UNIVERSITAT POLITÈCNICA DE VALÈNCIA

DEPARTAMENTO DE COMUNICACIONES

Fiber-Based Terahertz Time-Domain Spectroscopy Systems Operated in the Telecom Band

---

Thesis

to obtain the degree

Doctor of Philosophy (Ph.D.)

in Telecommunication

presented at the

Universitat Politècnica de València

by

Alexander Stefan Bockelt

Thesis director: Dr. Borja Vidal Rodríguez

Valencia, Spain, July 2017

The presented doctoral thesis has been revised and evaluated by the following external reviewers:

Dr. Jean-Louis Coutaz,

Université Savoie Mont Blanc, Chambéry, Auvergne-Rhône-Alpes, France

---

Dr. Mira Naftaly,

National Physical Laboratory, Teddington, Middlesex, United Kingdom

---

Dr. Guillermo Carpintero del Barrio,

Universidad Carlos III, Madrid, Spain

The thesis has been accepted by the Escola de Doctorat of the Universitat Politècnica de València on June 16th, 2017 and has been defended in Valencia on July 12th, 2017 against the following doctoral board:

Dr. Jean-Louis Coutaz (President),

Université Savoie Mont Blanc, Chambéry, Auvergne-Rhône-Alpes, France

---

Dr. Enrique Castro Camus (Secretary),

Centro de Investigaciones en Óptica A.C., León, Guanajuato, Mexico

---

Dr. Yahya Moubarak Meziani (Spokesman),

Universidad de Salamanca, Salamanca, Castilla y León, Spain

Table of Contents

Abstract

The aim of the doctoral thesis is the study of Terahertz time domain spectrometers relying on telecommunication fiber technology. Optical fiber offers low losses, high stability and compactness, features that ease the deployment of this kind of sensing instruments in industrial scenarios. The development of terahertz signal sources working at telecom wavelengths has enabled the employment of mature, telecom-related photonic components that allowed a transition within THz research from being mainly object of scientific interest to an application-oriented technology. In this thesis, fiber terahertz systems utilizing ultrafast photoconductors with integrated antenna structures have been investigated at different levels, including the control of the photoconductor structure, as well as at instrument and system levels.

The carrier transport in InGaAs–InAlAs multilayer hetero-structures, present in the employed photoconductive antennas, has been investigated under the additional injection of a continuous optical wave. By varying the amplitude level of the respective optical signal injected into either the emitter or the receiver, it has been shown that the amplitude of the detected photocurrent could be controlled without affecting its bandwidth. Unlike increasing the optical power of the pulsed signal, raising the continuous optical power results in a reduction of the measured photocurrent. This lowering of the conductivity is related to changes in the instantaneous carrier momentum relaxation time in the photoactive material, rather than to variations of the free carrier density level. This behavior affects systems including continuous-wave optical components, as, for

instance, optical amplifiers. The effect has been further exploited to modulate the operation conditions of photoconductive antennas, enabling an all-optical control of the THz amplitude. This represents a method to implement a signal modulation, necessary, for instance, for lock-in signal detection.

Different industrial applications and THz imaging systems require fast data acquisition. Slow, stepwise working mechanical optical delay lines are about to be replaced by faster schemes. A fast THz-time-domain spectroscopy system using a coil-based rapid mechanic delay line has been set up and analyzed.

A convenience of usage of optical fibers is the simplicity of signal multiplication and distribution. It can be exploited to allow centralized operation of a set of parallel terahertz sensing units. A centralized architecture with optical source sharing simplifies the implementation as well as the cost of nondestructive inspection platforms, where several sensing units would have to work in the same facility, for example at quality control in factories or security checkpoints. The cost of such a distribution system is evaluated, its feasibility experimentally demonstrated, and key features relevant to the system performance are discussed.

The present document is formally structured in a brief introduction, Chapter 2, which reviews common terahertz technology as a whole, with the focus on optoelectronic schemes and respective technology in the telecom band. Chapter 3 includes work carried out dealing with the carrier dynamics under continuous optical wave irradiation of the photoconductive antenna modules and the application of the effect as modulation method. Chapter 4 deals with the implementation of the fast delay in the system and Chapter 5 describes and analyses

architecture for parallel, remotely controlled sensing. Finally, Chapter 6 provides conclusion and future work perspectives.

Resumen

El objetivo de la presente Tesis Doctoral es el estudio de espectroscopios temporales de Terahercios basados en tecnología de fibra óptica para telecomunicaciones. La fibra óptica ofrece bajas pérdidas de propagación, alta estabilidad y la capacidad de implementar sistemas robustos y compactos, características que facilitan el despliegue de este tipo de instrumentos de sensado en escenarios industriales. El desarrollo de fuentes de THz que operan en la banda infrarroja empleada en telecomunicaciones permite el uso de componentes maduros de la industria de las comunicaciones ópticas, lo que a su vez se ha traducido en una transición desde el uso de la banda de THz básicamente para intereses científicos al desarrollo de sistemas para aplicaciones industriales. En la presente tesis se investigan sistemas de THz basados en antenas fotoconductivas y fibra óptica a distintos niveles: control de la estructura fotoconductiva, instrumento y sistema.

El transporte de portadores en heteroestructuras multicapa InGaAs–InAlAs, empleadas actualmente en antenas fotoconductivas, se ha investigado bajo la inyección de una onda óptica continua. Se ha observado que variando el nivel de amplitud de esta onda continua tanto en el emisor como en el receptor es posible controlar la fotocorriente detectada sin afectar a su ancho de banda. A diferencia de un incremento en la potencia óptica de la señal pulsada, elevar el nivel de continua resulta en una reducción de la fotocorriente medida. Esta reducción de la conductividad se relaciona con cambios en el tiempo de relajación del momento de los portadores en el material fotoactivo en lugar de variaciones de la densidad de portadores libres. Este

comportamiento puede tener un efecto en sistemas que introduzcan componentes ópticos continuos como por ejemplo sistemas de sensado que empleen amplificadores ópticos. Este efecto puede ser usado para modular las condiciones de operación de las antenas fotoconductivas permitiendo el control todo-óptico del sistema. Este método permite modular la señal, lo que resulta necesario por ejemplo para realizar detección lock-in.

Tanto diferentes aplicaciones industriales como los sistemas de imagen en THz requieren sistemas rápidos de captura. Para ello es necesario sustituir las líneas de retardo ópticas tradicionales basadas en motores paso-a-paso por otros sistemas de mayor velocidad. Se ha implementado y caracterizado un sistema THz-TDS usando una línea de retardo rápida basada en bobinas de voz.

Una característica fundamental de la fibra óptica es su extraordinaria simplicidad para realizar la distribución de señales ópticas. Esta característica puede ser explotada para permitir la operación centralizada de un conjunto paralelo de sensores de THz. Una arquitectura centralizada en la que la fuente óptica se comparte entre muchos sensores simplifica la implementación y reduce el coste de sistemas de inspección no destructiva que requieran de múltiples sensores en paralelo, como, por ejemplo, en control de calidad industrial o en controles de seguridad. Se ha evaluado el coste de estos sistemas distribuidos, se ha validado experimentalmente su viabilidad y se han identificado y estudiado sus prestaciones.

El documento de la tesis doctoral se estructura formalmente en una breve introducción, el capítulo 2, en el que se revisa la tecnología de THz en su conjunto, los esquemas optoelectrónicos y el uso de tecnologías ópticas basadas en la banda de las

telecomunicaciones. El capítulo 3 incluye el estudio realizado sobre la dinámica de los portadores bajo la irradiación dela antena fotoconductiva con una onda óptica continua y su uso como técnica de modulación. El capítulo 4 trata con la implementación de un sistema THz-TDS rápido mientras que el capítulo 5 describe y analiza una arquitectura de sensado paralela para reducir costes. Finalmente el capítulo 6 recoge las conclusiones y futuras líneas de actuación.

Resum

L'objectiu de la present Tesi Doctoral és l'estudi d'espectroscopis temporals de terahertzs basats en tecnologia de fibra òptica per a telecomunicacions. La fibra òptica ofereix baixes pèrdues de propagació, alta estabilitat i la capacitat d'implementar sistemes robustos i compactes, característiques que faciliten el desplegament d'aquest tipus d'instruments de sensat en escenaris industrials. El desenvolupament de fonts de THz que operen a la banda infraroja emprada en telecomunicacions permet l'ús de components madurs de la indústria de les comunicacions òptiques, el que al seu torn s'ha traduït en una transició des de l'ús de la banda de THz bàsicament per interessos científics al desenvolupament de sistemes per a aplicacions industrials. En la present tesi s'investiguen sistemes de THz basats en antenes fotoconductivas i fibra òptica a diferents nivells: control de l'estructura fotoconductiva, instrument i sistema.

El transport de portadors en heteroestructures multicapa InGaAs-InAlAs, emprades actualment en antenes fotoconductivas, s'ha investigat sota la injecció d'una ona òptica contínua. S'ha observat que variant el nivell d'amplitud d'aquesta ona contínua tant en l'emissor com en el receptor és possible controlar la fotocorriente detectada sense afectar el seu ample de banda. A diferència d'un increment en la potència òptica del senyal polsada, elevar el nivell de contínua resulta en una reducció de la fotocorrent mesurada. Aquesta reducció de la conductivitat es relaciona amb canvis en el temps de relaxació del moment dels portadors en el material fotoactiu en lloc de variacions de la densitat de portadors lliures. Aquest comportament pot tenir un

efecte en sistemes que introdueixin components òptics continus com ara sistemes de sensat que utilitzen amplificadors òptics. Aquest efecte pot ser usat per modular les condicions d'operació de les antenes fotoconductivas permetent el control tot-òptic del sistema. Aquest mètode permet modular el senyal, el que resulta necessari per exemple per realitzar detecció lock-in.

Tant diferents aplicacions industrials com els sistemes d'imatge en THz requereixen sistemes ràpids de captura. Per a això és necessari substituir les línies de retard òptiques tradicionals basades en motors pas-a-pas per altres sistemes de major velocitat. S'ha implementat i caracteritzat un sistema THz-TDS usant una línia de retard ràpida basada en bobines de veu.

Una característica fonamental de la fibra òptica és la seua extraordinària simplicitat per realitzar la distribució de senyals òptiques. Aquesta característica pot ser explotada per a permetre l'operació centralitzada d'un conjunt paral · lel de sensors de THz. Una arquitectura centralitzada en la qual la font òptica es comparteix entre molts sensors simplifica la implementació i redueix el cost de sistemes d'inspecció no destructiva que requereixin de múltiples sensors en paral · lel, com, per exemple, en control de qualitat industrial o en controls de seguretat . S'ha avaluat el cost d'aquests sistemes distribuïts, s'ha validat experimentalment la seua viabilitat i s'han identificat i estudiat les seues prestacions.

El document de la tesi doctoral s'estructura formalment en una breu introducció, capítol 2, en el qual es revisa la tecnologia de THz en el seu conjunt, els esquemes optoelectrònics i l'ús de tecnologies òptiques basades en la banda de les telecomunicacions. El capítol 4 inclou l'estudi realitzat sobre la dinàmica dels portadors sota la irradiació de la antena fotoconductiva amb una

ona òptica contínua i el seu ús com a tècnica de modulació. El capítol 5 tracta la implementació d'un sistema THz-TDS ràpid mentre que el capítol 6 descriu i analitza una arquitectura de sensat paral · lela per reduir costos. Finalment, el capítol 7 recull les conclusions i futures línies d'actuació.

1. Introduction

Light is a fascinating phenomenon that has amazed humankind since remote times. Eventually, the electromagnetic nature of light was theoretically predicted by James Clerk Maxwell and experimentally confirmed by Heinrich Hertz in the late 19th century. With the instrumentation to generate radio waves and the discovery of X- as well as Γ-rays, following shortly after, humankind successively explored a wider range of the electromagnetic spectrum. Along with the comprehension of phenomena related to respective spectral bands, engineers were continuously gaining technological domination of those, in other words, generation and detection techniques were developed. Technologies corresponding to certain spectral bands mostly underwent significant progress, when engineering was driven by gadgetry demands related to the historical context. For instance, microwave electronics developed rapidly during the first half of the 20th century, due to communication and sensing equipment requirements by military machinery during both World Wars and nuclear technology was majorly developed during the nuclear arms race in the Cold War era. In contrast, the field of photonics gained its importance much later in the second half of the

century, when its development was boosted by demands of informatics and communications. A classic example for the long time lacking utility of optical technology is the Laser, which at the time of its first realization by Theodore H. Maiman in 1960 [1] counted as a "solution looking for a problem," but afterwards evolved to constitute a key component in a plethora of modern everyday life devices. Although technologically accessible spectral regions, in the electrical as well as in the optical domain, were continuously expanded, the band covering the frequencies superior to microwaves and inferior to infrared light, namely the so-called far-infrared or terahertz (THz) frequencies from approximately $100\ GHz - 10\ THz$ (see Figure 1) [2], has been out

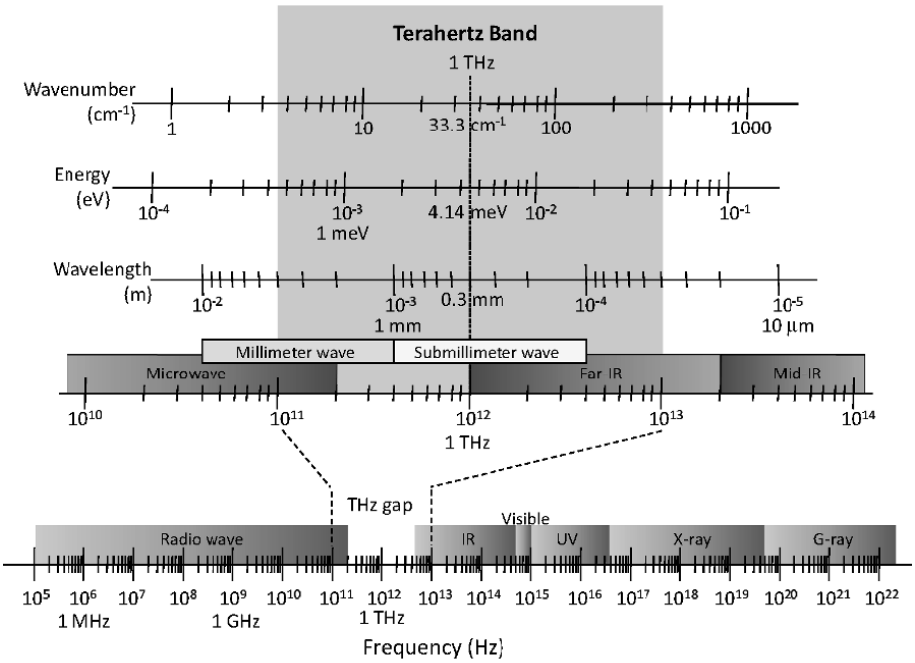

Figure 1. Location of the THz band in the electromagnetic spectrum. Graphic extracted from [2]

of reach until late. Straight photonic THz generation schemes, commonly exploiting optical transitions, were practically not suitable, because of the detrimental impact of thermal electronic excitation at room temperature. Microwave frequency up-conversion techniques, in contrast, turned out to be inefficient. In consequence, the THz spectral band was also labeled the "THz gap," since neither suitable emitters nor detectors have been available until recently.

Finally, success was granted to today's optoelectronic frequency down-conversion schemes, when the breakthrough in the field of ultrafast lasers as well as certain advances in semiconductor growth and processing technology occurred. Today, the most common or most widely spread broadband THz generation methods rely on ultra-short optical pulses, i.e. ultra-fast pulsed lasers, developed in the 1970s. With their groundbreaking works, David H. Auston [3] and Chi H. Lee [4] commonly count as the pioneers of ultrafast optical switching and the newly gaping research field named *THz optoelectronics*. Nevertheless, as in the case of the Laser, the potential of THz technology has firstly been unappreciated, so that "THz optoelectronics" rather embodied a scientific research field than a technological branch. Lacking an application-oriented driving force, THz equipment remained immature - until the possibilities in semiconductor device fabrication experienced a boost in the early 21st century. An ongoing optimization of material properties and the miniaturization of structure dimensions have made THz devices suitable for diverse applications, such as spectroscopy [5, 6, 7, 8, 9], environmental sensing, such as pollution detection [10], nondestructive material testing [11, 12, 13], imaging [14, 15], biomedical diagnostics [16, 17, 18], homeland security inspection

[19, 20] or high-speed terahertz wireless communication networks [21, 22, 23, 24], to name the most familiar ones. Moreover, newly available detectors are subject to further scientific interest, as for instance in molecular chemistry [25, 26, 14] or radio astronomy [27, 28], since a considerable part of rotational and vibrational molecular transitions, as well as about 98 % of cosmic radiation [29, 30], fall in the THz range. Lately, novel THz emitters and sensors in combination with robust and mature fiber-optic technology, including cheap and compact fiber lasers are replacing cumbersome and expensive free space arrangements with huge and costly laser sources.

In the following, Chapter 2 reviews the basics of THz technology and elucidates fundamental principles and components, focusing on the ultrafast photoconductive switching approach, which has been applied throughout the work of this thesis. Chapter 2 also provides an overview of the implementation of fiber technology and the use of telecom wavelengths in *terahertz time-domain spectroscopy* (THz-TDS) systems. Hereby, insight in the working principle on a microscopic level of the employed photo-switches is provided.

In Chapter 3 investigations are presented, which involve a continuous wave optical signal that has been used to manipulate the performance of *photoconductive antennas* (PCAs). In this context, this wave's microscopic scale physical impact is discussed, as well as a possibility for practical use as modulation application is elucidated.

Chapter 4 reports on an experimental arrangement introducing a high-speed mechanical optical delay line for rapid data acquisition. It provides insight into the optimization of performance parameters important in THz-TDS. Improvements

of the noise performance and the data capture time achieved by this scheme as well as the data processing methods are presented.

Chapter 5 presents studies about an architecture of parallel and remote control of several parallel THz-TDS systems. In particular, signal division, distribution and amplification in optical fibers is exploited to suggest an architecture for a network of parallel working THz sensor heads in an industrial scenario.

2. Terahertz Technology

The Terahertz band, which is the only spectral region named after its frequency rather than its wavelength, is typically considered to cover the frequency region of electromagnetic waves from $100\,GHz/300\,GHz$ to $10\,THz/30\,THz$. There is not a standard definition of its exact range and it overlaps with the microwave regime at low frequencies as well as with the *mid-infrared* (MIR) regime at its high frequency end. This region has also been known as the *far-infrared* (FIR) and alternate designations exist for some portions of this band such as *millimeter waves* (MMW, $\lambda = 1 - 10\,mm$) and *submillimeter waves* (SMMW, $\lambda = 0.1 - 1\,mm$). Whereas solid-state devices related to microwave technology are traditionally employed to generate and sense MMW, optical or thermal techniques are more common in the THz regime. Generation methods based on microwave technology to reach THz frequencies are known as frequency up-conversion methods [31], whereas photonic-assisted techniques are referred to as frequency down-conversion schemes [32]. Quasi-optical transitions also have been exploited for direct generation of THz signals in gas lasers (transitions between rotational modes in molecular gases [33]) or *THz quantum cascade lasers* (THz-QCL) [34, 35, 36] (inter-sub-band transitions),

whereby the general requirement of cryogenic cooling fundamentally limits their applicability. Operation at room temperature has been achieved at MIR frequencies [37] and lately intra-cavity *difference frequency generation* (DFG) has expanded the range into the FIR [38]. Moreover, free electron acceleration-based generation methods have also been developed. With those, particularly bright THz radiation can be achieved, since free electron beams do not impose limitations by material damage. Concretely, this is achieved in *backward wave oscillators* (BWOs) [39] and *free-electron lasers* (FELs) [40]. While BWOs are tabletop equipment, FELs are huge facilities and rather serve for high-end scientific experiments than portraying applicable technologic solutions.

Generally, THz sources are classified in *pulsed* or *broadband* and *continuous wave* (CW) or *narrowband* sources. Whereas microwave up-conversion methods usually generate CW radiation, photonic schemes exist for both, pulsed and continuous signals: *photo mixing,* DFG and *optical parametric amplification* (OPA) for the former and *transient photoconductive switching* and *optical rectification* (OR) for the latter. Generation through free electron acceleration exists for both, narrowband as well as broadband signals.

On the other side, THz detection schemes are classified in coherent and incoherent methods. Coherent schemes like photoconductive switching and *electro-optic sampling* (EOS) serve for pulsed signal detection and photomixing serves for continuous waves. III-V solid-state heterodyne detectors, in contrast, only apply for continuous signals. Incoherent detectors such as *bolometers* [41], *pyroelectric detectors* [42] and *Golay cells*

[43], rely on the thermal effect caused by THz wave absorption and hence measure THz wave intensities at relatively slow speeds.

In this chapter, THz generation and detection schemes are reviewed. The focus thereby is laid on opto-electronic approaches. An introduction into THz time-domain spectroscopy (THz-TDS), the major THz tool, is given, while the last section particularly deals with the realization of such a system based on optical fiber.

2.1 Terahertz Electronics

The electronic approach towards generation of THz radiation is based on III-V-solid-state devices, typically based on InP *high-electron mobility transistor* (HEMT) MMICs. Signals of microwave synthesizers are used for frequency multiplication, reaching up to hundreds of GHz [2]. New frequency components based on the input frequencies are generated when these microwave signals are coupled to electronic circuits (mixers) with highly nonlinear characteristics, like, for example, circuits including Schottky barrier diodes.

Nonlinear mixers generate multiple new frequency components based on the input frequencies. For instance, if the microwave signals $E_1(t) = E_1 \cos(\omega_1 t)$ and $E_2(t) = E_2 \cos(\omega_2 t)$ are mixed by a nonlinear mixer with a quadratic nonlinearity $\chi^{(2)}$, frequency components at both of the input frequencies ω_1 and ω_2 (linear part), a continuous part, second harmonics of both input frequencies $2\omega_1$ and $2\omega_2$ and a sum $(\omega_1+\omega_2)$ as well as a difference frequency component $(\omega_1-\omega_2)$ appear at the device's output:

$$
\begin{aligned}
V_{out}(t) &= \chi^{(2)}[E_1(t) + E_2(t)]^2 \\
&= \chi^{(2)}[E_1 \cos(\omega_1 t) + E_2 \cos(\omega_2 t)]^2 \\
&= \frac{1}{2}\chi^{(2)}(E_1^2 + E_2^2) \\
&+ \frac{1}{2}\chi^{(2)}E_1^2 \cos(2\omega_1 t) \\
&+ \frac{1}{2}\chi^{(2)}E_2^2 \cos(2\omega_2 t) \\
&+ \frac{1}{2}\chi^{(2)}E_1E_2 \cos[(\omega_1+\omega_2)t] \\
&+ \frac{1}{2}\chi^{(2)}E_1E_2 \cos[(\omega_1-\omega_2)t]
\end{aligned} \tag{1}
$$

Appropriate filtering isolates the desired signal. In this particular case, both emerging harmonics and the sum frequency might be in the range of interest (THz range). Mixers with higher order nonlinearity generally cause higher order harmonics and mixed terms. Since the output power shrinks as $1/f^3$ with frequency, the conversion becomes drastically inefficient for high harmonics exceeding some hundred GHz. Hence, the practicability of electronic concepts is confined to the lower THz frequency range (max. $1.5\,THz$) and moderate powers ($< 100\,\mu W$). Additionally, electronic solutions are limited to narrowband signals with a relative bandwidth in the range of $\Delta f/f \sim 10^{-6}$; hence, for wideband THz signals either optoelectronic or free electron schemes are required.

2.2 Terahertz Optoelectronics

Probably the widest-spread technologies to access the THz band are those based on frequency down-conversion schemes by means of optoelectronic devices due to their ability to reach large portions of this spectral region. Additionally, they provide efficient, compact and versatile solutions.

This chapter reviews the most relevant optoelectronic generation and detection schemes. Whereas for brevity a quite basic overview of concepts is provided here, complete round-ups can be found in literature [2, 6, 14]

2.2.1 Continuous Wave Terahertz Radiation

Pulsed systems provide a broader range of spectral information, generally favorable in spectroscopy or imaging, whereas CW systems benefit from high resolution, compactness and simplicity [44]. In the following section, an overview of CW techniques is provided. Usually the interplay of CW signals in a nonlinear medium or device is exploited to generate or sense radiation at THz frequencies.

2.2.1.1 Continuous Wave Signal Generation

CW THz generation methods can be classified in two major categories, one exploiting photoconduction in semiconductor materials to convert electrical energy provided by an external bias voltage and another based on nonlinear optical crystals translating optical energy to the THz range.

2.2.1.1.1 Photo Mixing

Analogously to microwave up-conversion circuits, there exist opto-electronic heterodyne down-conversion schemes to generate CW THz signals from CW optical waves, which are referred to as *photo mixing* [45, 46]. Two continuous optical signals incident on a PCA alter its conductivity at their beat frequency. The photocurrent induced in the biased PCA then oscillates with the beat frequency and radiates electromagnetic energy either via a connected metallic antenna structure or simply via surface currents in the photo-conducting material itself, for example in *large area emitters* (LAE) [47, 48, 49]. Preferentially, both signals originate from a single source to grant phase stability and to evade sensitive and complex alignment procedures. This prompts the deployment of dual-mode lasers [50, 51].

If the photo-mixer is illuminated by the beams of two different laser modes with amplitudes E_1, E_2 and frequencies ω_1, ω_2, the incident electric field $E_{opt}(t)$ is made up of the fields of both:

$$E_{opt}(t) = E_1 e^{-i\omega_1 t} + E_2 e^{-i\omega_2 t} \tag{2}$$

The optical power, hence, is proportional to the square of the instantaneous electric field

$$P_{opt}(t) \propto |E_{opt}(t)|^2 \propto P_0 + P_{beat} \cos(\omega_- t), \tag{3}$$

where $P_0 = P_1 + P_2$ is the temporal average power, $P_{beat} = 2\sqrt{P_1 P_2}$ is the beat power and $\omega_- = \omega_1 - \omega_2$ is the beat or difference frequency. It alters the conductivity and thus the

flowing photocurrent $I_{phot}(t)$ under a constant bias voltage, what can be described by

$$I_{phot}(t) = \int P_{opt}(t - t') \left(e \cdot n(t') \cdot v(t')\right) dt' \tag{4}$$

The radiated electromagnetic field, being the first temporal derivative of the oscillating current in a radiating Hertzian dipole model, can finally be approximated as

$$E_{THz}(t) \propto - P_{beat} \sin(\omega_- t - \phi). \tag{5}$$

Obviously, the radiated field oscillates with the beat frequency ω_-. Choosing ω_1 and ω_2 with the appropriate spacing, the radiated field is a THz electromagnetic wave. Expanding this principle to successively involving higher numbers of longitudinal laser modes, as in mode-locked lasers or optical combs, one obtains pulsed operation, since the former two-tone beat signal reshapes toward an impulsive waveform. This concept, presented in paragraph 2.2.2.1.1 is known as *photo switching*.

2.2.1.1.2 Difference Frequency Generation

Difference Frequency Generation is a second-order nonlinear process and hence requires a medium with a non-centrosymmetric lattice structure. Two longitudinal laser modes $E_1 = E_0 \cdot \sin(\omega_1 t)$ and $E_2 = E_0 \cdot \sin(\omega_2 t)$ are incident on the device and collinearly propagate through the medium as

$$\begin{aligned} E_{opt}(t) = E_1(t) + E_2(t) &= E_0[\sin(\omega_1 t) + \sin(\omega_2 t)] \\ &= 2E_0 \cos\left(\frac{\omega_-}{2} t\right) \sin\left(\frac{\omega_+}{2} t\right), \end{aligned} \tag{6}$$

where $\omega_- = \omega_1 - \omega_2$ stands for the difference and $\omega_+ = \omega_1 + \omega_2$ for the sum frequency. To assure a temporal and spatial beat signal, parallel polarization is necessary. The anisotropic atomic structure causes a remnant polarization $P(t)$ inside the material, which in turns starts to propagate at the beat frequency ω_-:

$$P(t) = \chi^{(2)} E_0^2 \left[\cos\left(\frac{\omega_-}{2} t\right)\right] = \frac{1}{2}\chi^{(2)} E_0^2 [1 + \cos(\omega_- t)], \tag{7}$$

where $\chi^{(2)}$ is the second-order nonlinear susceptibility. The polarization-induced electric radiation field is hence

$$E_{THz}(t) \propto \frac{\partial^2 P(t)}{\partial t^2} = -\frac{1}{2}\chi^{(2)} \omega_-^2 E_0^2 \cos(\omega_- t). \tag{8}$$

ω_- is chosen to fall in the THz range. If the optical refractive index for both involved optical waves is approximately the same ($n_1 \approx n_2 \approx n_{opt}$), the momentum mismatch of the THz and the optical waves is

$$\Delta k = n_{opt} \frac{\omega_1}{c} - n_{opt} \frac{\omega_2}{c} - n_{THz} \frac{\omega_-}{c} = \Delta n \frac{\omega_-}{c}. \tag{9}$$

When the phase-matching condition $\Delta k \cong 0$ is satisfied, both co-propagate and energy is continuously transferred from the latter to the former. Hence, the THz wave undergoes coherent amplification, as long as the *walk-off* between both waves is small. In practice, the conversion is limited by this walk-off. Depending on the material, the phase-matching condition might not be satisfied for simple geometries. Therefore, different approaches have been made to fulfil this requirement (see Section 2.2.2.1.2).

2.2.1.1.3 Optical Parametric Amplification

Like DFG, *optical parametric amplification* (OPA) [52] exploits a nonlinear process inside a crystal, but here only a single frequency input signal is required. An incident pump photon of frequency ω_p is split into a so-called idler photon of a lower frequency ω_i and a second one of frequency ω_{THz} carrying the difference momentum. The appropriate choice of wavelength and crystal lets the difference wave fall in the THz regime. If the phase-matching condition

$$\vec{k}_p = \vec{k}_i + \vec{k}_{THz} \tag{10}$$

is satisfied, both resulting waves are amplified. Phase-matching often involves non-collinear propagation of the different waves. This fact has been used to generate tunable narrowband THz waves. A typical crystal for OPA is $LiNbO_3$, where for instance an NIR pump beam of wavelength $\lambda_p = 1064\,nm$ has been used to generate THz signals between $1 - 3\,THz$ by varying the angle between $\overrightarrow{k_p}$ and $\overrightarrow{k_i}$.

2.2.1.2 Continuous Wave Signal Detection

Sensing of CW THz radiation is often realized by down-converting heterodyne receivers. As alternatives to coherent optoelectronic detection schemes, sensing can also be performed utilizing incoherent detectors. In radio astronomy, for instance, thermal detectors were widely employed to sense THz bands. A brief description of CW THz sensors is given in the following paragraphs.

2.2.1.2.1 Heterodyne Detection

CW THz signals can be detected with a heterodyne scheme, which is the inverse process of the photomixing. A nonlinear element mixes the input signal $E_{sig}(t) = E_{sig}\cos(\omega_{sig}t)$ with a local oscillator's optical reference tone $E_{ref}(t) = E_{ref}\cos(\omega_{ref}t)$ of a known frequency ω_{ref}. According to Equation (1) (see Section 2.1), several frequency components appear at the output. The difference frequency signal $\frac{1}{2}\chi E_{sig}E_{ref}\cos[(\omega_{sig}-\omega_{ref})t]$ is separated by an isolator and amplified. If the frequency of the local oscillator ω_{ref} is in the appropriate range, $\omega_{sig}-\omega_{ref}$ falls in a spectral range, which is already accessible by electronic spectrum analyzers. Via this measurable *radio frequency* (RF) signal, the input signal at THz frequency ω_{sig} can be identified computationally.

2.2.1.2.2 Thermal Detection

Thermal detectors are incoherent detectors, which measure the incident THz power via the temperature change in an absorber. The translation mechanism of these small temperature variations depends on the type of detector.

Bolometers, for example, make use of a temperature-dependent resistivity change of the absorber. Their broad spectral range with maximum sensitivity in the THz band is their asset, their demand for cryogenic cooling a practical disadvantage.

Pyroelectric detectors make use of the temperature-induced spontaneous electric polarization change of a pyroelectric crystal, when it is illuminated. In its dark state, the bulk electric

polarization of a pyroelectric crystal is compensated by surface charges, so that no macroscopic polarization remains, unlike e.g. the permanent magnetization of bar magnets. The pyroelectric detector utilizes such a crystal filling up the spacing of a capacitor. A radiation absorber is placed at one electrode of the capacitor, forwarding its heat into the crystal. Absorbing radiation, i.e. increasing temperature lowers the spontaneous polarization in the pyroelectric material and thus the compensating surface charges. A circuit is measuring the current flow between the electrodes, when it is closed. Since the current is associated to a change of temperature, it cannot work in in steady-state mode, but needs an AC modulation of the signal to measure the change periodically.

Golay cells are acousto-optic radiation detectors. Incident radiation is absorbed by the surface coating of a membrane enclosing a gas chamber. The coating heats the gas and its induced volume change bends the surface. An optical beam incident on a reflector on the membrane is deflected and the deflection measured by a read-out system of photo detectors. For the same reason as pyroelectric detectors, Golay cells also need a modulated THz signal, which is usually done at acoustic frequencies. They represent the thermal detectors with highest sensitivity at room temperature.

2.2.2 Broadband Terahertz Radiation

Broadband or pulsed THz generation became possible with the emergence of ultrafast lasers. The extended bandwidth of the optical signal defines a theoretical upper frequency limit in the

down-conversion process. However, a limiting factor, at the generation as well as the detection, is THz absorption by optical phonon resonances, which takes place in the THz generating or sensing crystal. This impedes the full exploitation of the optical bandwidth, which principally can extend up to decades of THz. This section reviews the common pulsed operation optoelectronic generation and detection methods.

2.2.2.1 Broadband Signal Generation

In contrast to CW or narrowband signals, the representation of broadband signals in the time domain results in a few-, single-, or even half-cycle pulses, which take their ideal, ultimately transform-limited waveforms, when the frequency components are perfectly phase-matched. The optical seed signals in THz optoelectronics thus have to vary on a time scale $\leq ps$, corresponding to the THz range. Mode-locking techniques in lasers or laser amplifiers generate signals, which exhibit durations and rise times in the sub-picosecond range, typically from a few tens to a hundred femtoseconds. The down-conversion of these optical signals to THz frequencies is mostly done exploiting two different mechanisms: Either, analog to photomixing, the conductivity of micro-structured photoconductive semiconductor devices is switched by the optical signal or the polarization response to optical waves of nonlinear media creates a secondary wave propagating at THz frequencies. As for CW schemes, the major difference between both methods is that PCAs convert electric field energy, whereas nonlinear crystals convert optical energy. Consequently, the formers' output power is scalable over

a wide range until a breakdown voltage is reached, whereas the latter are limited by available optical power, phase-matching conditions and multiphoton absorption [53].

2.2.2.1.1 Photoconductive Switching

Photoconductive switches or photoconductive antennas are miniature size opto-electronic switches integrated on semiconductor chips, which make use of the change of electrical conductivity under optical irradiation [2, 3, 54]. Photoconductors are designed to be insulating in the dark state, but become highly conductive, when photons with energies equal or superior to its electronic energy bandgap are absorbed. In the solid-body electronic band-structure view, photon absorption raises electrons to the *conduction band* (CB) or creates holes in the *valence band* (VB). These mobile charge carriers, submitted to an externally applied bias voltage, accelerate and build up a current transient. According to the oscillating dipole model, this surge current eventually radiates electromagnetic energy with THz frequencies. The switch-on time thereby is governed by the rising slope of the excitation pulse, while the switch-off time depends on the recovery time, i.e. the carrier lifetime, of the photoconductive material. Since the pulse rise time of ultrafast lasers is shorter than material recovery times, they determine the highest frequency components, i.e. the THz signal's bandwidth. The current's fall time depends on recombination processes, which conceptually restrict the carriers' lifetime to a time scale suitable for THz responses. Carrier lifetimes determine the spectral position of the amplitude maximum. In common photoconductor

materials, used for THz generation, the electron mobility is about one order greater than the one of the holes, hence, the electron dwell time in the CB is the determinant parameter. *Electron-hole recombination* (e-h-recombination), the capture of a CB-electron by a VB-hole, is generally a slow process ($\sim ns$ in InGaAs [55]), too slow to feature THz responses. However, defect incorporation by, for example, doping, radiation damage, ion-bombardment, and growth temperature control at the semiconductor growth process, introduces intra-bandgap energy states, which represent localized electron trapping centers. The corresponding trapping process, *Shockley-Read-Hall* (SRH)*-recombination*, exhibits much shorter trapping times than e-h-recombination, ranging from several decades of picoseconds to the sub-picosecond range in InGaAs [56, 57]. Conventional materials for the fabrication of ultra-fast photoconductive devices have been low-temperature-grown (LTG)-GaAs or radiation damaged silicon-on-sapphire (RD-SOS), whereas lately more complex composites have emerged, which further have reduced electron lifetimes down to $\sim 200\, fs$ [56]. Besides fast responses, suitable photoconductor materials exhibit high electron mobility, favoring considerable photocurrents. On the other hand, materials with a low residual carrier concentration in its dark state are desired to suppress parasitic dark currents as effectively as possible. Eventually, the development of suitable materials is a tradeoff between optimizing carrier lifetime, mobility and conductivity.

The radiated power depends strongly on the efficiency of the antenna structure, which has been realized in a plethora of different geometries. In conventional approaches, metallic electrodes are connected to the functional material. Electrode shapes are classically strip-line-, dipole- or bow-tie-like, however,

many approaches have been made to enhance the emission by variating the antenna structure. Miniaturized electrodes with nano-size gaps ($\sim 100\,nm$) have been considered to reduce the carrier transit time and enable ballistic carrier transport [58]. On the other side, no radiating structure is required in LAE-structures, since the currents in the functional material itself act as radiating structure. Latest research has implemented arrays of plasmonic nano-antennas on an ErAs:InGaAs photoconductive material and thus achieved the highest reported THz output power of $\sim 300\,\mu W$ with PCAs operating at telecom wavelengths [59].

In a simple picture, the PCA can be considered a short oscillating Hertzian dipole. Excited by an impulsive current, this dipole in turn radiates an electromagnetic pulse. Due to the mismatch of wave impedance because of the discrepancy in refractive indices, the major part of the radiated power is released into the substrate. Since a portion of the wavelengths and the device dimensions are of the same order, the radiation pattern is highly divergent. Usually a hyper-hemispherical silicon lens, which is glued to the backside of the substrate, is employed to diminish the divergence. However, to produce a collimated beam with quasi-plane wave fronts, as it is desired for many applications, additional THz optics (see Section 2.3.4) are necessary.

In the following, analytical expressions describing the generation process in a photoconductive switch [60] are outlined. Initially, as in a finite impulse response system, the photocurrent density $j(t)$ is expressed as the convolution between the temporal shape of the optical power P_{opt} received and the impulse response of the photo-switch:

$$j(t) = P_{opt}(t) \otimes [en(t)\overline{v}(t)] \tag{11}$$

Here, e denotes the elementary charge, $n(t)$ the time-dependent carrier density and $\overline{v}(t)$ the carrier drift velocity. The exciting optical pulse is assumed to have a Gaussian form with a pulse width τ_{exc} and carrier relaxation is assumed to follow a simple exponential decay law with time constant τ. Photo-excited carriers in semiconductors are well-described by the classical Drude-model, so that using a mean carrier collision or momentum relaxation time $\delta\tau$ and the effective mass m_{eff} the equation of motion for those carriers is

$$\frac{d\overline{v}(t)}{dt} = -\frac{\overline{v}(t)}{\delta\tau} + \frac{q}{m_{eff}}E(t). \tag{12}$$

$E(t)$ is the strength of the bias field applied to the electrodes and is supposed to be approximately constant and uniform over the illuminated area. For moderate optical intensities, which do neither evoke saturation effects in the excited carrier concentration nor field screening by space charge effects, combining Equations (11) and (12) yields the following expression for the current in the time-domain:

$$\begin{aligned} j(t) \propto \Bigg\{ & exp\left(\frac{\tilde{\tau}_{exc}^2}{4\tau^2} - \frac{t}{\tau}\right) \cdot \ erfc\left(\frac{\tilde{\tau}_{exc}}{2\tau} - \frac{t}{\tilde{\tau}_{exc}}\right) \\ & - exp\left(\frac{\tilde{\tau}_{exc}^2}{4\tilde{\tau}^2} - \frac{t}{\tilde{\tau}}\right) \cdot erfc\left(\frac{\tilde{\tau}_{exc}}{2\tilde{\tau}} - \frac{t}{\tilde{\tau}_{exc}}\right)\Bigg\} \\ & \cdot \frac{P_{opt}E_{bias}\delta\tau}{m_{eff}} \end{aligned} \tag{13}$$

Here, $\tilde{\tau}_{exc} = \tau_{exc}/(2\sqrt{ln2})$, the optical pulse duration, and $1/\tilde{\tau} = 1/\tau + 1/\delta\tau$, where τ is the carrier relaxation time. E_{bias} is a constant bias field. The far field of an oscillating dipole is proportional to the first temporal derivative of its current density:

$$E_{THz}(t) \propto \frac{dj(t)}{dt}. \tag{14}$$

Hence, the temporal shape of the THz pulse is obtained taking the derivative of Equation (13). A plot of the temporal progresses of optical intensity, emitter photocurrent and radiated field strength is depicted in Figure 2. The THz field almost instantaneously follows the optical pulse at its rising flank. Although the current signal has a much longer tail due to the longer carrier lifetime, its impact on the field amplitude is small,

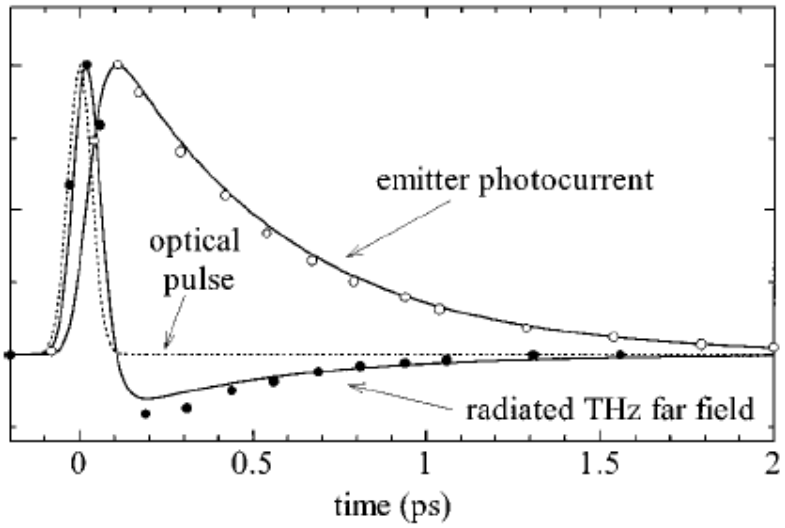

Figure 2. Temporal shapes of optical pulse, emitter photocurrent and radiated THz field for typical PCA emitter time parameters. Graphic extracted from [60]

because of the relatively slow decay. In practice, measured THz pulsed are followed up by oscillations in the GHz range, caused by reflections in the metallic antenna structure, which obscure the smooth relaxation.

The spectral power distribution can be obtained taking the Fourier transform of Equation (14),

$$E_{THz}(f) \propto \frac{(\tau - \tilde{\tau}) f \, exp(-(\pi f \tau_{exc})^2)}{(1 - 2\pi i f \tau)(1 - 2\pi i f \tilde{\tau})} \cdot \frac{P_{opt} E_{bias} \delta\tau}{m_{eff}}. \qquad (15)$$

2.2.2.1.2 Optical Rectification

The optoelectronic alternative to the photoconductive switching method to generate broadband THz radiation is to utilize a nonlinear crystal exploiting optical rectification, a second-order nonlinear effect similar to DFG and OPA. The optical behavior of matter is dominated by the electronic response to irradiated optical fields, so nonlinear optical phenomena occur due to nonlinear electronic motion.

In the Lorentz model for electronic motion, bound atomic electrons are considered to move harmonically with small elongations around their equilibrium positions of the chemical bonds in a crystal lattice. For those small elongations the potential energy, which electrons face, is approximately quadratic, what results in a linear response to the driving electric field (magnetic response is negligible for most materials). Thus, radiation emitted by those electronic dipole oscillators is in turn of the same frequency.

However, highly intense fields, as they occur in femtosecond pulses, prohibit the approximation of small elongations and hence quadratic potential energy functions. In media with di- or polyatomic matrices, which intrinsically show an inversion asymmetry due to highly polar chemical bonds, the resulting field forces drive the electronic motion into an inharmonic regime, where the potential has to be described by terms of higher orders. If a perturbation procedure with the electron's position

$$x(t) = \sum_{n=1}^{\infty} x^{(n)}(t), \quad n = 1,2,3, \ldots \tag{16}$$

up to the second order is made, the potential energy exhibits a cubic term and the equation of motion a quadratic term:

$$\frac{d^2x}{dt^2} + \gamma \frac{dx}{dt} + \omega_0^2 x + \alpha x^2 = -\frac{e}{m} E(t) \tag{17}$$

The first order equation is linear

$$\frac{d^2x^{(1)}}{dt^2} + \gamma \frac{dx^{(1)}}{dt} + \omega_0^2 x^{(1)} = -\frac{e}{m} E(t), \tag{18}$$

and returns

$$x^{(1)}(t) = -\frac{e}{m} \frac{E_0 e^{-i\omega t}}{\omega_0^2 - \omega^2 - i\omega\gamma} + c.c. \tag{19}$$

as solution and hence the optical response is at the incident wave's frequency ω. The second order equation of motion is

$$\frac{d^2x^{(2)}}{dt^2} + \gamma \frac{dx^{(2)}}{dt} + \omega_0^2 x^{(2)} = -\alpha (x^{(1)})^2 \tag{20}$$

and returns as solution

$$
\begin{aligned}
x^{(2)}(t) &= x_{2\omega}^{(2)} + x_0^{(2)} \\
&= -\alpha\left(\frac{eE_0}{m}\right)^2 \frac{e^{-i2\omega t}}{(\omega_0^2 - \omega^2 - i\omega\gamma)^2[\omega_0^2 - (2\omega)^2 - i2\omega\gamma]} \\
&+ c.c. - 2\alpha\left(\frac{e}{m\omega_0}\right)^2 \frac{|E_0|^2}{(\omega_0^2 - \omega^2)^2 + \omega^2\gamma^2}.
\end{aligned} \tag{21}
$$

It consists of two terms, of which $x_{2\omega}^{(2)}$ is oscillating at the double frequency (*second harmonic generation*, SHG) and $x_0^{(2)}$ is a frequency-independent constant that is proportional to the square of the electric field amplitude $|E_0|^2$ (OR). This means that the static nonlinear polarization $P_0^{(2)}$ associated to OR is proportional to the intensity $I_0 \propto |E_0|^2$of the optical signal:

$$
\begin{aligned}
P_0^{(2)} &= -Nex^{(2)}(t) \\
&= -\left(\frac{e}{m\omega_0}\right)^2 \frac{2\alpha e^2 N|E_0|^2}{m^2\omega^2[(\omega_0^2 - \omega^2)^2 + \omega^2\gamma^2]} \\
&= 2\epsilon_0\chi_{ijk}^{(2)}(0, \omega, -\omega)|E_0|^2
\end{aligned} \tag{22}
$$

with $\chi_{ijk}^{(2)}$ being the second-order nonlinear susceptibility tensor. If instead of a plane wave a Gaussian optical pulse with duration much longer than the optical cycle is incident, the temporal trace of $P_0^{(2)}(t)$ replicates its pulse envelope and is in turn source of electromagnetic radiation. Since the bandwidth of such signals is approximately determined by the inverse pulse duration, pulses from femtosecond lasers $(10 - 100fs)$ produce radiation with THz content.

In anisotropic crystals $\chi_{ijk}^{(2)}$ is a real tensor with off-diagonal elements, so that OR has a different efficiency for each crystallographic direction. In the ideal case, the electric field vector of the linearly polarized optical signal coincides with the

crystal axis with the highest $\chi_{ijk}^{(2)}$. Commonly, this axis is the one along the polar chemical bonds.

As it is already indicated in Section 2.2.1.1.2, a second criterion for efficient generation is the phase or propagation velocity matching between the optical and the induced THz pulse. Since the refractive index in the optical domain, n_{opt}, and the refractive index in the THz band, n_{THz}, generally differ, the optical pulse and the induced distortion propagate at different speeds. Traversing the crystal, after a certain length, called *walk-off length*, the overlap between the optical pulse and the original induced nonlinear distortion is lost, so that there is no efficient energy transfer from the optical to the THz wave. The longest walk-off lengths, and hence energy transfer, are obtained, when the group velocity of the optical pulse and the phase velocity of the center wavelength of the THz pulse match. Ideally, n_O and n_T are similar at the operation wavelength. Fortunately, in *zinc telluride* (ZnTe), both refractive indices coincide at a wavelength of $822\,nm$ [61], which falls into the gain spectrum of a titanium-sapphire laser, making it a favorable candidate for nonlinear THz generation. Other approaches to achieve velocity matching include the use of tilted wave fronts [53, 62] and periodical poling of crystal layers [63].

Besides ZnTe, materials with high second-order nonlinearity are, for instance, ZnTe, GaAs, GaP, InP, GaSe, $LiTaO_3$, CdTe and $LiNbO_3$ [64, 2]. The latter, however, suffers from strong THz absorption and thus is not suitable for simple transmission geometries. Lately, there has been a development of nonlinear organic salt crystals, such as OH1 [65, 66, 67, 68], DAST [69, 70, 71, 72] and DSTMS [73, 74, 75, 76], which show a considerably higher nonlinear susceptibility and hence provide more efficient

THz generation. However, since the susceptibility is a function of frequency, the distinct gain curves produce various power spectra.

2.2.2.2 Broadband Signal Detection

For detection, often the inverse process of the generation is utilized. However, there are also detection schemes making use of the nonlinear susceptibility of a crystal. Both ideas are sketched in the following.

2.2.2.2.1 Photoconductive Switching

Analogously to the generation process, a photocurrent is generated in a PCA detector module, with the major difference that the bias field of the emitter is replaced by the incident THz field. The latter is much smaller than the bias field in the emitter, so that the antenna structure is adapted to the smaller photocurrents, for example by a narrow electrode gap and hence lower resistivity. The detector PCAs used in all experiments of this work have been dipole-shaped instead of the strip line-type of the emitters. As at the generation process, the detection bandwidth depends on the rise time of the optically induced carrier lifetime and therewith on the slope of the rising slope of the femtosecond pulse. The lifetime, instead, does not affect the detection bandwidth.

2.2.2.2.2 Electro-optic Sampling

A widespread technique to detect THz signals is based on the *Pockels effect.* Under an externally applied static electric field, an electro-optic crystal with second-order nonlinear susceptibility tensor $\chi_{ijk}^{(2)}$ becomes birefringent. This effect is closely related to OR, since in a lossless medium $\chi_{ijk}^{(2)}$ has the same coefficients [2]. The birefringence is proportional to the field strength and can be probed by irradiating light of linear polarization.

At certain delay and if the THz phase velocity and optical pulse group velocity match is granted, the optical pulses face a constant birefringence during propagation through the electro-optic crystal. Scanning the delay of the optical pulse and detecting the polarization change by birefringence hence maps the electric field strength of the THz pulse.

Experimentally, such a detector is realized by the arrangement in Figure 3. The optical probe beam suffers a dephasing of both orthogonal polarization components and becomes the more elliptic the stronger the electric field. The orientation of the linear polarization is chosen such that the linearly polarized probe beam is converted into a perfect

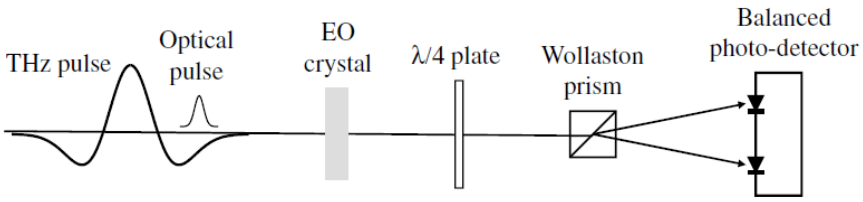

Figure 3. Schematic diagram of the setup of an EOS detector. Graphic extracted from [2].

circularly polarized beam after passing through a quarter-wave plate. A Wollaston prism splits both polarizations spatially into different beams, which are focused onto conversely wired photo-detectors. For zero field strength, both polarization components are equal and balance the photo-detectors, so that no current is measured.

However, in the presence of a non-zero field, the output polarization has generally become elliptic. After the quarter-wave plate, the polarization is then non-circular and the split beams are of different intensity. This unbalances the photodetectors and a current proportional to the THz field is measured.

2.3 Terahertz Time-Domain Spectroscopy

Terahertz time-domain spectroscopy is a time-resolved characterization method [6]. Since ultra-fast events such as current transients for THz generation occur on a time scale too small to be tracked in real time due to bandwidth limitations of electronic measurement equipment, a mapping technique is applied. An excitation pulse, the *pump pulse*, stimulates the experiment, whereas a second pulse, the *probe pulse,* probes the system's response at a certain temporal delay. This type of time-resolved measurement is commonly referred to as a *pump-probe-experiment*. It is convenient to use signals split from a single signal source to guarantee coherence and stability. Some experiments involve dividing a pulsed optical signal in three portions. The sample is excited by the first portion, the material response probed by the second one and the detection trigger provided by the third signal. In standard THz-TDS, the pump

pulse generates the surge current for THz emission, while the probe pulse triggers the photoconductive detector. The time delay is commonly introduced by a delay line, which can be implemented in the optical pathway to either the emitter or the detector. For convenience, the implementation of the delay line in the detector branch is natural, because this way the time trace of the THz signal is mapped in forward direction, when the delay

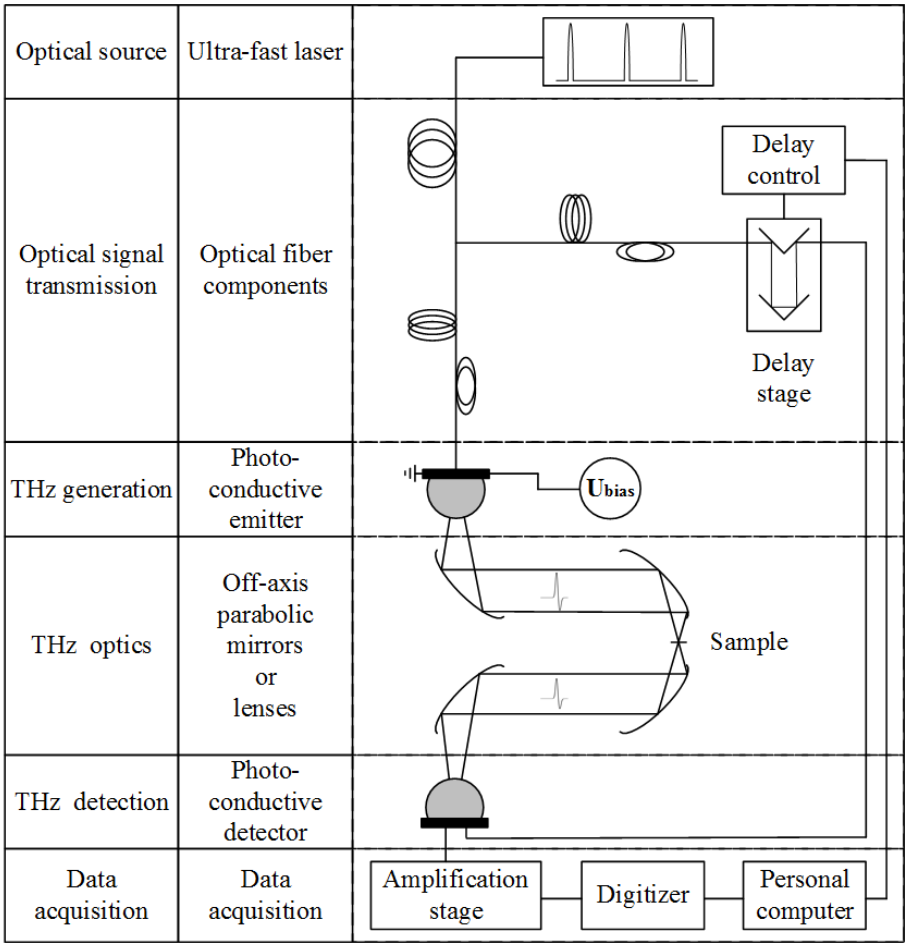

Figure 4. Sketch of a standard (fiber) THz spectrometer illustrating its basic functional elements

is increased. Besides the THz modules and the delay line, the overall arrangement consists of several functional elements, namely a signal source, transmission media to guide the optical signals and the THz wave, respectively, and data acquisition equipment. For spectroscopic measurements, a sample holder is placed at the THz beam's focal spot. A sketch of a typical standard fiber-based THz-TDS setup is depicted in Figure 4. The following paragraphs elucidate properties and functionality of each element. In the work of this thesis, all optical signal transmission is performed by fiber optics.

2.3.1 Ultrafast Lasers

THz-TDS is based on mostly visible or infrared broadband laser sources. Such lasers emit pulses in the femtosecond regime ($< 100\,fs$) at repetition rates up to $100\,MHz$. Lasers fulfilling those demands benefit from the *mode-locking* technique. Various supported longitudinal laser modes are "phase-locked" in the laser cavity employing mode-locking elements, like e.g. saturable absorbers or Kerr lenses. Those passive, intra-cavity elements reassure transmittance of high and attenuation of low intensity light in the laser resonator. High intensity spikes, which experience high transmittance occur, when the laser modes are in phase, other signals are absorbed. In consequence, the built-up light pulses are nearly transform-limited and pulse duration and bandwidth are inversely proportional: the shorter the pulse, the more locked modes are involved and vice versa. To achieve a large bandwidth at the THz generation process, a short pulse and hence broad optical bandwidth is desired.

Material	Gain Spectrum
Ti:sapphire	650 – 1100 nm
Rhodamine 6G (dye)	600 – 650 nm
Cr:LiSAF	800 – 1000 nm
Nd:glass, Nd-doped fiber	1040 – 1070 nm
Yb-doped fiber	1030 – 1080 nm
Er-doped fiber	1520 – 1580 nm

Table 1. Gain spectra of media employed in femtosecond lasers. Table extracted from [2]

Ultrafast operation demands high standards on the gain medium: Besides a broad gain, the high peak powers in short pulses require a high thermal conductivity, since fast heat flow is indispensable to prevent damage from the gain material. Furthermore, a short lifetime for excited carriers is appreciated, because long relaxation times can be a limitation to the pulse repetition rate. The traditional material of choice has been titanium sapphire (Ti:Sapphire) [77]. In this material Ti^{3+}-ions are embedded in a sapphire (Al_2O_3) matrix replacing Al_{3+}-ions, which provide the laser transitions. It has an ultra-wide gain spectrum from $650 - 1100\,nm$, a capacity to absorb up to $20\,W$ and a carrier lifetime of approximately $3.2\,ms$ [2]. Ti:Sapphire laser amplifiers, however, are bulky and expensive systems, which are sought to be replaced by cheaper and more compact sources in commercial platforms. A suitable replacement emerged with the advent of fiber lasers. The core element of such lasers are fiber ring oscillators consisting of *polarization-maintaining fibers* (PMF), which are partially doped with rare earth ions providing the optical transitions at the desired wavelength (suitable materials for ultrafast operation with their respective gain spectra

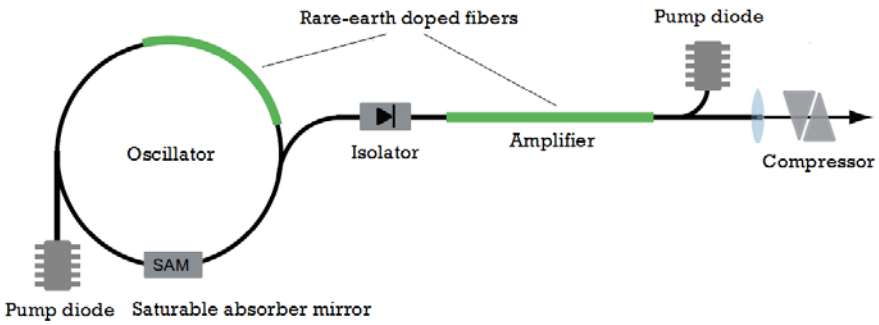

Figure 5 Core components of rare earth doped ring fiber lasers. Graphic extracted from [78]

are listed in Table 1). A scheme of the laser employed in this thesis [78] is presented in Figure 5. In such ring oscillators, pulsed operation is often enabled by a mode-locking technique employing a saturable absorber. The gain fibers are integrated in the ring oscillator as well as in a subsequent amplification stage and are optically pumped by laser diodes. Using a compressor (realized by prisms or Bragg-gratings), the pulse can be driven close toward its transform limited waveform.

2.3.2 Optical Signal Transmission

To feed the PCAs with optical pulses either free-space arrangements or, thanks to recent developments of PCAs working in the telecom bandwidth (see Chapter 2.4), an optical fiber circuitry can be chosen. Fiber technology has been introduced into the THz field for the first time in 2000 [79]. Including free-space propagation paths and beam guiding elements, the former are bulky, suffer from sensitive alignment and thus require a laboratory-like environment. In contrast, signal delivery by

optical fibers excels with its compactness, immunity to environmental distortions and easy alignment.

A shortcoming of fiber transmission lines is the bandwidth-limiting *chromatic dispersion* (CD). Propagation of femtosecond pulses through only few meters of standard *single mode fiber* (SMF) causes pulse widths to broaden unacceptably. To assure the illumination of the PCAs with shortest possible pulses, the broadening is compensated by the implementation of *dispersion compensating fiber* (DCF). This fiber type exhibits an inverse sign of the CD slope at the specified wavelength range with respect to SMF. Thus, pulses can either be re-compressed after broadening or be pre-compensated, i.e. broadened by opposite delay shifts, compared to SMF, before re-compression at standard CD. In commercial lasers, pre-compensation is often implemented, so that pulse widths are not at its minimum at the output, but after a certain distance of propagation in SMF [80]. The pre-compensation also keeps peak powers in the circuitry low and hence prevents possibly severe distortions caused by nonlinear effects. Since emitter and detector transmission lines include different free-space sections (THz beam, delay stage), the resulting asymmetry requires individual external dispersion compensation in each line. The challenge of the design of the fiber circuitry arises, when pump-probe requirements must be met: To map the THz pulse, it has to fall in the probe time window accessible by the delay stage. In practice, perfect CD compensation in both branches and time match are unlikely to occur for a configuration comprising only SMF and DCF with standard CD values. In fact, achieving the time match is

drastically eased by insertion of additional delay using *dispersion-shifted fiber* (DSF). This fiber type exhibits approximately zero dispersion at the operation wavelength and hence allows for adding delay without signal deformation. Additionally, to enhance stability, polarization-maintaining fibers have become widespread in fiber THz-TDS systems. In practice, tailoring the optical circuitry with optimum delay and dispersion compensation is rather delicate and optical pulses may suffer some degree of distortion. Figure 6 shows optical autocorrelation traces of the pulses at the line end in an experimental setup. For comparison, a theoretical reference pulse with its shape at the source is drawn to illustrate the broadening effect. A corresponding pulse could not be measured because of the laser's internal pre-compensation. The *full widths at half maximum*

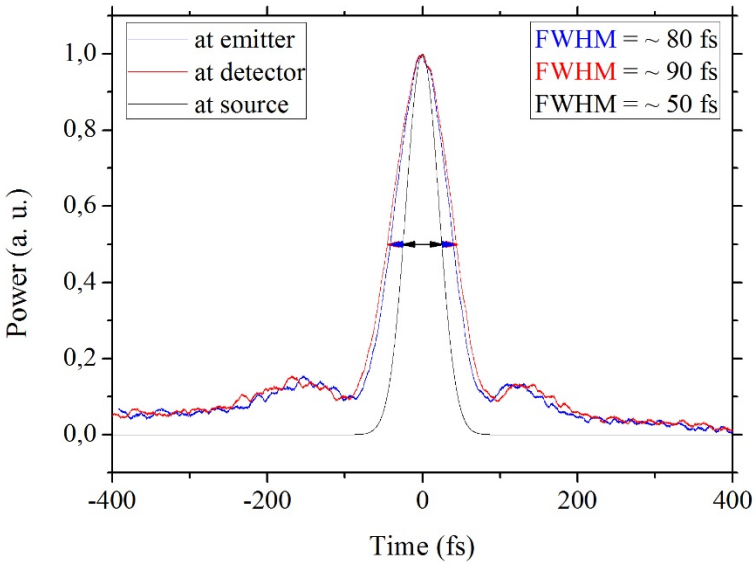

Figure 6. Autocorrelation traces of the optical pulses feeding the THz modules. The emission pulse width is drawn for comparison.

(FWHMs) of emitter and detector branch pulses broaden from initially $\sim 50\,fs$ to $\sim 80\,fs$ and $\sim 90\,fs$, respectively. Imperfect dispersion compensation affects the slope of the rising edge and at its extreme even results in pre-pulses. Besides the alignment of the THz optics (see paragraph 2.3.4), this might be a bandwidth limiting factor.

2.3.3 Optical Signal Delay

The implementation of the temporal delay has also strong implications on the system performance. Whereas for purely scientific purposes measurement times and rates use to play a minor role, for industrial-oriented THz time-domain spectrometers, data acquisition speed is a major issue. There is a tradeoff between measurement speed on the one hand and temporal as well as spectral resolution on the other.

The conventional strategy to achieve variable time delays has been the use of mechanical delay lines. Those use to be slow. In this section, a review for methods of fast and accurate delay implementation, mechanical as well as electronic, in free-air as well as in fiber transmission lines, is outlined. Additional details are provided in Chapter 4.

2.3.3.1 Mechanical Delay

The most straightforward way to introduce a dynamic time delay into an optical signal is employing moveable retro-reflectors. In general, the position of the retro-reflector is controlled with a step motor, although the use of vibrating

membranes is also possible. These are the main architectures for so-called *optical delay lines* (ODLs). The latter provide a relatively fast optical path variation, but only very short delay ranges, whereas the former, which are more common in photonics, enable the scanning of wider time delay windows, but usually at much slower speed. Time delay architectures completely based on fiber also exist and they include fiber stretchers [81] and the use of nonlinear effects in fiber to avoid mechanical parts (e.g. [82, 83]), but usually they provide limited *delay-bandwidth products*.

At sampling in the time-domain, the corresponding frequency resolution Δf after Fourier transforming is $\Delta f \approx 1/T$, where the total length of the temporal signal T is $T = (N-1) \cdot \Delta t$, with N being the absolute number of samples and Δt the sampling interval. In THz-TDS, temporal signal lengths that provide spectra with reasonable resolution (e.g. few GHz for sensing spectral lines of molecules) are of some decades of picoseconds. For this reason, stages with millimeter to centimeter range displacements are needed. Position accuracy of those is typically in the sub-micrometer range, what translates to a few femtoseconds at the delay scale.

Retro-reflectors, typically used in delay lines, consist frequently of a hollow cube with metal-coated reflective surfaces, which assure anti-parallelism between in- and outgoing beam. Scanning of the delay can be performed by a linear movement (*linear optical delay line*, LODL). Conventional LODLs are operated either manually or driven by electronic step motors, why the latter are often called *motorized optical delay lines* (MODLs).

For industrial-oriented tabletop THz equipment, such a slow, stepwise scanning method might not be suitable, so new implementations of dynamical optical pulse delays are being

sought, which maintain the desired precision, while decreasing measurement time. For example, to overcome the shortcomings of linear mechanical delay lines, *rotary optical delay lines* (RODLs) have been considered [84, 85], having less inertia-induced mechanical limitations due to uniform motion and thus the potential to operate at higher speeds. However, rotor blades usually produce a non-linear time delay progress and introduce dead times. Sophisticated geometries of rotor blades capable of producing linear time delays were designed [84, 86, 87]. Another method is to drive a slide with a retro-reflector with a voice-coil [88]. It is somehow a reasonable tradeoff between high scanning rates and long scanning windows. In this scheme, a fast linear scanning motion without digital positioning is performed. Instead, high-speed digitizing of the reflector position signal by a position sensor is required. As for vibrational delays, mechanical responses to analog drive signals are not linear and hence a linearization of the delay-axis is required at the data processing stage.

2.3.3.2 Optoelectronic Delay

In general, mechanical delay lines have some inherent drawbacks. Firstly, moving parts are subject to environmental distortions like mechanical vibrations, temperature variations, etc., which lower the reproducibility of measurements. Apart from all-fiber-based delay schemes, which typically exhibit small delay ranges, mechanical delay requires free-space propagation paths and is prone to misalignment, which can alter the transmissivity and hence introduce an additional error source. Secondly, mechanical parts might be limited by inertia and thus

restrict the scanning speed. Step motor driven delay stages perform a stepwise motion, producing dead times, while moving between target positions. This enlarges data capture times.

A further issue concerns the size of the time window to be sampled. If for the sake of high spectral resolution time windows of the order of nanoseconds are sought, device dimensions would exceed a practical size, whereas multipath architectures result in error-prone complexity and wide step widths.

For above reasons, purely electro-optic delay schemes promise stabilization and acceleration of data capture. In the following, state-of-the-art realizations of electro-optically controlled delays are described.

2.3.3.2.1 Asynchronous Optical Sampling

Asynchronous Optical Sampling (ASOPS) is a sampling technique commonly used for time-resolved measurements [89, 90, 91, 92, 93]. It is based on the interaction of laser sources with slightly different repetition rates. If one laser source provides the pump and the other one the probe pulses, the repetition rate offset of these lasers produces a dynamic time delay between respective pairs of both. The sketch in Figure 7 depicts its principle. Assumed that both repetition rates f_{pump} and f_{probe} differ by an offset Δf, the temporal increment of the delay at two subsequent detection processes is

$$\Delta t = |1/f_{pump} - 1/f_{probe}|. \tag{23}$$

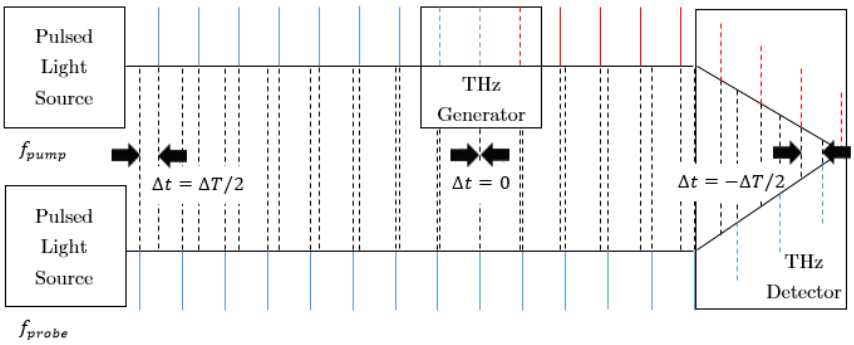

Figure 7. Working principle of ASOPS time delay generation. Two slightly detuned femtosecond lasers provide a dynamic time delay Δt between pump and probe pulses. At the beginning (right end of the sketch), probe pulses (blue dashes) arrive before ($\Delta t = -\Delta T/2$), at the end (left end), after ($\Delta t = \Delta T/2$) the THz (red dashes) pulse. The whole pulse repetition period $\Delta T = 1/f_{pump}$ is traversed in steps of $\Delta t = |1/f_{pump} - 1/f_{probe}|$.

This means that the time window $\Delta T = 1/f_{pump}$ is successively scanned by $\Delta T/\Delta t$ data points with a temporal resolution of Δt. For a small repetition rate offset Δf, $f_{pump} \approx f_{probe}$ and Δt can be approximated with $\Delta f/f_{pump}^2$. If, for instance, $f_{pump} = 100\ MHz$ and $\Delta f = 1\ kHz$, a $10\ ns$ time window is scanned in $1ms$ with a time delay increment of $100\ fs$. This is orders faster compared to a step motor driven mechanical delay line. In turn, fast scanning rates enable averaging without picking up low frequency noise components. Time window and delay step width are determined by f_{pump} and Δf, respectively, and have to be adjusted to the desired values, by either choice or varying the repetition rate of the involved lasers.

Stable operation requires phase locking of both lasers. Synchronization electronics, as well as mechanical and physical properties of the lasers, however, introduce a time uncertainty or timing jitter, which is limiting the temporal resolution. The

timing jitter at ASOPS is determined by the locking electronics and is typically $\sim 50\, fs$ [93].

2.3.3.2.2 Optical Sampling by Cavity Tuning

Optical Sampling by Cavity Tuning (OSCAT) [94, 95, 96, 97] represents an advancement based on the ASOPS principle, making one of the laser sources redundant. Instead of an incremental dephasing of two lasers, here, an unbalanced configuration of the signal transmission line provides dephasing. The laser's pulse repetition rate f_{rep} is successively varied changing the laser cavity length by a piezo driver. The technique makes use of an unbalanced optical path length: Whereas in conventional THz time-domain spectrometers portions of the same optical pulse are used to generate and detect a certain THz pulse, OSCAT uses sequenced optical pulses. A portion of a pulse indexed 'i' generates a THz pulse, which is then detected by a

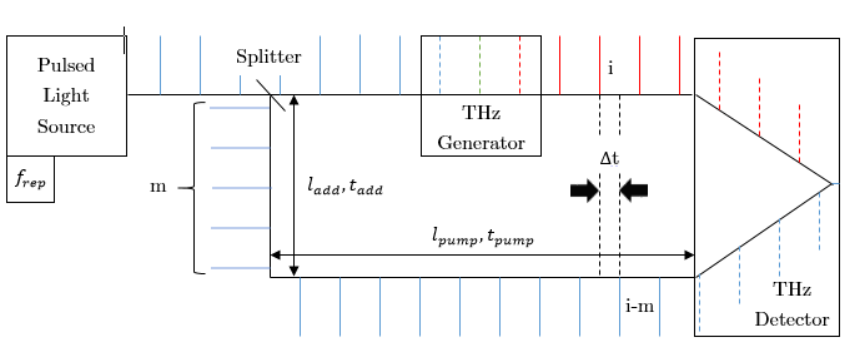

Figure 8. Principle of OSCAT time delay generation: In an unbalanced configuration, a THz pulse indexed 'i' is detected by an optical pulse with index '$i - m$'. A number 'm' of pulses propagates in an additional section of the detector transmission line with length l_{add} during a time t_{add}.

portion of a previously emitted pulse with index '$i-m$', whenever the signal transmission line, and hence propagation time, to the detector is longer than the one to the generator. A scheme to elucidate the functional principle is illustrated in Figure 8. If a pulse is split at a time $t = 0$, one portion takes a time t_{pump} to travel along the short emitter branch of length l_{pump}, consisting of the emitter optical path and the free space THz propagation path (red pulses in Figure 8), to the detector. The other portion requires a longer time $t_{probe} = t_{pump} + t_{add}$ for a longer path $l_{probe} = l_{pump} + l_{add}$ to arrive at the detector. Thus, the delay between pump and probe pulse with index *'i'* is simply $\Delta t_{i,i} = t_{add}$. However, during the time t_{add} a number of pulses m is emitted (if l_{add} is sufficiently long), so that the THz pulse with index *'i'* is probed by probe pulse '$i-m$' and the physically meaningful delay reduces to

$$\Delta t_{i,i-m} = t_{add} - m \cdot t_{rep}, \tag{24}$$

where $t_{rep} = 1/f_{rep}$ is the time interval between adjacent pulses. In contrast to conventional schemes, here the delay is shifted not by varying the time difference t_{add} with a moveable delay line, but by altering t_{rep} with a sweep of f_{rep}. Sweeping from a minimum repetition rate $f_{rep,min}$ to a maximum repetition rate $f_{rep,max}$ results in a maximum delay shift of

$$\Delta t_{shift} = m \cdot (1/f_{rep,min} - 1/f_{rep,max}). \tag{25}$$

Hence, the accessible delay range scales with the index 'm'. In turn, a specific index 'm' requires a minimum difference in the transmission line of

$$l_{add} = \frac{m \cdot c_0}{f_{rep,min} \cdot n}. \quad (26)$$

c_0/n denotes the propagation speed in the guiding medium. Eventually, the limiting factors for the scanning range are firstly the length of the delay line l_{add}, secondly the repetition rate range of the laser and the timing jitter of the laser source. Since this jitter is usually below $10\,fs$ over integration times from several MHz down to 10 kHz [94], the index 'm' can be as large as many ten thousands, if distortions of the pulses caused by dispersion and nonlinear effects in the transmission line can be satisfactorily compensated.

2.3.3.2.3 Electronically Controlled Optical Sampling

Electronically Controlled Optical Sampling (ECOPS) [98, 99, 100, 101, 102] is probably the most flexible of the opto-electronic delay techniques. Similar to ASOPS, it relies on the successive dephasing of a pair of femtosecond lasers. Whereas at ASOPS the pulse repetition rates are fixed, at ECOPS control electronics comprising a phase-locked loop (PLL) and an external voltage offset provide the dephasing. The PLL synchronizes both lasers and corrects the timing jitter, thus stabilizing the walk-off of pulses at the detector site, while the voltage offset applied to one laser sets the frequency offset. The negative feedback loop relies on piezo control of the cavity lengths of the lasers. Thus, it somehow combines elements of ASOPS and OSCAT and, consequently, the performance is noticeably improved (measurement time shortened by a factor of 50 for similar signal-to-noise ratio (SNR) in comparison to ASOPS [99, 100]). The

major drawback of such a system is the elevated cost due to the employment of two optical sources as well as control electronics for the cavity.

Whereas ASOPS uses two lasers running at their individual fixed pulse repetition rates f_{pump} and f_{probe}, ECOPS, due to its dynamical frequency control, holds f_{probe} variable. Both lasers are synchronized by locking a harmonic of their repetition rates via a PLL to a signal generator. An external voltage offset to the locking electronics then provides a variable frequency offset Δf. When $f_{probe}^{(\pm)} = f_{pump} \pm \Delta f$, the delay continuously shifts as in ASOPS. Here, however, Δf is an adjustable quantity and the dephasing or delay variation $d/dt(\Delta t)$, and hence the time step, can be controlled. For example, regions of the temporal signal with prominent significance can be scanned with slower speed and smaller steps, whereas less significant ones can be overrun.

Moreover, the dynamic repetition rate overcomes another inevitable feature of ASOPS, the fact that the scanned time window is necessarily equal to the pulse repetition period. If, for instance, the lasers are operated at $f_{rep} \approx 100\,MHz$, the delay covers the whole $10\,ns$ between adjacent pulses. In THz-TDS, typically only a time window of $50 - 100\,ps$ contains the required information, what results in a duty cycle of $5\,\% - 10\,\%$ or a dead time of $90\,\% - 95\,\%$. ECOPS, in contrast, provides the possibility to switch periodically between $f_{probe}^{(+)}$ and $f_{probe}^{(-)}$ by inversion of the external voltage offset. Hence, the sign of the dephasing is inverted, after the desired time window is scanned, and a backward scan is initiated. No scanning time unnecessarily elapses, but alternate forward and backward scanning of time traces are conducted at the speed of the modulation frequency, which is applied to the external voltage.

Like for ASOPS and OSCAT, timing jitter is a crucial issue. Therefore, the system is stabilized using a feedback system. A portion of the output of both lasers is detected by photodiodes and filtered to generate sine signal at their repetition rates. Both signals are compared with the reference signal by two double balanced mixers (DBMs), which output phase error signals. Those, in turn, are fed to amplifiers, which finally drive the piezo transducers to readjust the laser cavities' length.

2.3.3.2.4 Summary and Outlook

Concluding, optoelectronic methods provide superior performance than mechanical delay stages in many aspects, like scanning speed and robustness, having its main demerit in cost issues. ASOPS and ECOPS require two laser sources, which make up the major part of the overall system cost. OSCAT, in contrast, relies on only one optical source, but it relatively slow and suffers from pulse deformation occurring in a vastly extended fiber branch, which is hard to control. ASOPS is also limited to fixed delay ranges as consequence of the fixed pulse repetition rates of the lasers, what results in most experiments in a considerable dead time. ECOPS has overcome this drawback and enables electronic control of the scanning range. The measurement time of ECOPS underquotes the one of ASOPS by a factor of 50 [103]. Table 2 provides an overview over crucial system parameters of the respective technologies.

In [104] a novel delay scheme potentially applicable to THz time-resolved experiments is reported, which is based on a different approach making use of acousto-optical interaction in a

Technology	Scan rate	Jitter	Cost
ASOPS	~10 kHz [89]	$\sim 50\,fs$ [93]	Elevated
OSCAT	128 Hz [95]	$< 10\,fs$ [94]	Low
ECOPS	~8 kHz [103]	$\sim 50\,fs$ [100]	Elevated

Table 2. Overview of optoelectronic time delay scanning techniques

crystal (acousto-optic programmable dispersive filter, AOPDF). There, birefringence induced by an acoustic wave is exploited to split pulses into portions with orthogonal polarization, which travel at different speeds resulting as a delay at the output end of the crystal. This delay becomes variable with the displacement of the acoustic distortions. A scan rate of $34\,kHz$ has been achieved, while the precision (step width as well as jitter) could be shifted to the attosecond range.

2.3.4 Terahertz Optics

Since the optical-to-terahertz conversion efficiency using photoconductive antennas is rather low compared to other spectral ranges (the highest reported value to date is $0.075\,\%$ [59]), the overall radiated power is relatively low, commonly in the μW-range. Hence, sensitive detectors and low propagation losses are sought. Detection can be eased, when the power is bundled in a directional beam. Directivity of the THz beam is ensured using lenses and mirrors optimized for the THz range.

Refractive guidance of the beam allows for a linear experimental configuration, but requires the use of materials with

a flat optical response over very wide bands. Typical materials for THz lenses are *poly-methyl-pentene* (PMP/TPX), *high resistive float zone silicon* (HRFZ-Si) and *poly-tetra-fluoro-ethylene* (PTFE/Teflon). The choice of the appropriate lens material often depends on the quality of the flatness of the optical response in the frequency region of interest.

Alternatively, reflective optics, particularly metallic (usually gold or silver) off-axis parabolic mirrors are used to guide the THz beam. They show better bandwidth and absence of absorption and dispersion, but complicate alignment, since they do not allow for linear arrangements. However, in experimental arrangements, where collinear propagation of an optical or NIR and the THz beam is required (optical-pump-THz-probe-experiments, EOS), mirrors are inalienable due to the opacity of the lens materials at optical and NIR frequencies. In those cases, beam superposition is achieved by small holes in the mirrors, which permit the penetration of small diameter optical or NIR-beams, but maintain reflection losses of the THz beam low, due to its wider spatial extent.

2.3.5 Data Acquisition

The measurable quantity in THz-TDS is a current. In the case of EOS, this current is the result of the misbalance of two conversely wired photo-diodes. In a detection scheme with PCAs, it is the surge current arising due to the THz pulse. Amplification is required to boost the current before digitizing becomes possible. To obtain a voltage signal for sampling, low-noise trans-impedance amplifiers with a voltage output proportional to the

original current are commonly employed. Depending on the output power of PCA modules, signals have to be retrieved making use of lock-in detection when they are obscured by noise, whereas state-of-the art devices already exhibit sufficient output power for direct sampling after simple amplification.

If the signal originating from the THz-induced surge current is obstructed by noise, *lock-in-amplifiers* (LIAs) are employed to filter the noise and provide a *direct current* (DC) output proportional to the signal. LIAs make use of *phase-sensitive detection* (PSD). Therefore, the signal to be measured needs to be modulated as close as possible to its origin, so that no further noise contribution is modulated and picked up by the detector. In THz-TDS, this is traditionally realized either mechanically, by periodically interrupting the THz beam with an *optical chopper* (OC), or electronically, by modulation of the bias voltage applied to the emitter PCA.

LIAs comprise filtering stages, whose narrow low pass filters usually are simple RC-type filters, whose time constants $\tau = 1/RC$ are reciprocal to the $-3\,dB$-bandwidth. Hence, longer time constants lead to a more stable and reliable output. However, real amplitude changes in the signal are reflected at the output after several time constants, so that settling time should be taken into account at the sampling process. This sets a limitation to the sampling speed, since for fast scanning, the output is influenced by its past.

It has been a major objective to overcome the need of lock-in detection in THz-TDS to speed up data acquisition. To achieve reasonable resolution and bandwidth, a minimum trace length as well as a sufficiently small time step are required. Since data are typically captured with integration times of tens to hundreds of

milliseconds, measurement times for a single temporal trace extend to minutes and thus lie beyond acceptable values, when multiple scans are required.

Antenna modules emitting THz powers well above the noise level render lock-in detection redundant. State-of-the-art devices lately satisfy this condition and common analog-to-digital converters (ADCs) can be used for direct sampling after an initial amplification stage. Restrictions caused by filtering stages are avoided and fast scanning can be performed without any integration delay. This avoids long-term amplitude fluctuations, i.e. low frequency noise, of the optical power, which in many systems are the major source of noise. Depending on the delay method, scan rates of tens to thousands per second are possible [104].

2.3.6 Material Parameter Extraction

The purpose of THz-TDS is the extraction of optical parameters of materials in the THz domain. Though referring to the THz regime, these are traditionally referred to as *optical constants*. They are the *complex refractive index* $\tilde{n}(\omega) = n(\omega) + i\kappa(\omega)$, consisting of a real part $n(\omega)$ (*refractive index*) and an imaginary part $\kappa(\omega)$ (*extinction coefficient*), which is proportional to the *absorption coefficient* $\alpha(\omega)$ via $\alpha(\omega) = 2\omega/c \cdot \kappa(\omega)$ with c being the vacuum speed of light.

To extract the optical constants, experiments in two different modes, transmission or reflection geometry, can be performed. Whereas in THz reflection spectroscopy a beam reflected from a sample surface is analyzed, in transmission spectroscopy the beam

propagating through the sample is detected. Both allow for the extraction of the full set of the optical parameters. In reflection geometry, due to experimental requirements often beam-sample surface angles deviate from normal incidence, which adds computational complexity. However, systems including reflection geometry at normal incidence have been developed, e.g. in [105]. In transmission geometry, in turn, analysis of highly absorbing or thick sample might become problematic, since measurement results always have to be regarded in the light of the maximum available *dynamic range* (DR). The DR is the maximum quantifiable signal change of the measurement and is calculated taking the ratio of the maximum amplitude A_{max} and the rot mean square of the noise background ΔA_{rms} of the measurement [106]:

$$DR = \frac{A_{max}}{\Delta A_{rms}} \tag{27}$$

It can become the limiting quantity for the valid data range of the absorption coefficient, when strong absorption occurs and attenuates the transmitted signal below the noise level. In this case, the outcome of the analysis would yield an erroneous absorption coefficient equal to a maximum measurable absorption coefficient α_{max} that reduces the signal exactly to the noise level [107]. In reflection geometry, in contrast, the largest detectable absorption coefficient depends on the measurement reproducibility.

Parameter extraction is conducted analyzing the *transfer function* $H(\omega)$ of the sample, which is the quotient of the frequency spectra corresponding to temporal traces of the THz signals with and without the sample in the THz beam path. This

procedure has a systematic vulnerability, because conditions may change from one capture to another. This problem has been addressed, for instance, with the establishment of *Differential Time-Domain Spectroscopy* (DTDS) [108, 109, 110], which simultaneously captures sample and reference data, or in other words measures a differential signal.

Since the PCA represents a coherent detector, amplitude and phase of the signal can be recorded and converted into spectral data via a Fourier-transform (FT). In the frequency domain, a simple division of the complex spectra yields the transfer function of the sample. In the simplest case, the analytical expression

$$H(\omega) = \tau\tau' \cdot exp\left\{-\kappa(\omega)\frac{\omega d}{c}\right\} \cdot exp\left\{-i[n(\omega) - n_0]\frac{\omega d}{c}\right\} \tag{28}$$

can be derived for the transfer function, where τ and τ' denote the transmission coefficients at the air-sample and sample-air interfaces, respectively, and their product can be expressed as

$$\tau\tau' = \frac{4\, n(\omega) n_0}{[n(\omega) + n_0]^2}. \tag{29}$$

At this point, it is important to bear in mind that this expression is approximate and in some cases, for example for highly transparent thin films, where multiple reflections might overlap, expressions that are more accurate have to be considered. Dielectric parameters can be extracted using the following expressions

$$n(\omega) = n_0 - \frac{c}{\omega d}\phi(\omega), \tag{30}$$

where $n_0 \approx 1.00027$ is the refractive index of air and $\phi(\omega) = \angle H(\omega)$, and

$$\kappa(\omega) = \frac{c}{\omega d} ln\left\{\left[\frac{4\, n(\omega) n_0}{[n(\omega) + n_0]^2}\right] - ln|H(\omega)|\right\}. \quad (31)$$

Although, algorithms that are more accurate have been developed, taking into account signal echoes (Fabry-Pérot-oscillations) [111, 112, 113, 114, 115, 116] or providing increasing accuracy with an iterative method [115].
Furthermore, time-domain spectroscopic measurements represent a powerful tool to determine the sample thickness [111, 117, 118] or even layer thickness in multilayer structures [119]. Moreover, it has been employed to measure the birefringence of materials [120].

2.4 Terahertz Technology in the Telecom Band

The first material employed as photoconductor in optoelectronic THz-generation was RD-SOS [121, 122]. Shortly after, LTG-GaAs became the material of choice [123, 124]. Both materials exhibit electronic energy bandgaps corresponding to optical wavelengths around $800\, nm$. The typical pulsed laser source suitable for optical excitation at these wavelengths is the Ti:Sapphire laser, a rather expensive and bulky apparatus, which makes the massive deployment of this sensing tool difficult.

A large jump from scientific in-the-lab THz equipment toward industrial sensing instruments has been made with the development of photo-conducting materials suitable as PCAs

working in the band of telecom wavelengths. Thus, Ti:Sapphire lasers can be replaced by cost-effective 1550 nm fiber lasers. These materials include Fe-ion-implanted LTG-InGaAs [125], annealed, Fe-ion-implanted InGaAs (only detector) [126], LTG-GaAsSb [127], and eventually Be-doped LTG-InGaAs/InAlAs super-lattice structures [80] or the state-of-the-art InGaAs/InAlAs super-lattice structures grown at elevated temperatures [128]. The advent of those materials enabled the use of optical fibers as signal distribution medium and the exploitation of off-the-shelf devices based on mature telecommunication technology. Mode-locked fiber-ring lasers (see Section 2.3.1) designed (e.g. fiber-pigtail output) and optimized (e.g. dispersion pre-compensation) for transmission through optical fibers were employed.

The LTG-InGaAs/InAlAs material system was first employed in an all-fiber broadband THz time domain spectrometer in [80], as well as in a CW system [129]. The commonly used bulk photoconductive material has been replaced by a *multilayer hetero-structure* (MLHS). Ongoing development of the material, as well as device structure, took place, which lead to a manifold increase of power and improvement of dynamic range, resulting in state-of-the-art systems, as described in [88, 130].

The THz modules, which have been employed and investigated throughout this work, were commercial devices purchased from *Menlo Systems GmbH* and *Toptica Photonics AG*. Since their appearance in 2008, they underwent a continuous optimization process, which is recorded in detail in [131].

2.4.1 Photoconduction at 1550 nm Excitation

The development of photoconductive materials suitable for THz generation and detection aims at achieving low dark conductivity, high carrier mobility under illumination and short carrier lifetimes. In emitters, a low dark conductivity matters to make the material withstand high bias fields. In detectors, it keeps the dark current low and thus assures a high DR. Low dark conductivity is obtained, when the residual carrier concentration is low. Utilizing *molecular beam epitaxy* (MBE) growth, low residual carrier concentrations are usually achieved at elevated growth temperatures of several hundred degrees, which favor stoichiometric growth, where constituents are very mobile at the docking and build up a highly regular atomic lattice. Low growth temperatures, however, favor the creation of carrier-donating lattice impurities, what results in an elevated residual carrier concentration. Implantation of appropriate dopants reduces the amount of residual carriers. Hence, low dark currents require either high growth temperatures or doping. High carrier mobility materials, in contrast, exhibit low scattering rates and hence a small amount of defects. Therefore, elevated growth temperatures are favored, but rather low doping levels are desired. Desired short carrier lifetimes, however, require sufficient recombination or trapping centers, i.e. lattice impurities, what in turn is favored by low temperature growth or defect incorporation. Eventually, designing materials for ultrafast photoconductive switches involves a tradeoff among these parameters.

Several mechanism generally contribute to detract carriers from the CB and potentially determine the lifetime. Direct e-h-recombination, which is a radiative process that combines CB

electrons with VB holes, is not suitable for THz PCAs, since characteristic lifetimes lie typically in the pico- to nanosecond range. Auger processes involve three particles and have a low capture cross section. Considering quantum mechanical scattering probabilities, recombination rates in the InGaAs/InAlAs-PCA-material used in this work are not fast enough ($\sim 10\,ps$) below excitation densities of $10^{19}\,cm^{-3}$ [132] and can be neglected for common power irradiation of few mW, exciting carrier densities of only about $10^{17} - 10^{18}\,cm^{-3}$ [57]. As third process, SRH-recombination, also contributes to the carrier relaxation. Here, CB electrons undergo a phonon-assisted capture by defect states energetically located in the bandgap, before relaxation into the VB occurs. This non-radiative trapping happens on the picosecond time scale and below, as long as the corresponding trapping centers are not saturated [57].

LTG GaAs, MBE-grown at temperatures $\leq 200℃$, the long-time material of choice, exhibits excess arsenic due to its non-stoichiometric growth at this low temperature. Arsenic anti-site defects on gallium lattice positions (As_{Ga}) donate excess electrons to the lattice and leave positively charged defects behind. Through an annealing process free electrons are diffused until they recombine with gallium vacancies (V_{Ga}) acting as electron acceptors. This reduces the residual carrier concentration to an acceptable level, while the positively charged arsenic anti-sites (As_{Ga}^{+}) increase the electron capture cross section in contrast to neutral ones, what creates efficient trapping centers and hence short lifetimes.

A potentially suitable photoconductive material to be bridged by the telecom wavelength of $1550\,nm$ is LTG-$In_{0.53}Ga_{0.47}As$. Compared to LTG-GaAs, LTG-InGaAs has a sufficiently small

bandgap of $E_B = 0.74\ eV$. However, As_{Ga}^{+}-defects in LTG-InGaAs lie only $91 - 150\ meV$ below the CB edge and hence are subject to thermal activation, resulting in a residual carrier concentration of $n \sim 10^{17} - 10^{18} cm^{-3}$ [128], which impedes use as a photoconductive switch. Implanting Beryllium dopants as free electron acceptors lowers the carrier concentration, but thermal activation of trapped electrons remains a problem. Furthermore, the doping lowers significantly the electron mobility one the one hand and the photon absorbance on the other. The Be-concentration affects significantly the carrier scattering or momentum relaxation time, which falls in the $5 - 50\ fs$-range [57]. A detailed analysis of the impact of Be-doping on the carrier dynamics is provided in [133]. A solution to this problem has been found in the growth of an MLHS, in which hundred layers of $12\ nm$ thick photo-conducting InGaAs-layers are sandwiched by $8\ nm$ thick $In_{0.52}Al_{0.48}As$ barriers [80]. InAlAs itself does not contribute to a photocurrent, since its bandgap of $E_B = 1.46\ eV$ is transparent to $1550\ nm$ light, but reduces the dark current by a rapid free carrier capture via tunneling processes from adjacent InGaAs-layers. Due to the CB step of $\Delta E_C = 0.44\ eV$, the defect levels in InAlAs are mid-gap and thermal activation is disabled. Hence, the electrons are trapped in the deep InAlAs-traps, while conduction electrons face low resistivity and are highly mobile in the InGaAs-layers.

In another approach [134], MBE-growth of the InGaAs/InAlAs-MLHS at high temperatures has been conducted. At growth temperatures between $300 - 500℃$ bulk InGaAs has a residual carrier concentration of only $10^{14} - 10^{15}\ cm^{-3}$, which cause a Hall-mobility of $\mu_H = 10^4 cm^2/Vs$, corresponding to a mean scattering time of $\delta\tau = 250\ fs$, according to the Drude-

model. The rise of mobility in contrast to LTG-InGaAs proves beneficial for PCAs, whereas the scattering rates are unacceptably low regarding carrier lifetimes. The solution comes with the InAlAs barrier layers: InAlAs shows a tendency to alloy clustering in the $300 - 500℃$ temperature range. Those nanometer-size InAs- and AlAs-like regions represent lattice defects, which lie energetically mid-gap in InAlAs, showing energies $0.6 - 0.7\,eV$ below the CB edge. In a nanometer-sized MLHS, the wave functions of CB electrons in InGaAs have considerable overlap with those trap states in InAlAs and hence electron capture by tunneling into the cluster traps is enabled. The deep trap states promise high resistivity, since they prevent thermal re-excitation. The residual carrier concentration of the MLHS is $n < 10^{12} cm^{-3}$, the Hall-mobility decreases to $\mu_H \cong 1500 - 3000\,cm^2/Vs$, which is still almost an order higher than in the LTG-InAlAs. This increase of mobility in comparison to LTG-InGaAs outweighs the increase of resistivity from $0.01 - 1\,\Omega cm$ to approximately $5800\,\Omega cm$. It has thus become possible to simultaneously grow high mobility layers with few scattering centers on the one hand, and highly resistive barrier layers on the other hand, at the same temperature. The high-temperature grown MLHS exhibits higher photocurrents and a higher breakdown voltage, so that bias fields of the order of $10\,kV/cm$ can be applied in the emitter. A mean power at pulsed THz operation of $64\,mW$ with a conversion efficiency of $2 \cdot 10^{-3}$ has been achieved [56]. At the same time, the spectral bandwidth only shrinks slightly, since the trap density is smaller and the trapping time longer than in the LTG hetero-structure.

2.4.2 Antenna Design

Besides the evolution of the photoconductive material, a geometrical optimization has taken place, with respect to early realizations of THz emitter and receiver structures [135]. Traditionally, the contacting of the photoconductive material has been realized by deposition of planar gold electrodes on top of the functional material. This is technologically a simple method, but entails certain disadvantages. Firstly, the electrodes sandwich some non-functional material outside active photoconductive region, what unnecessarily contributes to the dark current. Secondly, the in-plane component of the bias field in deeper layers is small and the electron acceleration obstructed. Furthermore, the current flow is hindered at layer interfaces, which represent resistive barriers. These problems have been addressed, when the functional material has been treated by *chemically assisted ion-beam etching* (CAIBE) to take the form of a *mesa-ridge*, which permit lateral contacting. Consequently, the carrier transport takes place in-plane with high field strengths even in deeper layers. Since the field distribution is uniform, carrier trajectories do no longer cross layer interfaces. Photo- as well as dark currents were raised by a factor $\times 5$. At the same time, removal of functional material off the laser spot caused a reduction of the dark current by a factor $\times 120$. This resulted in an overall boost of ca. $\times 25$. Besides, also output power and bandwidth benefit.

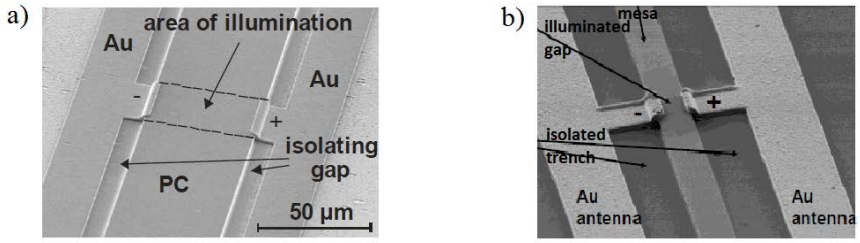

Figure 9. SEM-pictures of a) emitter chip and b) receiver chip. Pictures are taken from the Application Note of Menlo Systems GmbH.

All devices, which have been employed in this work, were fabricated by *Menlo Systems GmbH* or *Toptica Photonics AG,* based on similar concepts. Thus, all of them featured the mesa-ridge design implemented in their antenna structure. *Scanning electron microscopy* (SEM) pictures of the antennas are illustrated in Figure 9. The emitter PCAs used a strip line design with an electrode distance of $25\ \mu m$, formed by the ridge width and hence applicable bias voltages lead to electric field strengths of few kV/cm. The receiver modules had a dipole-structured antenna with a smaller gap of only $10\ \mu m$. For both the focal spot of the excitation beam had a diameter of around $10\ \mu m$.

3. Combination of Continuous and Pulsed Optical Waves

THz spectroscopy can be divided into two approaches: time-domain (pulsed as reviewed in Section 2.2.2 and based on femtosecond lasers) and frequency-domain (continuous as reviewed in Section 2.2.1 and based on CW optical sources).

In 2010, Ryu and Kong performed an experiment, which apparently showed that an additional CW optical signal at 780 nm feeding a pulsed THz time-domain instrument based on an LTG-GaAs emitter PCA resulted in a boost of THz power [136]. It was an unexpected result and no physical explanation of the underlying mechanism could be provided.

A set of measurements trying to replicate the observed effect in a 1550 nm fiber-based system showed the opposite outcome: a continuous optical wave reduced the amplitude of the measured photocurrent not only in the emitter, but also more strongly in the receiver.

In this chapter, the injection of a CW optical signal on a pulsed PCA-based THz-TDS system is studied and the underlying physical mechanism is described. Finally, it is shown how this effect could be used to implement an all-optical control

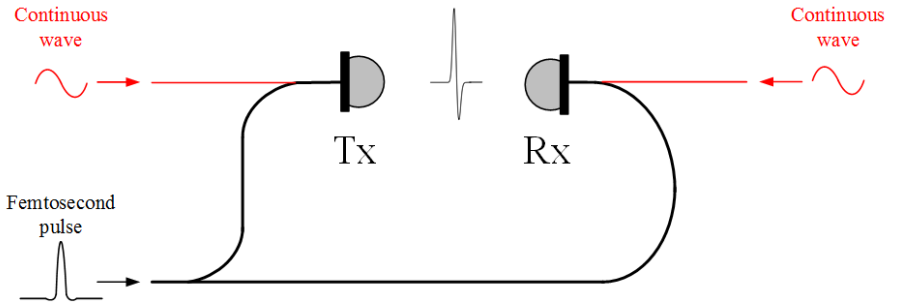

Figure 10. Principal idea of manipulating the performance of a THz TDS system by injecting a CW into either the emitter/transmitter (Tx) or receiver (Rx) fiber pathway

of a PCA. Figure 10 shows the block diagram used to study the manipulation of the performance of a THz-TDS system through CW injection.

3.1 Experiment

If a CW signal is superposed to the train of femtosecond pulses that conventionally feeds the PCA modules, a reduction in the measured photocurrent was observed. Experiments were carried out with a fiber-based THz-TDS setup (depicted in Figure 11) that was mounted with commercial components. The key components were THz modules described in Section 2.2.2 and the optical source described in Section 2.3.1. The CW signal from the laser source was injected into either the emitter or the receiver PCA. Standard pulsed-only operation was taken for reference.

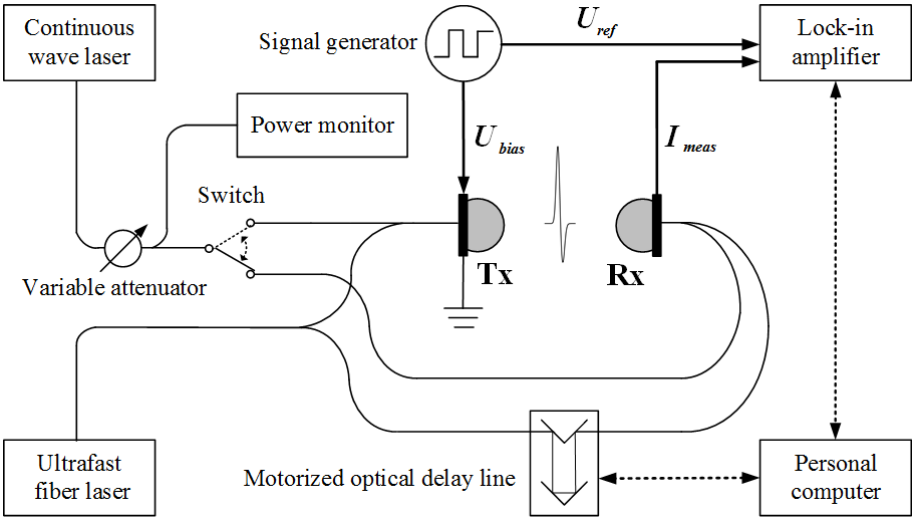

Figure 11. Experimental setup: The THz emitter and receiver modules were fed with femtosecond pulses emitted by the ultrafast fiber laser as in standard operation conditions. Additionally, a CW is injected into either the Tx or Rx.

3.2 Results

In Figure 12, the captured time-domain data of these three configurations (CW injection into the emitter, receiver or no CW injection) are presented. It can be seen that, in contrast to the observations made in [136], CW injection into either PCA reduces the photocurrent considerably. For a fixed optical CW power, the amplitude reduction is larger, when the CW is injected into the receiver. Figure 13 shows a set of time traces captured for successively increasing CW optical powers injected into the receiver PCA. Raising the power from zero to the level of the pulsed signal, the detected current amplitudes are continuously reduced. Normalization of the time traces to their peak

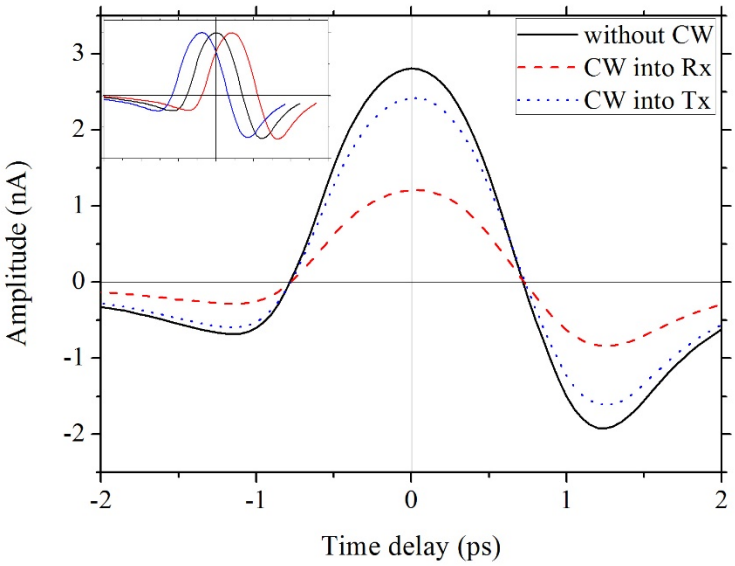

Figure 12. Detector photocurrents when the THz time-domain spectrometer is operated conventionally (black solid line), and when additional optical CWs are injected into either the emitter (blue dotted line) or the receiver (red dashed line). Inset: Normalized waveforms

amplitudes shows that the waveform is preserved (inset of Figure 13). Figure 14 shows spectra corresponding to current transients captured with absent, intermediate and high (with respect to the pulsed optical power) CW powers at the detector. Within the limit of the available resolution ($\Delta f = 20\,GHz$) and apart from a slight degradation of the DR due to reduced amplitudes and additional laser noise, the corresponding spectral data show no significant differences, i.e. no spectral redistribution of power is observed.

The peak amplitudes of the photocurrent with respect to the ratio of CW to pulsed power are presented in Figure 15. The amplitude decreases with rising CW power, following a reciprocal

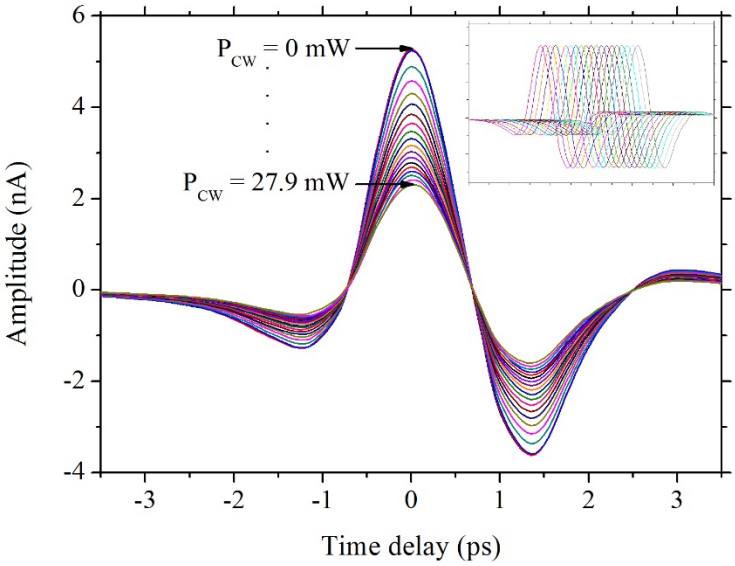

Figure 13. THz time traces captured under variation of additionally injected CW optical power into the receiver PCA. The power was successively increased from $0\,mW$ to $27.9\,mW$. Inset: Normalized waveforms.

curve. At equal power levels (P_{CW} / P_{Puls} $\cong 1:1$) this reduction, is about $35\,\%$, if the injection is applied to the receiver. If the CW injection is applied to the emitter, the amplitude reduction is noticeably smaller (around $8\,\%$). Replacing the CW signal by an amplified spontaneous emission (ASE) noise signal of equivalent power yields similar results (inset of Figure 15).

In conventional THz-TDS, increased optical power raises the detected photocurrent, in the accessible power regime to tens of mW. However, the injection of the CW in the experiments led to a considerable reduction of the measured detector signal. Measurements of the average DC conductivity of the PCAs, when

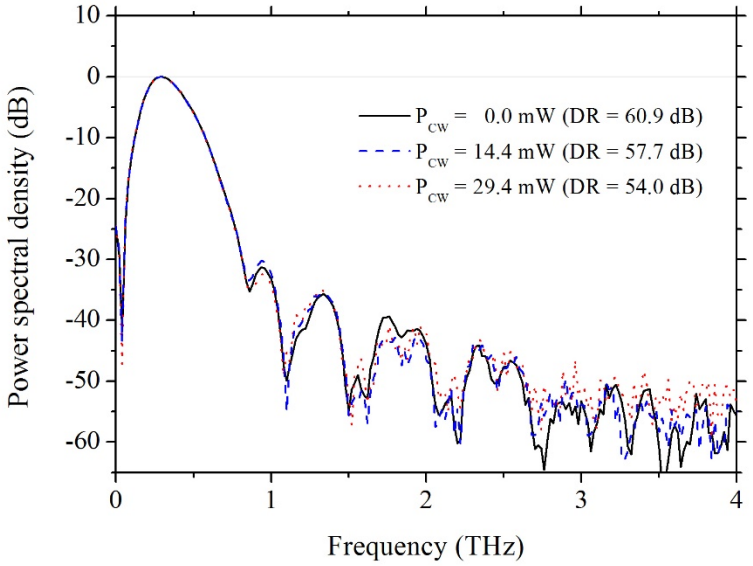

Figure 14. Fourier-spectra of detector currents with absent, intermediate and high CW optical powers injected into the receiver PCA. Dips in the spectra are caused most likely by filtering due to delayed signal portions. Possible candidates for their origin are residual polarization mode dispersion (PMD, see Section 5.3.5) in the fiber patch cords and imperfect alignment of the THz optics.

exposed to the CW, instead, unsurprisingly show an increase with rising optical CW power.

3.3 Discussion

Optimization in photoconductive switching usually targets the enhancement of key parameters of photoconductor materials, which principally are the dark resistivity and carrier mobility. On a microscopic scale, these quantities relate to time constants, i.e. mean times between microscopic events, and effective masses of

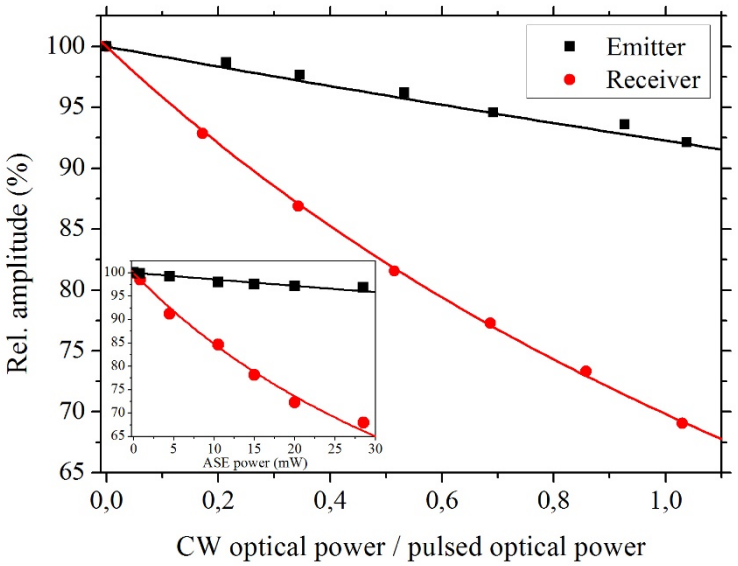

Figure 15. Detector current amplitude vs. continuous to pulsed wave power ratio. Data are fitted with a reciprocal function. Inset: Replacing the CW power by an equivalent ASE optical amplifier noise power

the involved charge carriers, which crucially determine the carrier dynamics. The carriers' effective mass depends on their type (electron/hole), the potential curve of the crystal lattice and on their energy. Whereas carrier type and potential are intrinsic properties of a semiconductor, excitement with different excitation energies can lead to different effect masses. As described in Section 2.4.1, there are several radiative and non-radiative relaxation mechanisms. In state-of-the-art photoconductive switches, the SRH-recombination is the dominating, fast process, which determines carrier lifetime. Choosing growth conditions, like substrate selection, compound ratio, doping level, temperature, etc., provides static control of the carrier lifetime. Dynamic control can potentially be gained by

populating excessively energy levels involved in the relaxation processes.

Besides recombination, the carrier dynamics also comprise scattering, which can be expressed in the momentum relaxation time $\delta\tau$ of the carriers, a characteristic mean time between scattering events. The carriers' momentum relaxation time constant is determined by the number of potential scattering targets, which are potentially crystal impurities or the lattice vibrations, so-called phonons. The phonon density can be regarded as a quantity linked to the heat of the crystal lattice. Implantation of crystal impurities represents a static control of the amount of scattering, whereas the density of phonons can be dynamically controlled by the incident optical flux.

Bearing this in mind, several processes have been contemplated as the possible cause of the effect observed in Section 3.2. Firstly, it is figured out, how the CW affects the generation process. Since the radiated THz field strength $E_{THz}(t)$ scales with the temporal variation of the photo-induced current density $d/dt\ (j(t))$ in the emitter PCA [2] and the latter with the free carrier density $n(t)$ as well as with the conduction band carrier velocity $v(t)$, $E_{THz}(t)$ is proportional to the carrier accumulation rate in the conduction band $d/dt\left(n(t)\right)$ and the corresponding carrier acceleration $d/dt\ v(t))$ [137]:

$$E_{THz}(t) \propto \frac{d}{dt} j(t) = \frac{d}{dt}\left(en(t)v(t)\right) = e\left(v(t)\frac{d}{dt}n(t) + n(t)\frac{d}{dt}v(t)\right). \tag{32}$$

The time-dependence of the quantities $n(t)$ and $v(t)$ is given implicitly via the incident optical power, so the equation becomes:

$$
\begin{aligned}
&E_{THz}\left(P_{opt}(t)\right) \\
&\qquad \propto \left(v\left(P_{opt}(t)\right)\frac{d}{dt}n\left(P_{opt}(t)\right)\right. \\
&\qquad \left. + n\left(P_{opt}(t)\right)\frac{d}{dt}v\left(P_{opt}(t)\right)\right) \\
&\qquad = \left(v\left(P_{opt}(t)\right)\frac{\partial n\left(P_{opt}\right)}{\partial P_{opt}}\frac{dP_{opt}(t)}{dt}\right. \\
&\qquad \left. + n\left(P_{opt}(t)\right)\frac{\partial v\left(P_{opt}\right)}{\partial P_{opt}}\frac{dP_{opt}}{dt}\right).
\end{aligned}
\tag{33}
$$

In the following, a prime denotes quantities after taking into account the added CW. An additional CW adds the optical power P_{CW} to the pulsed optical power $P_{puls}(t)$ to make up the total incident optical power $P'_{opt}(t)$. On the time scale of the pulse duration, much longer than the CW's optical cycles, P_{CW} is considered constant. Thus, quasi-static CW power leaves the temporal derivatives of the pulses unchanged:

$$
\frac{dP'_{opt}(t)}{dt} = \frac{dP_{puls}(t)}{dt} + \underbrace{\frac{dP_{CW}}{dt}}_{=0} = \frac{dP_{puls}(t)}{dt} = \frac{dP_{opt}(t)}{dt}. \tag{34}
$$

With Equation (34) the expression for E'_{THz} becomes:

$$
\begin{aligned}
&E'_{THz}(P'_{opt}(t)) \\
&\qquad \propto \left(v'\left(P'_{opt}(t)\right)\frac{\partial n'(P_{opt})}{\partial P_{opt}}\frac{dP_{opt}(t)}{dt}\right. \\
&\qquad \left. + n'\left(P'_{opt}(t)\right)\frac{\partial v'(P_{opt})}{\partial P_{opt}}\frac{dP_{opt}}{dt}\right).
\end{aligned}
\tag{35}
$$

The carrier population $n'\left(P'_{opt}(t)\right)$ has the two contributions $n\left(P_{puls}(t)\right)$ and $n(P_{CW}(t))$ with the latter term always being an

increment. Hence, it holds $n'\left(P'_{opt}(t)\right) > n\left(P_{opt}(t)\right)$. In the non-saturation regime $n\left(P_{opt}(t)\right)$ is assumed linearly growing with optical power and the respective partial derivative $\partial n'(P'_{opt})/\partial P'_{opt}$ equal to $\partial n(P_{opt})/\partial P_{opt}$. Comparing the terms of Equations (33) and (35) makes clear that $E'_{THz}(t) < E_{THz}(t)$ can only hold, if either the carrier velocity or its derivative produce a smaller contribution than their unprimed counterparts do.

At the detection process, it becomes even clearer that the velocity term, but not the carrier density one, must be the source of the reduction of the detected current $j'_{rec}(t)$, because it scales with $n'\left(P_{opt}\right)$:

$$j'_{rec}(t) \propto en'(t)v'(t). \tag{36}$$

The proportion of CW-generated conduction band carriers contributing to the THz current is assumed comparatively low, because of the fast trapping rate and the small ratio of optical pulse duration and pulse cycle. In contrast, when an average DC photocurrent is measured, the total number of CW-excited carriers contributes to the current, so that a higher $n'(t)$ dominates over the shrinking velocity term. However, due to the relatively fast trapping rate and slow electron-hole-recombination rate, the CW potentially accumulates a considerable population in the trap states and hence slow down the trapping by trap saturation [138]. This, in turn, would result in a carrier accumulation in the conduction band during the pulse, what provably leads to higher photocurrents, but extended lifetimes and hence narrower spectra. Consequently, if the CB electron density $n'(t)$ were dominant, only an amplitude increase would be measured.

According to the Drude-Lorentz model of carrier transport, which is widely used for modelling THz photo switches, because under conventional operation conditions carrier densities are high enough to restore equilibrium on a femtosecond timescale [139], $v(t)$ is expressed as the product of the elementary charge e, the carrier momentum relaxation time $\delta\tau$, the driving electric field E and the inverse effective mass ${m_{eff}}^{-1}$: $v(t) = e \cdot \delta\tau \cdot E \cdot {m_{eff}}^{-1}$ To lower $v'(t)$ with respect to $v(t)$, the additional CW lowers the factor $\delta\tau \cdot E \cdot {m_{eff}}^{-1}$.

The most straightforward explanation is to assume a reduced local electric field through field screening occurring in THz photoconductive antennas [139, 140, 141]. Bias field screening occurs due to space charge fields, which attenuate the external field to make up a lower local field. Since CW-excited carriers are not supposed to accumulate in the conduction band, but to populate rather the trap states, they are localized and hardly able to alter the screening potential. Besides, the minor number of CW-excited carriers remaining in the conduction band or lifted into the conduction band within a narrow timeframe around the pulse is a negligible fraction compared to the pulse-excited carriers and cannot explain the observed amplitude variations by screening. Moreover, as it has been shown that field screening leads to reshaping of the waveforms [140, 141], but the experimental results do not reveal any reshaping within the resolution limits. Consequently, field screening is excluded as a possible origin of the measured amplitude reduction. Furthermore, the receiver PCA lacks a static external electric field, the driving force able to build-up a space charge field. Thus, only the THz-field itself could create such, but since its strength

is orders smaller than the emitter's bias field, it does not explain the higher impact of the CW in the receiver.

Observations of varying conductivity due to dynamic average effective masses have been discussed in the context of THz wave emission [142, 143, 144, 145, 146]. In those, energy-dependent excitations into satellite-valleys and intra-band relaxation have been declared responsible for these alterations. In present experiments, however, the energies of the optical CW as well as of the pulsed photon energy is held constant and additional field screening by the CW is negligible, thus, the distribution of electrons in the conduction band states is maintained and the average m_{eff} is not subject to change.

A different situation can emerge, when the excitation wavelength is tuned. Higher energy transfer might potentially involve the population of satellite valleys and thereby alter the

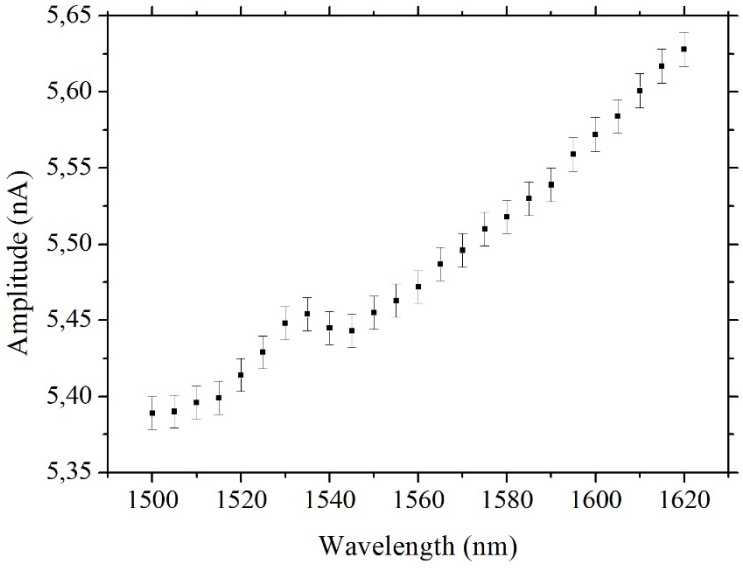

Figure 16. Photocurrent amplitudes vs. wavelength of the additional CW

momentum and hence effective mass distribution of the carrier ensemble. Indeed, a variation of the amplitudes with the CW wavelength has been found (depicted in Figure 16).

However, since the onset of electron transfer to satellite valleys in InGaAs starts at $\sim 1.6\,eV$ [147] and photon energies applied in the experiment have been far below $(0.76 - 0.83\,eV)$, the observed variations cannot be attributed to carrier redistribution. Below the onset of inter-valley transitions at $1.6\,eV$, in [147] THz amplitudes have been found to rise (fall) with increasing photon energy (wavelength), what contrasts the tendency observed in Figure 16 , where amplitudes were lowered most for high photon energies. In presented measurements, it seems that increasing photon energies (decreasing wavelengths) are more likely absorbed and cause a higher impact (lowering) on the amplitude. However, the energy range in the experiment is not too close to $1.6\,eV$, so that both results might be valid.

Increasing the CW optical power, however, leads to heating, which on a microscopic level translates to a decrease of the momentum relaxation time $\delta\tau$, because the number of scattering events is raised, when optical energy is transferred to the crystal lattice. Scattering is supposed to increase due to the excitation of *longitudinal optical* (LO)-phonons and a higher carrier density [137, 148]. Hereby the former make the major contribution, since Monte Carlo-simulations have shown that carrier-to-carrier-scattering plays only a minor role, being of elastic nature and thus only causing slight angular deviations of carrier trajectories [149]. Whereas a rise of pulsed optical power merely results in an increase of involved carriers, CW-excited carrier contribution is negligible.

Although in materials with small bandgaps, like InGaAs, heating by elevated bias voltages or optical fluxes can result in further heating by activation of intrinsic carriers [47, 150], this effect is not relevant in the devices reported here as indicated by the absence of runaway effects at certain power and by the fact that the reduction in amplitude is more severe for the receiver than for the emitter.

Experimental results were compared with an analysis of the response of photoconductive switches at THz generation and detection, provided by Duvillaret et al. [60]. Therein, the following dependences of the photocurrent in the receiver on all the time constants can be pointed out like:

$$\begin{aligned} & j_{rec}(t, \tau_{em}, \tau_{rec}, \delta\tau_{em}, \delta\tau_{rec}) \\ & \propto \frac{\delta\tau_{em}\tau_{rec}^2\delta\tau_{rec}}{(\tau_{rec}+\delta\tau_{rec})(\tau_{em}+\tau_{em})\left(\frac{\tau_{em}\delta\tau_{em}}{\tau_{em}+\delta\tau_{em}}+\tau_{rec}\right)} \\ & \cdot f(t, \tau_{em}, \tau_{rec}, \delta\tau_{em}) \end{aligned} \tag{37}$$

in the time-domain and

$$\begin{aligned} & j_{rec}(\omega, \tau_{em}, \tau_{rec}, \delta\tau_{em}, \delta\tau_{rec}) \\ & \propto \frac{\tau_{rec}^2\delta\tau_{rec}}{(\tau_{rec}+\delta\tau_{rec})(1+i\omega\tau_{rec})} \\ & \cdot \frac{\tau_{em}^2\delta\tau_{em}}{(\tau_{em}+\delta\tau_{em})(1-i\omega\tau_{em})\left(1-i\omega\frac{\tau_{em}\delta\tau_{em}}{\tau_{em}+\delta\tau_{em}}\right)} \end{aligned} \tag{38}$$

in the frequency-domain, where τ_{em} and τ_{rec} denote the electron lifetimes, $\delta\tau_{em}$ and $\delta\tau_{rec}$ the momentum relaxation times of emitter and receiver, respectively. In the first expression, the term denoted $f(t, \tau_{em}, \tau_{rec}, \delta\tau_{em})$ abbreviates a group of exponential and inverse error functions, in which only τ_{em}, τ_{rec} and $\delta\tau_{em}$, but not $\delta\tau_{rec}$ appear as arguments. Equations (37) and (38) were used

to compute temporal pulse forms and corresponding Fourier spectra under variation of carrier lifetimes and momentum relaxation times. In the regime of carrier lifetimes typical for LTG-InGaAs/InAlAs ($\sim 0.7\,ps$), an increase in carrier lifetime results in reshaping the pulse form as can be seen in Figure 17a) and Figure 17b). Whereas in the receiver, for increasing carrier lifetimes, the leading positive peak is lowered and its energy transferred increasingly to the negative peak, in the emitter, exactly the opposite takes place; the positive peak grows, while the negative one reduces. Measured signals, however, show a

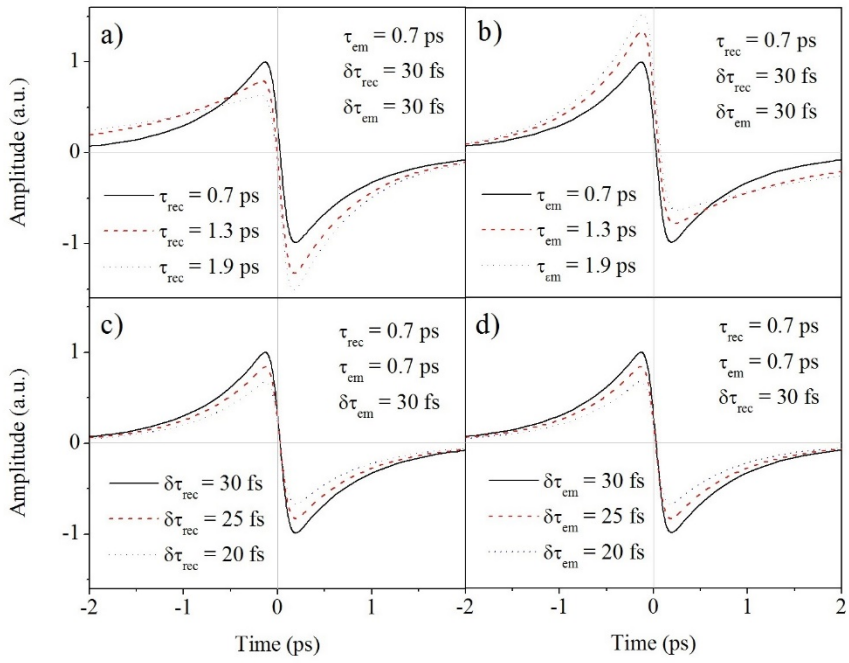

Figure 17. Computed time traces of receiver photocurrents under variation of carrier lifetimes (a, b) and momentum relaxation times (c, d) of the receiver (a, c) and the emitter (b, d)

uniform decrease in the positive as well as the negative peak (see Figure 12), as opposed to the energy redistribution between both peaks observed in Figure 17a) and Figure 17b). Furthermore, the temporal pulse widths broaden and the spectral peaks consequently shift, as it is depicted in Figure 18a) and Figure 18b). Carrier lifetime variations, which cause amplitude changes in the order of the measured ones ($\sim 35\,\%$ for the receiver, see Figure 12), result in shifts of the maximum frequency of the order of $\Delta f = f(A_{max}) - f(A'_{max}) = 100\ GHz$. Since within the resolution limit of the measurements ($\Delta f = 20\ GHz$) no noticeable spectral shift is observed (see Figure 14), the effect should not be attributed to a change of the carrier lifetime. The situation becomes different, when the momentum relaxation times are varied. For smaller $\delta\tau_{em}$ or $\delta\tau_{rec}$ the amplitude becomes smaller in both peaks (Figure 17c) and Figure 17d)), while neither the pulse shape nor the spectrum do significantly change, just as observed in the measurements. Computed spectra, however, reveal a difference in the behavior of the emitter and receiver PCA. A variation of $\delta\tau_{em}$ causes a different roll-off at higher frequencies (Figure 18d)). A variation of $\delta\tau_{rec}$, in contrast, leaves the Fourier spectrum unchanged (Figure 18c)). This becomes clear considering Equation (37): Whereas $\delta\tau_{em}$ affects the pulse shape (being argument of term$f(t, \tau_{em}, \tau_{rec}, \delta\tau_{em})$), and, in turn, affects the spectral distribution, $\delta\tau_{rec}$ plays a different role: Because it does not appear in $f(t, \tau_{em}, \tau_{rec}, \delta\tau_{em})$, but in the fractional term, there is no impact on the pulse shape, but a reciprocal scaling in amplitude, reflected in the measurements presented in Figure 15. Hence, the spectral power distribution obtained under variation of $\delta\tau_{rec}$ is maintained. The slight differences in the spectra, when the CW is injected into the

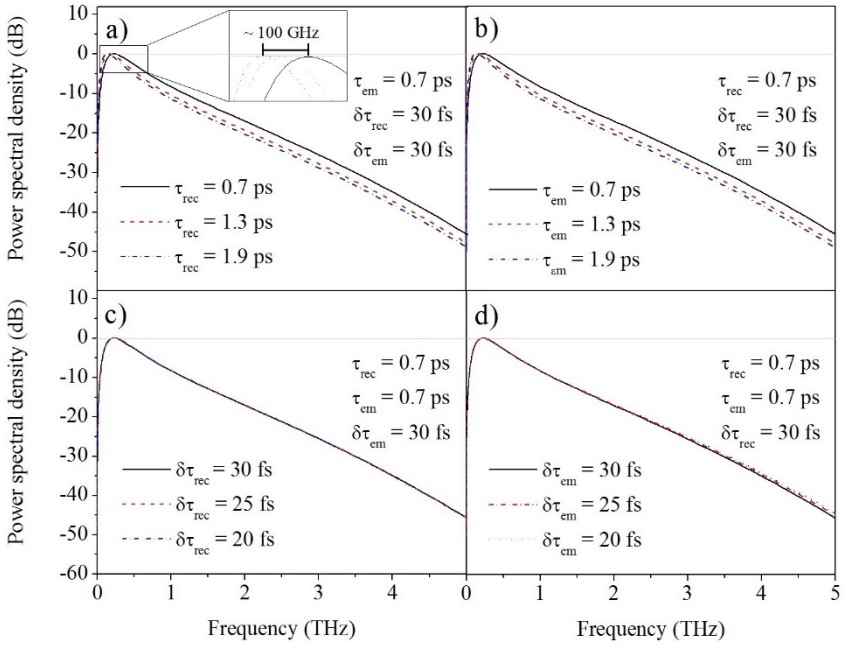

Figure 18. Computed spectra of receiver photo-currents under variation of carrier lifetimes (a, b) and momentum relaxation times (c, d) of the receiver (a, c) and the emitter (b, d)

emitter, cannot be appreciated in the experiments due to bandwidth and noise limitations in the setup.

To back up the conclusions drawn above, a photocurrent autocorrelation measurement was conducted for the emitter module. Autocorrelation traces allow the extraction of the lifetime of the conduction carriers [151]. As it can be seen in Figure 19, the irradiance of an optical CW of similar power to the pulsed power, which noticeably reduces the radiated THz field amplitude, does not recognizably alter the autocorrelation trace within the limits of the resolution of the measurement. Gaussian fits of the principal lobe show almost identical FWHMs of around $230\,fs$. The slightly smaller width of the graph

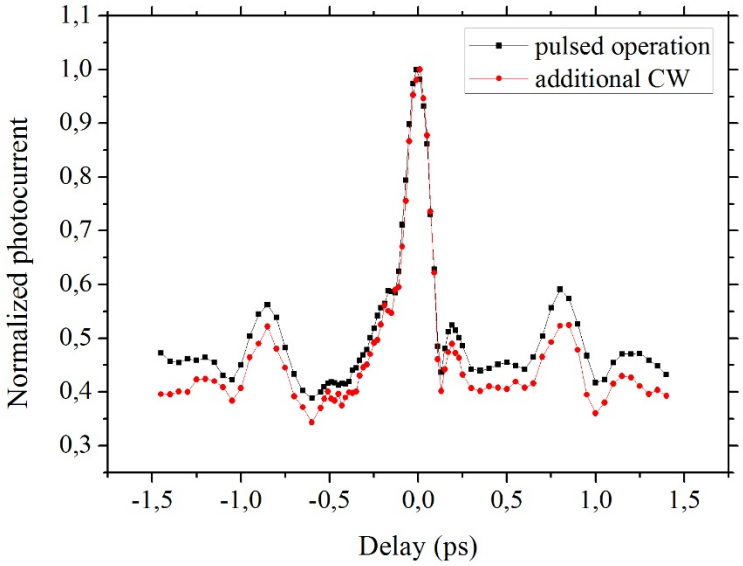

Figure 19. Photocurrent autocorrelation trace for the emitter module.

representing the additional CW cannot be taken as an indicator for a narrowing due to the measurement uncertainty. A potential increase of the carrier lifetime, however, would favor higher THz amplitudes (compare Figure 18b), what is in opposition to the observed behavior.

Concluding, the conducted experiments show that observed reductions in the amplitude of the THz signal occur due to absorption and phonon scattering rather than redistribution of carriers in the semiconductor's energy bands and states. From a technological point of view, the injection of an additional CW optical signal into both emitter and receiver antennas in a THz time-domain spectrometer diminishes the amplitude of the THz field, while the signal's spectral shape and bandwidth is maintained. Although presented results with $1550\,nm$-LTG-InGaAs/InAlAs-devices contrast those Ryu and Kong [136]

produced with $780\,nm$-LTG-GaAs-antennas, it still represents a method to manipulate or optically control the THz amplitudes without severely changing the standard operation conditions.

3.4 Application: Signal Modulation

A potential application of an all-optical signal control by a CW is amplitude modulation. Generally, in THz-TDS a modulation can be implemented through various mechanisms. One possibility is mechanically chopping the THz beam in free-space. This mechanical method is technologically poor, because it involves moving parts and it is limited to low modulation speeds. Amplitude modulation of the optical pulses by means of a chopper in free-space has the same drawbacks. External modulators in fiber-based schemes and electronic modulation of the antenna bias voltage are further modulation methods, which affect directly the THz generation process. Even free-space THz modulators are available [152, 153]. Performing modulation via a CW represents an alternative approach, which allows high frequency modulation since low-cost directly modulated CW lasers at $1550\,nm$ with bandwidths up to the GHz range are commercially available. Additionally, all-optical modulation is convenient for fiber-based remote THz sensing heads.

THz signal modulation, for example, is desired for future communication applications; however, the most natural use in the present setup, where the signal is obscured by noise, is its exploitation for lock-in detection. To assess the feasibility of optical modulation for lock-in detection an experiment sketched in Figure 20 has been set up.

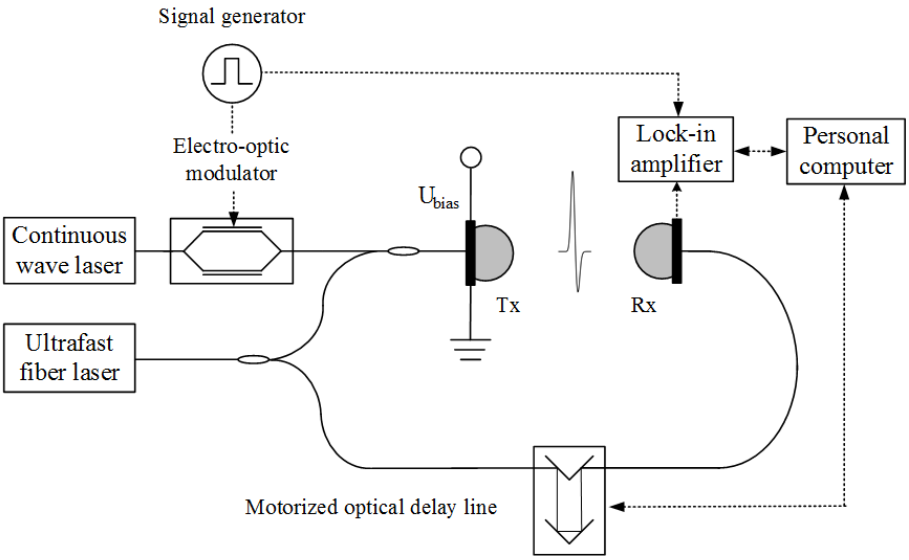

Figure 20. Setup to test CW optical modulation in THz-TDS

Here, a conventional fiber-based THz-TDS setup has been modified, inserting a fiber-coupler in the emitter branch of the fiber circuitry, enabling the CW injection into the emitter PCA (modulation of the receiver is not sensitive to the THz signal due to the large modulated dark current). Whereas the insertion requires a readjustment of dispersion compensation in the conventional fiber circuitry, the injection line does not demand such, guiding a narrowband signal. A common $1550\,nm$ CW telecom laser source has been utilized to provide the modulation signal. An electro-optic modulator, in this case a *Mach-Zehnder-modulator* (MZM), has been integrated in the fiber pathway. Instead of driving the emitter PCA with the modulation signal of the signal generator, this signal now controls the output power of the MZM.

To produce comparable results with respect to standard operation, i.e. modulation of the emitter bias, the emitter has

been biased with a fixed voltage equal to the high level of the square-wave signal of the respective bias modulation. In this manner, the carrier-accelerating field is supposed to be equal for both modulation types.

To modulate the MZM a bipolar rectangular waveform has been selected, because it had proven most efficient at bias modulation. Power levels of the pulsed and CW sources were of similar magnitude. A series of measurements, in which CW signals with power levels of $6\,mW$, $11\,mW$ and $16\,mW$ have been injected, has been conducted for increasing bias voltages. Figure 21 shows the signal amplitude curves for those measurements.

Despite the effect of amplitude reduction at CW irradiance, for increasing optical CW power, the measured signal rises, since a higher amount of energy is modulated. That means, whereas

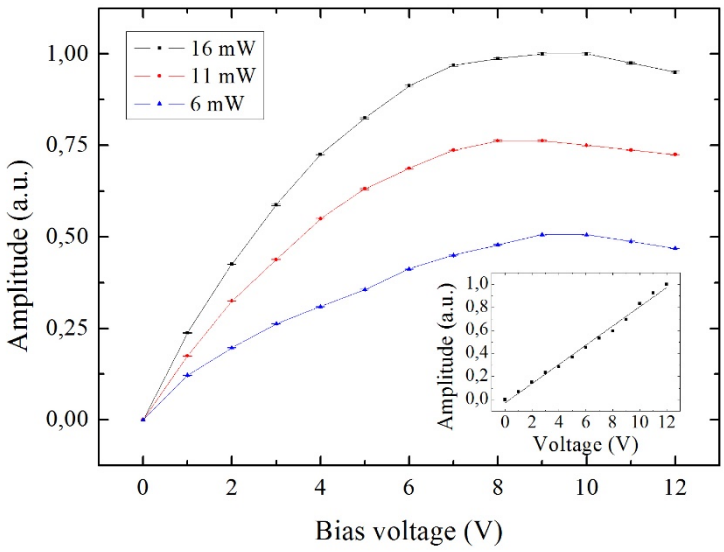

Figure 21. Relative amplitudes of THz signals vs. emitter bias voltage for CW optical modulation. Inset: Curve for emitter bias modulation.

the radiated THz power shrinks because of the CW absorption, the detectable part is increasing. It turns out that the optical modulation method leads to a saturation behavior reaching its maximum between $8 - 10\,V$, whereas modulation of the antenna bias shows a linear rise in the examined range up to $12\,V$ (inset of Figure 21). Optical modulation becomes less efficient after passing its maximum.

The modulation efficiencies have been examined, varying the modulation frequency from few Hz to $80\,kHz$. The optimum modulation frequency for both modulation techniques was found to be around $30\,kHz$, what is most likely related to the bandwidth of the detection electronics. The amplifier bandwidth as well as the electric circuitry inside the antenna modules are possible candidates to be the limiting element. Whereas the amplitude

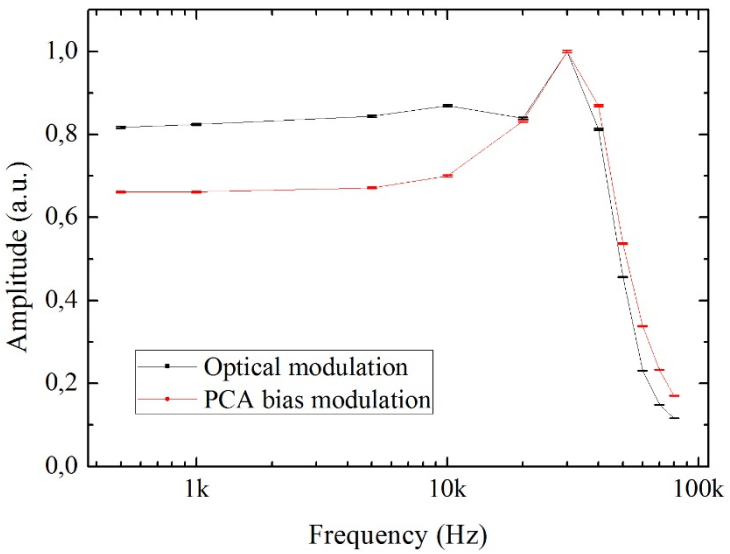

Figure 22. Modulation efficiency vs. modulation frequency for CW optical modulation and electrical bias modulation

decrease towards lower modulation frequencies is lower for the optical modulation, the detected photocurrent drops drastically for both modulation types after reaching its maximum (see Figure 22).

Since for the optical modulation of the CW only a part of the total incident optical energy is modulated, signals of equal amplitudes have been considered to compare both modulation methods. The spectra in Figure 23 reveal that there is no major degradation regarding bandwidth and DR, when optical modulation (red dotted line in Figure 23) is applied.

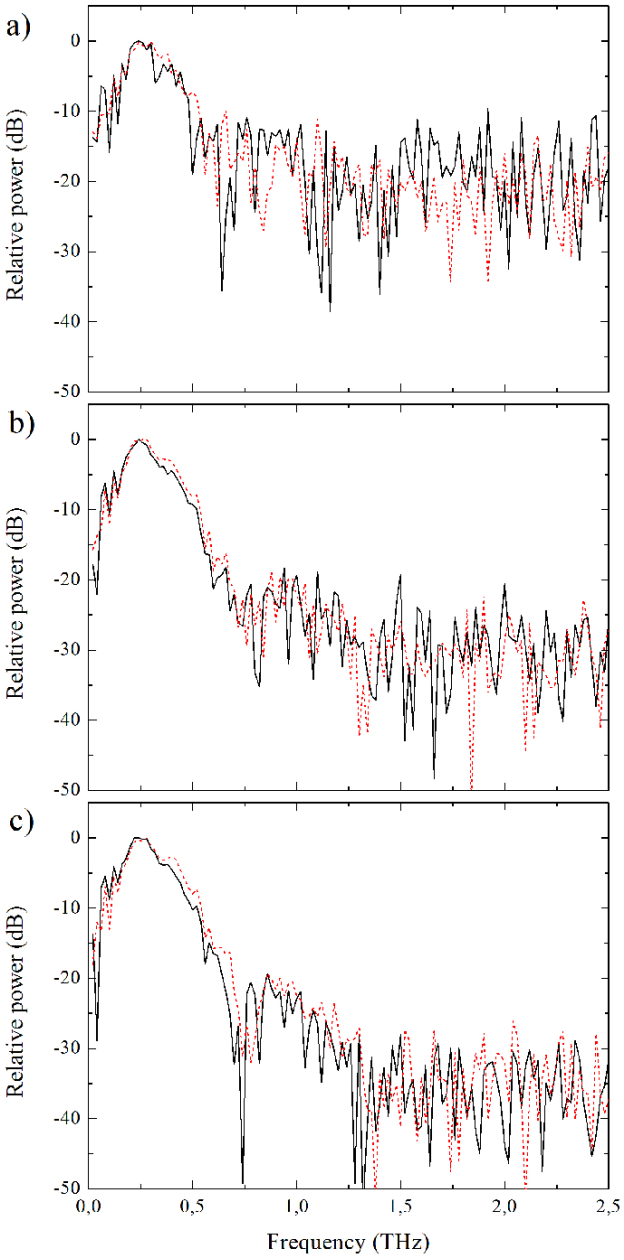

Figure 23. Fourier spectra captured using CW optical modulation (dotted line) and emitter bias modulation (solid line) for CW optical powers of $6\,mW$ (a), $11\,mW$ (b) and $16\,mW$ (c).

4. Rapid Data Acquisition

In conventional THz-TDS instruments for scientific spectroscopy studies, acquisition time might not be the most critical parameter. Instead, DR [107], bandwidth and transmitted power are usually the main targets. A common technique to enhance the DR of many instruments, also THz-TDS systems, is averaging. If the identical signal can be measured several times, the signal traces can be averaged to minimize noise. However, in many industrial applications [154, 155] acquisition time is critical. A similar situation arises in spectroscopic THz imaging [15].

In general, fast data capture has been enabled by certain progress of the photoconductor growth and antenna design (THz emission has been boosted to two to three orders above the noise background), so that state-of-the-art devices feature high output powers and high signal-to-noise ratios, what has made lock-in filtering redundant. The lapse of lock-in detection reduces system complexity and cost by diminishing the number of system components, removing those used for modulation and filtering. Nevertheless, the different contribution of noise sources has to be evaluated anew without lock-in detection, since, for example, thermal noise is no longer eliminated [156].

Latest advances aim at high-speed data capture, implementing delay implementations like presented in Section 2.3.3. They were mainly fast implementations of optical delay lines or schemes using a pair of femtosecond lasers or a modified one to allow tuning of the cavity. In this thesis, the use of a fast mechanical, fiber-coupled optical delay line will be studied.

In delay line-based THz-TDS systems, the registration error of the delay position due to timing jitter or irreproducibility of the positions can become the dominant source of error [156, 157, 158, 159]. Among these uncertainties, fixed-offset errors can be reduced by careful trace alignment before averaging in the data processing stage.

4.1 Spectrometer Setup

Optoelectronic delay schemes, reaching up to kHz scanning rates, are commercially available (see Section 2.3.3.2), but their cost is considerably higher than conventional schemes, being one of the key obstacles for widespread use of THz technology [54]. Schemes based on a fast mechanical optical delay line are very similar to conventional instruments and thus the cost increment can be kept small.

A spectrometer assembly with fast data capture (see Figure 24) was set up. It included a customized fiber-coupled high-speed mechanical optical delay line, shown in Figure 25.

The delay is introduced by a hollow-cube retro-reflective gold mirror mounted on a voice coil-driven slide. In contrast to approaches with mirrors attached to vibrating membranes, this delay line benefits from a wider scanning range, but at the cost

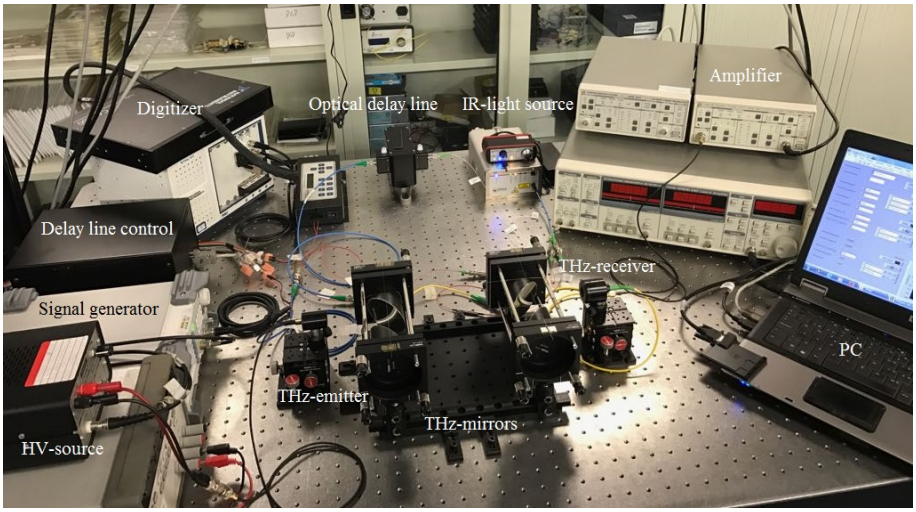

Figure 24. THz-TDS setup including a mechanical optical delay line for rapid data capture

of lower scanning rates. In the present case, the maximum scanning range was around $1\ cm$ corresponding to a maximum pulse delay of approximately $67\ ps$. The mechanical inertia of the carrier slide constrains the scanning rates to $f_{scan} < 20\ Hz$, resulting in $N = 2 \cdot f_{scan} \leq 40$ traces per second. Similar to state-of-the-art commercial devices [88], this corresponds to an average delay-scanning rate of around $1200\ ps/s$, when a linear motion with short interruptions at the reverse points is considered. A low-noise current amplifier amplified and converted the photocurrent signal to the $mV - V$ scale. Data capture was realized using a high-speed digitizer able to sample at rates ranging up to $15\ MSa/s$.

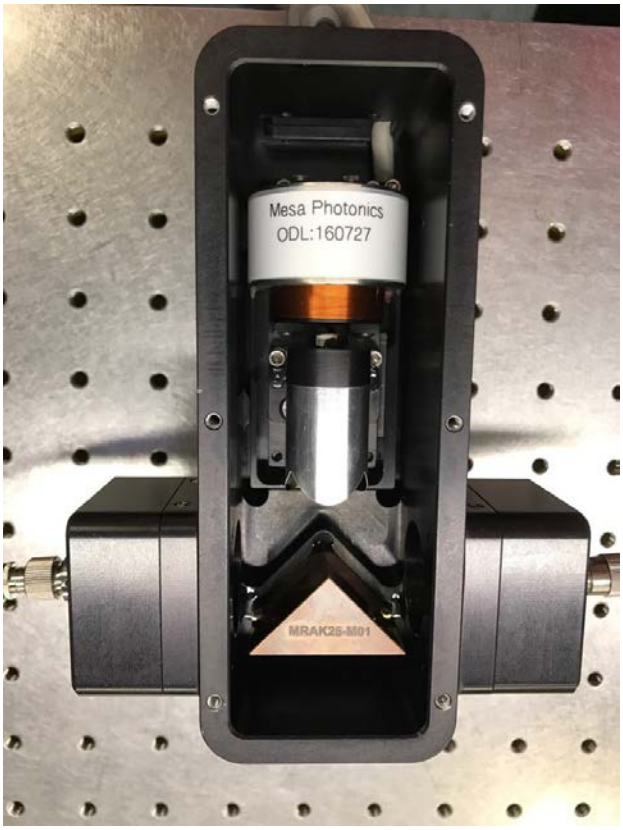

Figure 25. High-speed mechanical delay line: Optical delay via a reflecting prism and hollow-cube reflector mounted on a voice coil

Implementing the fast delay line introduces several novelties: First, since in many THz-TDS systems the $1/f$-amplitude noise of the optical source is the dominant noise source [113], in such a system low frequency variations will not be picked up in a fast measurement. Reducing the measurement time due to long-term instabilities has already been considered, for instance, at the development of DTDS [110]. Second, it enables averaging of a significantly higher number of signal traces. Third, oversampling can be performed with even moderate sampling rates, so that a

bunch of traces with a resolution well above the Nyquist rate can be taken simultaneously.

4.2 Performance

In general, there are several uncertainties influencing THz-TDS measurements, comprising sample geometry, misalignment, refractive index fluctuations, reflections, blackbody radiation, laser instability as well as thermal, shot and quantum noise. While the former have been discussed exhaustively in different work [111, 112, 113, 114, 115, 117, 160, 161, 162], here, only the signal noise shall be considered. Noise sources in THz-TDS have been investigated for long [113, 163], however, in in different system different noise sources might be predominant.

In a THz system with a fast optical delay line for rapid data acquisition, the registration error of the delay line position through timing jitter or irreproducibility of the positions can become the dominant source of error [156, 157, 158, 159]. This registration noise can be reduced by careful trace alignment and averaging in the data processing stage.

Spectroscopic performance, i. e. bandwidth and resolution are limited by the DR [107] and SNR [164], respectively. It is therefore important to know, which is the limiting uncertainty or error in the system.

We have investigated, if the inherent electronic noise of the PCAs (and current amplifier) is the limiting factor or if obtained noise level could be further reduced, by delay line control or data processing.

The data acquisition process involves as potential error sources the clock jitter of the digitizer and the quantization error. The clock jitter of the digitizer used in the setup shown in Figure 24 (National Instruments PXI-5922) is $< 3\,ps$ and translates for delay line speeds in the order of m/s to delay errors in the sub-attosecond range, being thus negligible. The quantization error, reflected in the *signal-to-quantization noise ratio* (SQNR) in the time domain, is [165]

$$SQNR = 1.761 + 6.02 \cdot N, \tag{39}$$

where N is the number of bits of the data. For the maximum applied sampling rate of $0.5\,MSa/s$ storing data with $24\,bits$ resolution, the SQNR is with $\cong 146\,dB$ still far greater than the span between the maximum amplitude and the observed time-domain noise floor of $\sim -53\,dB$ in a single measurement. However, the jitter in the time or delay axis, which is caused by the electronic noise of the optical encoder, might become decisive. This error is specified by the manufacturer as $\delta x \leq 150\,nm$, what results in delay jitter of $\delta t \leq 1\,fs$, but is frequency-dependent. Therefore, and since any digitizing errors are assumed to be smaller, statistical analysis has been applied to compute the *standard deviation* (SD) of the sample positions as averaged delay jitter. The computed SD surprisingly depends on the sampling rate. Values obtained for 500, 50 and $5\,kSa/s$ were $0.8, 1.4$ and $1.5\,fs$. The maximum obtainable dynamic range (in the time domain) is described by [166]:

$$DR_{max} = -20 \cdot \log(2\pi f \cdot \delta t) \tag{40}$$

The DR_{max} of femtosecond jitter on the THz-frequency scale is very sensitive to δt. Plots for the computed SDs are illustrated in

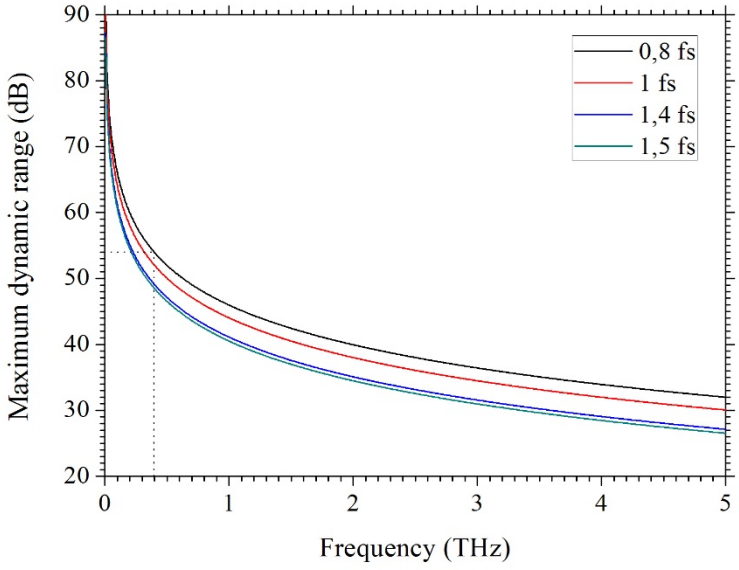

Figure 26. Maximum obtainable dynamic range due to timing jitter

Figure 26. In the typical frequency range of a THz-TDS instrument, calculations show that, for the fast ODL and ADC considered here, jitter noise can be the limiting noise in PCAs: According to Equation (40) and indicated in Figure 26, the DR_{max} at $400\,GHz$, the peak frequency, is $53.9\,dB$, what reflects the experimentally found time domain DR ($53\,dB$), when sampled with $500\,kSa/s$ ($\delta t = 0.8\,fs$).

Concluding, in the presented system, the jitter noise of the delay line is likely to determine the DR_{max} of the overall system. Enhanced accuracy of the time axis is supposed to improve the measurement quality. Surprisingly, in this case, the statistically calculated SD decreased with measurement speed and hence provides better and faster data capture. However, data post-processing can enhance jitter-limited results.

4.3 Data Processing

A mechanical delay at high scanning rates encounters several challenges at the processing stage. Firstly, a linear motion can only be well approximated in a relatively slow scanning mode. In the present setup, the slide could be driven until about $5\,Hz$ without severe distortions of the linearity. If the pulse occurrence is located well apart from the reverse points, the nonlinearities emerging at higher rates might have little effect on the pulse shape.

4.3.1 Linearization

Mechanical delay lines can be run at faster scanning rates by applying nonlinear driving waveforms for the motion of the slide. For example, a sinusoidal control signal showed a rather pure sinusoidal response until about $15\,Hz$. Above this value, the measured position signal exhibited considerable deviation from the sinusoid and particularly asymmetry between scanning directions. Nonlinear motion, however, leads to a set of non-uniformly sampled data. Hence, spectral information has to be extracted either evaluating those unevenly spaced data by estimation methods or generating linearized data by interpolation. The former can be realized by several distinct methods, such as the Lomb-Scargle periodogram [167, 168], but algorithms are computationally effortful and the reconstruction is not perfect, but rather estimation-type, whose quality strongly depends on the type of data nonlinearity or uncertainty.

The Fourier transform, in contrast, returns complete spectral data for a bandlimited signal sampled above the Nyquist-rate. Nevertheless, once more, the noise data are compromised, because interpolated data points reconstruct the signal, but do not carry information of unpredictable noise amplitudes within the sampling intervals. Interpolation of a noisy signal underestimates the noise, since interpolated data points lie intermediate on the ordinate. This underestimation is more severe, the closer the sampling rate and the frequency to detect lie.

To assess degradations caused by interpolation, the following simulations have been conducted. A trace with N data points of a hypothetical harmonic signal of frequency f_{hyp} has been uniformly sampled at a frequency f_{sample} above the Nyquist-rate. Subsequent Fourier transforming results in perfect reconstruction of the frequency and the amplitude of the signal. Alternatively, N non-uniform samples – a cosine like distribution of query points as produced by the velocity profile of delay line has been assumed – have been taken for comparison. These samples were interpolated to extract uniformly spaced data. Although lying equidistant, they are no true samples of the signal. Hence, a Fourier analysis will not return the correct amplitude of the real signal. The amplitude of the reconstructed tone in the spectrum was compared to the one gained with the true uniform samples for several values of the ratio $f_{sample}/\, f_{hyp}$. In a bandlimited THz signal, f_{hyp} is considered the maximum frequency component f_{max}. The outcome of the simulation, presented in Figure 27, shows that if $f_{sample} > 10^2 \cdot f_{max}$, the reconstructed signal amplitude is about $99.9\,\%$ of the real amplitude obtained with uniform sampling. Measurements with smaller ratios, i.e. with slower sampling or emergence of high frequency components,

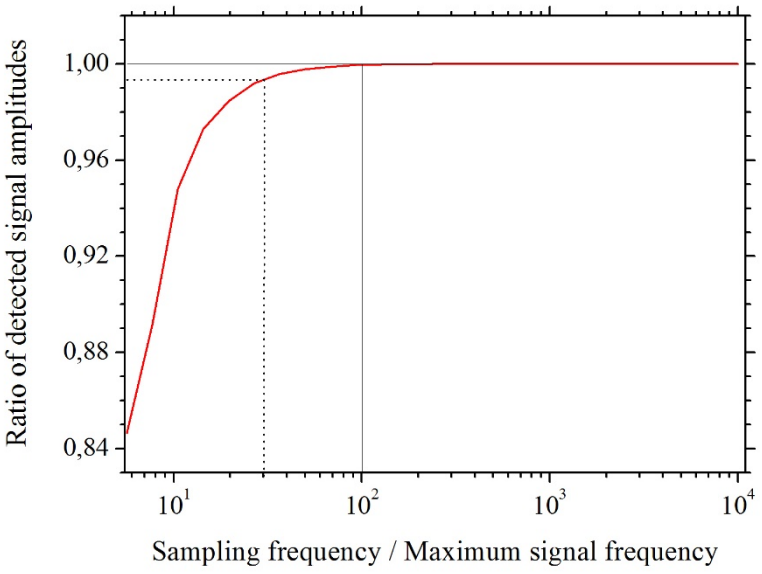

Figure 27. Simulation of the quality of signal reconstruction of interpolated data with varying ratio of sampling and maximum signal frequency. The solid line marks the frequency ratio of 100, which allows signal reconstruction better than 99.9 % and the dotted line marks the ratio of 30 for the estimation below, which still results in a reconstruction of more than 99 %.

suffer from a considerable degradation caused by the interpolation.

The present system was driven at $10\,Hz$ with a displacement range of about $1\,cm$. A conservative estimation, considering a sinusoidal drive signal, yields as a typical maximum displacement velocity of the mirror $0.5\,m/s$. When sampling with $0{,}5\,MSa/s$, a sample is taken every $2\,\mu s$. During such a sampling period, the displacement of the mirror is $1\,\mu m$. Due to the double pass of the optical signal, the generated delay between two consecutive samples is $6.6\,fs$. This corresponds to a sampling rate of $150\,THz$, what is exactly a factor 30 greater than the considered bandwidth

of $5\,THz$, with the maximum signal frequency being even smaller. Concluding, a sampling rate of $0.5\,MSa/s$ is sufficient to reconstruct the signal with more than $99\,\%$ of accuracy. It is important to note that interpolation removes high frequency contents – in these measurements only noise – but at no point improves the SNR or DR, because signal and noise are affected the same way. Taking the flat part of the spectrum in the $5\,THz$-window as noise floor of the measurement, one can calculate the PDR within mentioned accuracy range.

4.3.2 Temporal Alignment

Sample positions in fast optical delay lines do not repeat exactly at each scan and thus averaging over equally indexed data

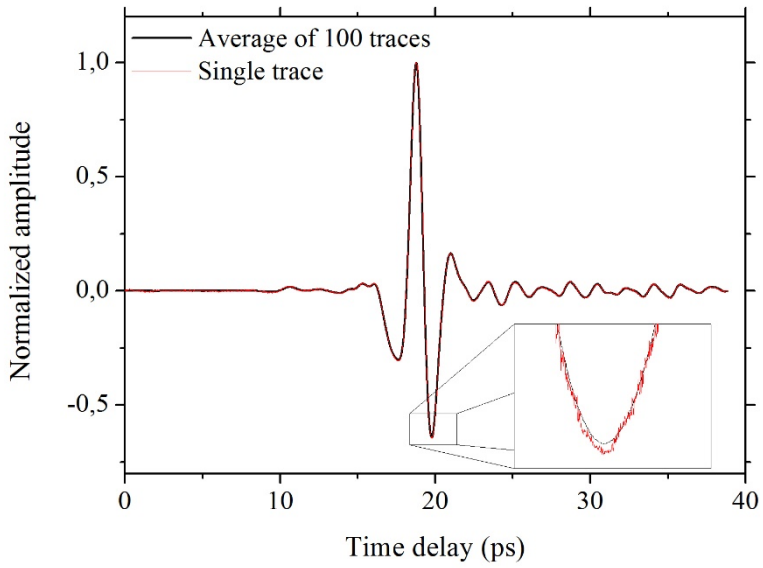

Figure 28. Temporal traces a single trace and the average of 100 time traces

points would result in a jitter-like error. The arbitrary position shift of data points in each measurement can be corrected by interpolation, whereas a constant offset-error appearing in the data is not removed that way.

Consequently, temporal offsets between different traces have to be treated by alignment procedures. Poor alignment, i.e. delay axis uncertainties can be more detrimental to the outcome of the measurement than amplitude noise itself [159, 169]. The difficulty of proper alignment lies within the fact that, due to noise, signal features like extrema or zero crossings are obscured. There can be found plenty of alignment procedures in literature [170, 171, 172, 173, 174], which even provide sub-sampling interval temporal resolution. Due to the sampling capacity of the employed digitizer, a straightforward sliding average method similar as in

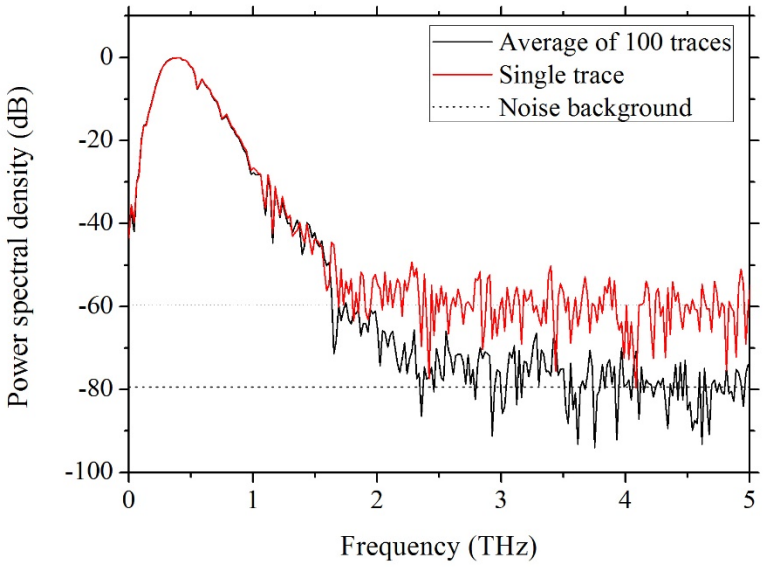

Figure 29. Spectra of a single temporal trace and averaging of 100 time traces

[170] has been used for alignment. Figure 28 shows the temporal traces and Figure 29 the spectral data for a single scan and the 100-traces average. Averaging causes the noise floor to drop from $-60\,dB$ for a single measurement to $-80\,dB$ for the average of 100 measurements. The PDR hence is raised by $20\,dB$. This agrees with the theoretical improvement obtainable by averaging, given by

$$PDR_{dB}(N) = 20 \cdot \log(\sqrt{N}). \tag{41}$$

The PDR data extracted from the measurements (see Figure 30) exhibit with $(9.95 \pm 0.17)\,dB/dec$ almost the theoretical limit of $10\,dB/dec$. It is noteworthy, that in contrast to Section 4.2, here the DR data are derived from the spectra and not from the

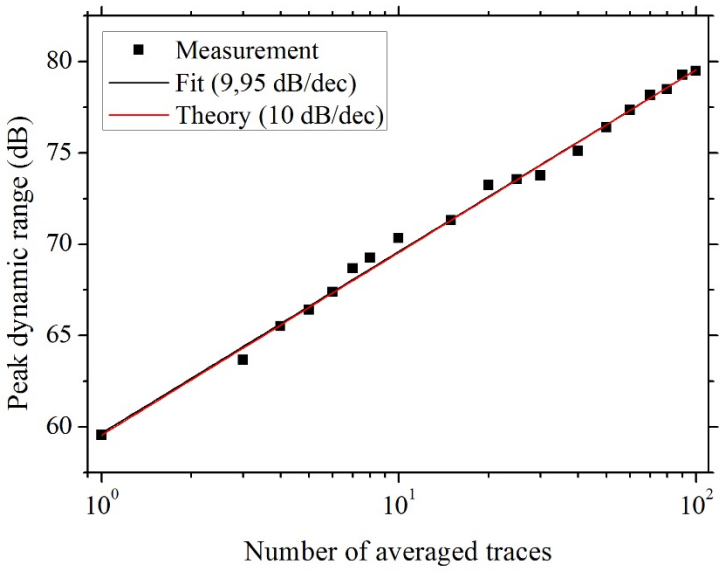

Figure 30. Peak dynamic range vs numbers of averaged data traces

time domain. Proper alignment turned out to be indispensable to achieve this value. Obtained performance is comparable to state-of-the-art commercial devices [88, 103], when neglecting the measurement speed, which is ECOPS-based in [103]. The temporal data corresponding to Figure 29 with a trace length of approximately $40\ ps$ have been captured in $100\ ms/trace$. Hence, to achieve the $80\ dB$ PDR, $10\ s$ measurement time were necessary, opposed to $82\ dB/4.4\ s$ (mechanical delay [88]) and $76\ dB/0.5\ s$ (ECOPS [103]).

5. Parallel Terahertz Sensing

Sensing instruments exploiting the THz band offer an attractive approach to non-destructive inspection of a wide range of materials with applications in an increasingly extensive variety of industries: in-line monitoring of plastics, compounds, glass, paper, etc.; analytical sciences; biological, pharmaceutical and medical sciences; quality control; environmental monitoring; security, etc. [14, 175]. In many cases, these instruments sense features that are not accessible with sensors working in other spectral regions such as the optical, infrared or X-ray bands or complement the information obtained by these. Since THz radiation is located between the microwave and the optical regions of the electromagnetic spectrum, they exhibit merits of both bands: good penetration depth as well as sub-millimeter resolution. When exposed to terahertz radiation, neither scanned objects nor operators run considerable damage or health risk as opposed to X-ray-based inspection systems. Additionally, many materials that are opaque in the visible and near-infrared regime (such as plastics, paper, cardboard, textiles, etc.) are transparent in the THz region, while many other materials present characteristic spectroscopic fingerprints in this band. Thus, the

THz band allows the inspection of materials inside conventional packages.

Pulsed THz PCAs based on $1550\,nm$ sources allow the implementation of all-fiber THz-TDS systems [80, 129, 130, 176, 177, 178, 179] rivaling the traditional free-space THz systems. Usually all-fiber THz-TDS systems use very short fiber lengths. However, the excellent features of optical fiber as transmission medium can be further exploited to simplify large THz systems by establishing a centralized common signal source with several sensor heads. Hence, the use of optical fiber enables long-haul signal distribution and remote operation control of THz systems. All-fiber implementations are less susceptible to optical misalignment, are less cumbersome and, most notably, show lower cost maintaining good performance. The former takes effect when it comes to precisely coupling the light into the PCAs or if mechanical perturbations (e.g. vibrations in industrial environments) occur. Furthermore, ambient parameters like humidity, dust/vapor concentration, etc. do not affect propagation in fibers, whereas they could cause degradation of an optical beam.

Sets of parallel inspection units based on THz-TDS might be controlled via a centralized architecture. A centralized approach with its emphasis on sharing the optical source simplifies the implementation and cost of such inspection platforms, where several sensing units consisting of remote emitter/receiver heads [178, 179] have to work in the same facility, such as in-line quality monitoring sites in factories, security controls with many parallel security checkpoints as in airports, customs or large characterization laboratories, etc. This parallel approach allows

additional cost reduction by sharing the optical source and increases the system flexibility.

This chapter discusses this sensing architecture including feasibility, key features relevant to the system performance and cost reduction.

5.1 Architecture

Optical fiber allows the remote feeding of a set of THz emitters/receivers thanks to its low transmission loss. Thus, the whole system complexity can be reduced by using a centralized architecture, which incorporates simplified modules that ease the measurement setup in industrial scenarios. Centralization also allows simplification of the control system. The small size and weight, flexibility and robustness of optical fiber facilitates the deployment of the THz sensing equipment in industries as well as the adaptation of the sensing heads to already deployed machinery. Finally, the immunity to electromagnetic interference of optical fibers simplifies deployment in harsh noisy industrial environments.

Figure 31 shows the proposed architecture for the distribution of femtosecond pulses from a single source to several THz generation and detection systems. The pulses emitted by a single femtosecond optical source at $1550\,nm$ are stretched employing a dispersive module to compensate chromatic dispersion. One of the advantages of employing photoconductive antennas fed in the $1550\,nm$ band is that dispersion compensation becomes simpler. Low order dispersion terms can be compensated employing

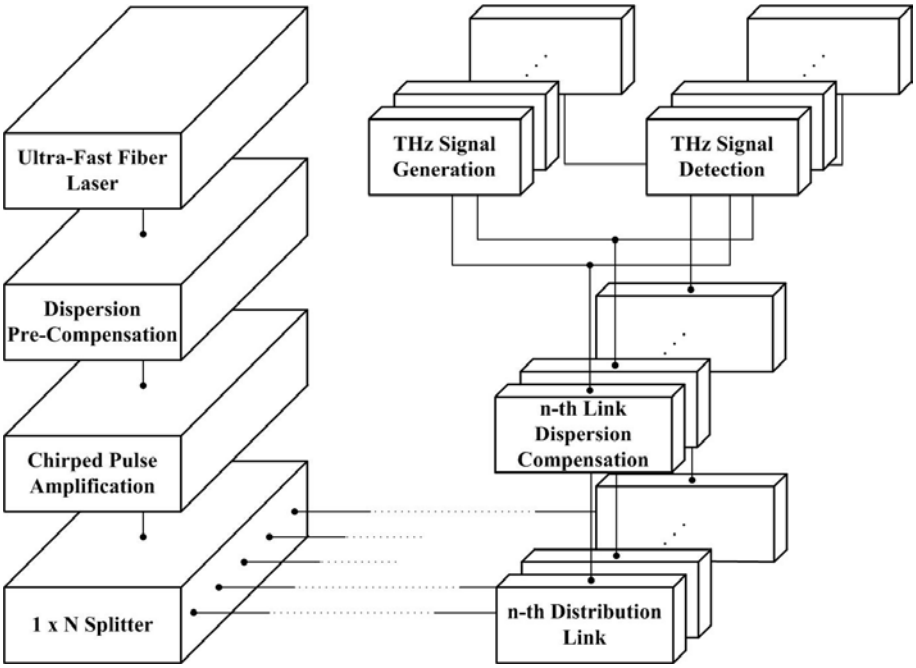

Figure 31. Centralized fiber distribution architecture

dispersion compensation-fibers or chirped fiber Bragg gratings developed for the telecom industry.

The stretched pulses are amplified by an *erbium-doped fiber amplifier* (EDFA) to compensate the distribution loss in the optical splitter. A stretched pulse has significantly lower peak power and thus nonlinear effects occurring in the EDFA become less harmful. In particular, *self-phase modulation* (SPM) has been proved to become decisive for the pulse quality, when high optical powers are employed [176]. The amplified optical pulse is then distributed by means of an optical splitter and standard single-mode fiber links to different THz heads. Each distribution link is made up of a certain amount of SMF, so that in case of different link lengths an individual dispersion compensation for the respective link would have to be implemented.

The femtosecond optical source is a considerable percentage of the spectrometer cost. Therefore, source sharing between several THz heads can result in a considerable cost reduction. Figure 32 shows an estimation of the cost reduction for a typical all-fiber setup. As it can be seen, a centralized THz-TDS system might reduce the system cost to between 50 % and 70 % of the cost of a set of conventional THz-TDS systems for a number of parallel sensing heads approximately greater than five or higher. The relative cost reduction asymptotically approaches a certain limit within this percentage range, which is given by the cost of the components used to build up the spectrometer. The depicted curves were calculated assuming high and low price limits of conventional commercial telecom laser sources. In a centralized architecture, additional sources can be saved, whereas the

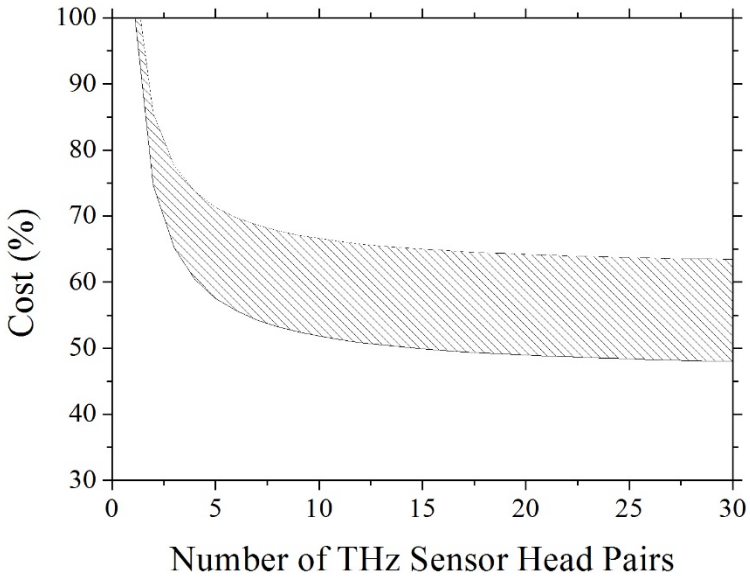

Figure 32. Range of potential cost reduction due to optical source sharing in THz-TDS.

remaining components' cost increases linearly with the number of inspections units. Further saving potential lies in sharing a common delay stage, as it is sketched in Figure 33, which introduces delays before the signal is split. When residual dispersion issues are eliminated, future implementations might rely on a centralized delay control, integrating the delay stage in the central part of the system.

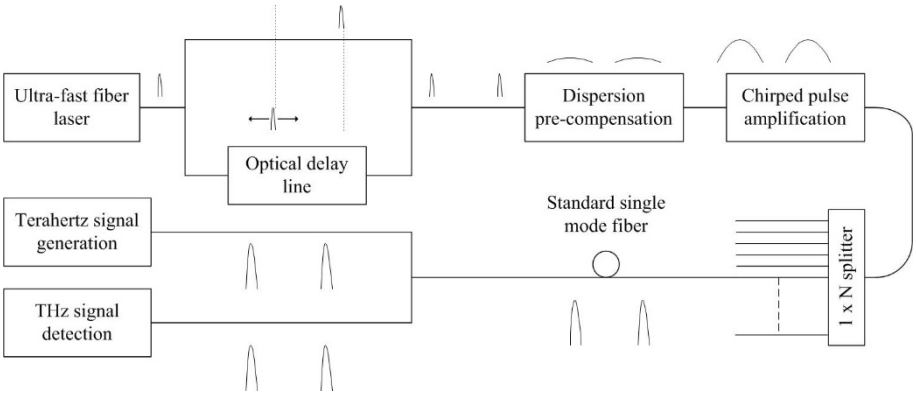

Figure 33. Integration of a delay line in the central part of the parallel sensing architecture

5.2 Experimental Results

To evaluate the feasibility of an all-fiber centralized architecture, the set-up depicted in Figure 34 has been assembled in the laboratory. The system was designed such that the section, which implements the fiber distribution link, could easily be in- and excluded, to assess how it affects the quality of the terahertz generation and detection process.

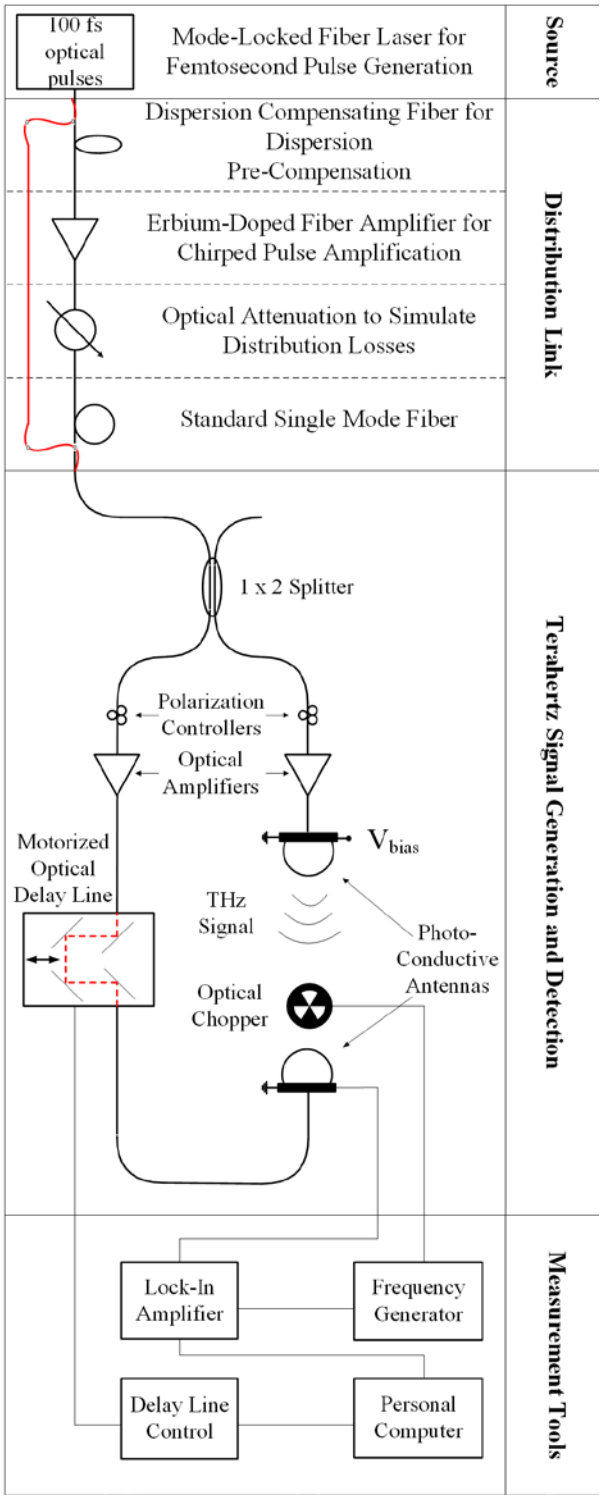

Figure 34. Set-up of the all-fiber distribution link architecture. The section 'Distribution Link' could be excluded for comparison.

Femtosecond optical pulses of approximately $100fs$ pulse width with a mean power of $2.5\,mW$ and a repetition rate of $50\,MHz$ were stretched by means of a DCF reel with a total dispersion of $-0.33\,ps/nm$. Stretched pulses subsequently were amplified via *chirped pulse amplification* (CPA) by an EDFA. Then these amplified pulses are intended to be split for fiber distribution by an $1 \times N$-fiber splitter. However, to facilitate the experimental setup, this splitter was replaced by an *optical attenuator* (OA) simulating the splitting loss. An optical loss of $12\,dB$, corresponding to a 1×16-splitter, was included in the link. The attenuator was followed by a standard SMF fiber link of $100\,m$. The delivered pulses were split into two branches and directed to the emitter and the receiver PCA, respectively. Due to the initial dispersion pre-compensation, stretched pulses ($> 10\,ps$) are measured at the input of each branch. Consequently, the length of the fibers in both branches must be tailored precisely to re-compress the pulses to the possibly narrowest shape. The pulses were passed through *polarization controllers* (PCs) and two high-output power optical amplifiers (EDFAs) before being injected into InGaAs/InAlAs PCAs. The emitter PCA electrodes were biased with $18\,V$. An LIA and an OC, modulating the amplitude of the THz signal at $1\,kHz$, was employed for detection.

Autocorrelation traces of the optical pulses taken at the input of the antennas are shown in Figure 35. It can be appreciated how the optical pulses at the input of the PCAs have been stretched by the distribution link due to residual dispersion (a, b) compared to those obtained when the fiber distribution section

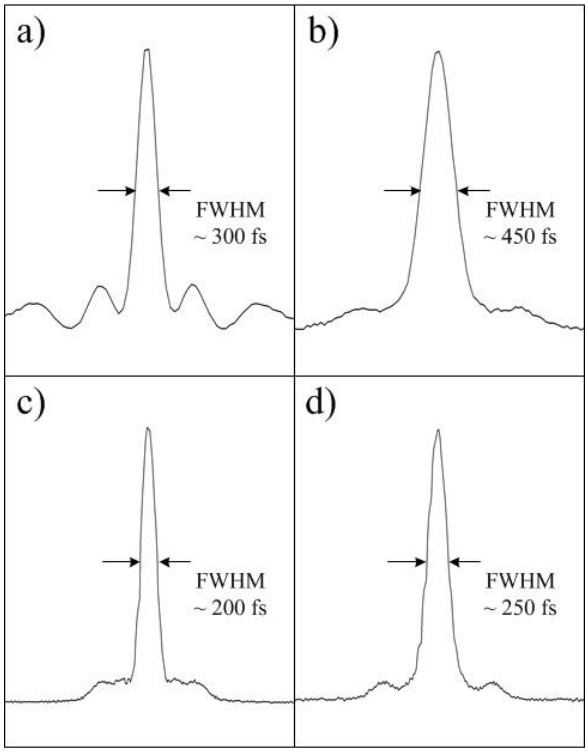

Figure 35. Autocorrelation traces of the optical pulses at the emitter (a, c) and receiver (b, d) PCA's input with (a, b) and without (c, d) distribution link.

was omitted (c, d). The pulse width or its FWHM is a decisive parameter in THz generation and detection in PCAs [60].

Figure 36 shows the detected terahertz signal and Figure 37 its spectrum, where the $10\,dB$ bandwidth of the Fourier spectrum falls close to $1\,THz$ and signal frequencies up to $2\,THz$ are observed. For comparison, the curves for the system without the distribution link are included. It becomes clear that the system suffers a degradation of the dynamic range due to additional noise introduced by the optical amplifier and a degradation of bandwidth due to the dispersion-broadened optical pulses. Both

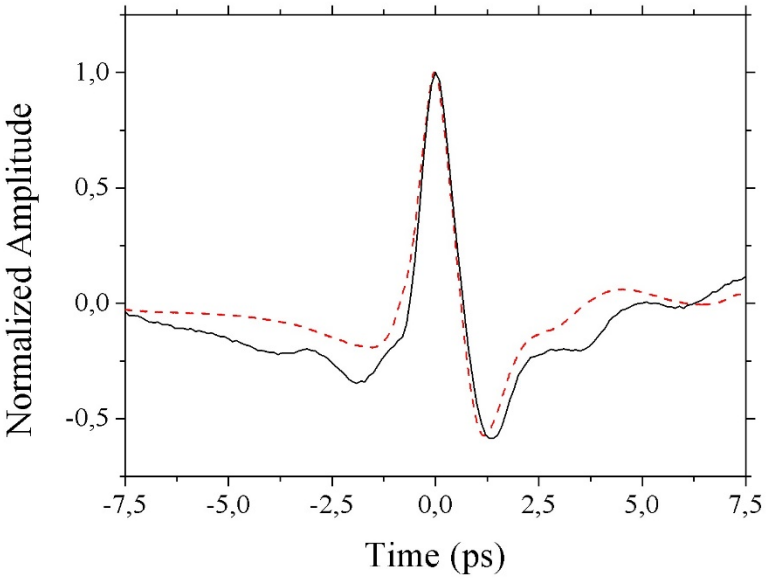

Figure 36. Time–resolved THz pulses without distribution (red, dashed line) and with $100\,m$-distribution link (black, solid line)

topics are treated in Section 5.3. Although the performance has decreased, THz frequencies up to $1.5\,THz$ have been obtained for a $100\,m$ SMF distribution link.

The feasibility of long-haul fiber distribution links feeding THz sensing units has also been tested employing an SMF link of $25\,km$ of length with the corresponding compensation module, using a similar set-up to the one shown in Figure 34**.** Once more, the positive and negative dispersion in both fiber types has to be compensated precisely to retain narrow pulses. This cancellation becomes gradually more sensitive with increasing fiber length since residual dispersion given by mismatches in higher-order dispersion parameters directly depends on fiber length. Additionally, with longer fiber links, time jitter becomes an issue and actions have to be taken to compensate it. Section 5.3.4

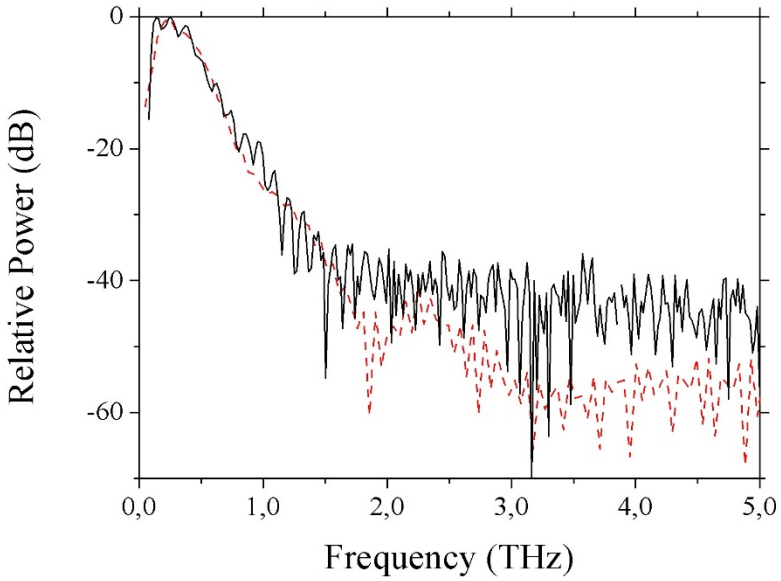

Figure 37. THz frequency spectra with 100 m distribution link (solid lines) and without distribution (dashed lines).

provides a detailed treatment of these issues. Figure 38 shows the THz spectra obtained with and without the long-haul fiber link. This result shows the feasibility of the approach when limiting factors are addressed.

5.3 Fiber Implementation Features

Although fiber-based THz systems using PCAs allow the development of complex centralized architectures not feasible with free-space optics, optical fiber implementations show several critical features that might affect or limit the performance of centralized THz inspection instruments. In this section, the

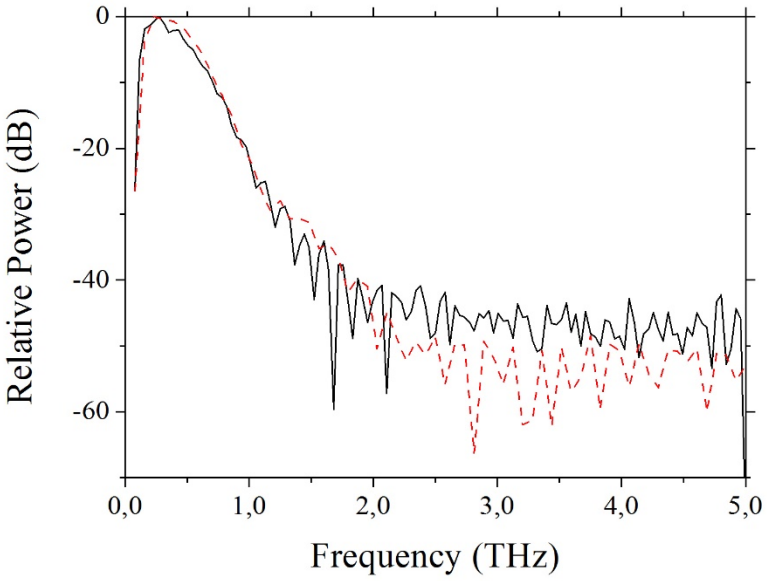

Figure 38. Spectra of THz pulses with 25 km distribution link (solid line) and without distribution link (dashed line).

impact of fiber transmission properties on the performance of THz sensing are particularly studied.

5.3.1 Chromatic Dispersion

Unlike free-space, optical fiber is a dispersive medium. Thus, light propagation in fiber results in severe stretching of femtosecond pulses after considerably short fiber lengths. The broadening factor of an unchirped Gaussian pulse of *root mean square* (RMS) width σ_0 due to chromatic dispersion is given by Equation (42) [180].

$$\frac{\sigma(z)}{\sigma_0} = \sqrt{1 + \left(\frac{\beta_2 z}{2\sigma_0^2}\right)^2 + 0.5\left(\frac{\beta_3 z}{4\sigma_0^3}\right)^2}, \tag{42}$$

where β_2 and β_3 are the fiber's second and third order dispersion parameters, respectively, and z is the fiber length.

Chromatic dispersion has to be accurately compensated to deliver almost transform-limited pulses to the PCAs for optimum THz generation and detection. The width of the optical pulses controls the bandwidth of the THz signals, as shown in Equation (43) [60]:

$$\overline{J_{rec}}(\sigma) \propto e^{-2(\pi f \sigma)^2}, \tag{43}$$

where $\overline{J_{rec}}(f)$ is the spectrum of the measured photocurrent and f is the frequency.

As mentioned in Section 5.1, different approaches are commercially available to compensate second and even third order dispersion terms. Probably the most common method is the use of dispersion compensation fibers. Figure 39 shows an example of the degradation of the THz spectrum due to residual dispersion, expressed as a length of uncompensated SMF. In particular, the example shown in the figure assumes a fiber path of $100\,m$ of SMF (dispersion $D = 20.8\,ps/(nm \cdot km)$ and a dispersion slope $S = 0.061\,ps/(nm^2 \cdot km)$) and the length indicated, compensated by a section of $40.895\,m$ of DCF ($D = -50.8\,ps/(nm \cdot km), S = -0.154\,ps/(nm^2 \cdot km)$). Due to the broadband nature of femtosecond pulses, care has to be taken to

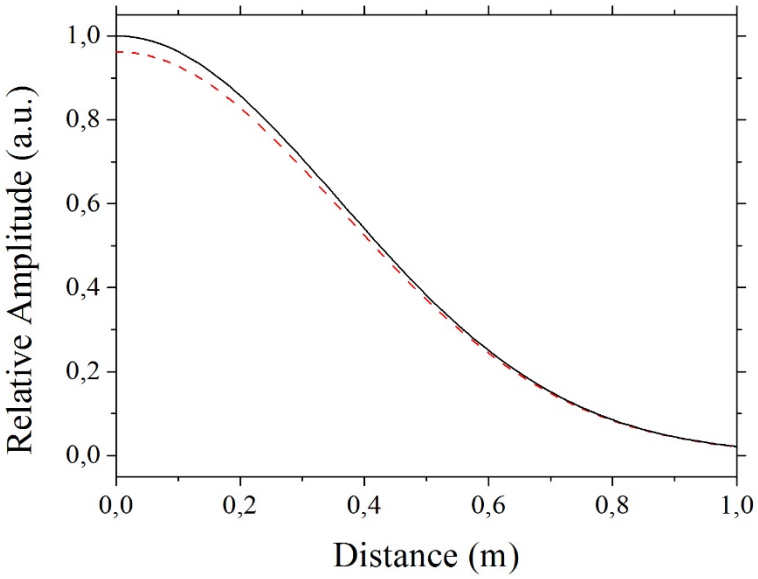

Figure 39. Effect of residual chromatic dispersion on the amplitude at $1\,THz$ of the detected photocurrent. Solid: Effect of second order dispersion. Dashed: Combined effect of second and third order dispersion.

use DCF modules, which compensate, at least partially, the third order dispersion term.

Given the tight constraints of femtosecond pulse distribution by optical fiber, dispersion changes due to temperature variations [60] might affect the THz signal in industrial scenarios. The thermal coefficient of the chromatic dispersion may have opposite signs for fibers with different dispersion sign, so it is possible to compensate partially temperature-induced dispersion drifts by combining different fibers with suitable thermal coefficients. Besides, fibers with low dispersion slopes are more convenient, not only in terms of dispersion slope compensation, but also to achieve better thermal stability. Figure 40 shows the effect of the dispersion temperature dependence on the THz signal bandwidth

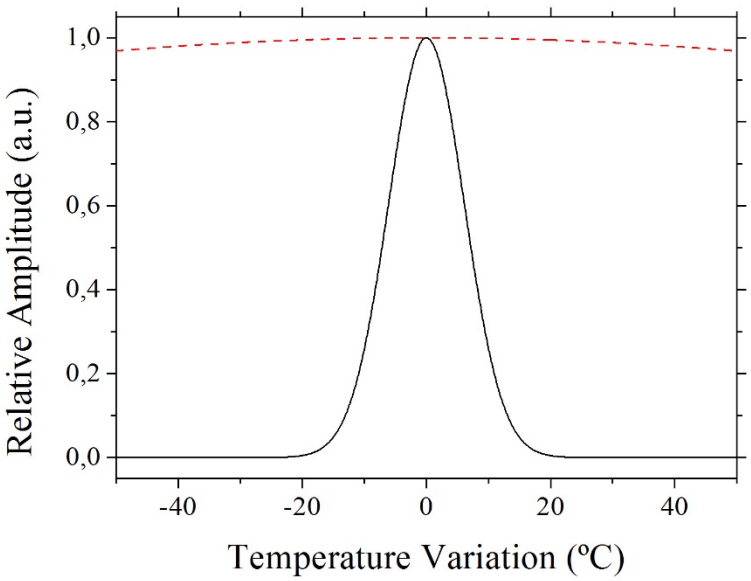

Figure 40. Effect of the temperature dependence of chromatic dispersion on the relative amplitude at $1\,THz$ of the detected photocurrent. Solid line: SMF: $-0.0016\,ps/(nm\cdot km\cdot °C)$; DCF: $0.004\,ps\,/(nm\cdot km\cdot °C)$; Dashed line: SMF: $-0.0016\,ps/(nm\cdot km\cdot °C)$; DCF: $0.0009\,ps/(nm\cdot km\cdot °C)$.

assuming $D_{SMF} = 20.8\,ps/(nm\cdot km)$,$D_{DCF} = -50.8\,ps/(nm\cdot km)$, no third order dispersion and for two combinations of dispersion thermal coefficients [181]. As can be seen from Figure 40, temperature dependence might have a considerable impact on the THz system if the compensating fiber is not suitably chosen.

5.3.2 Nonlinear Effects

Nonlinear effects in optical fiber can result in severe distortion of the femtosecond pulses when high optical power is used [176]. As an example, in [181] SPM was used in combination with *third-*

order dispersion (TOD), for THz pulse shaping. These distortions are in general detrimental to the generation and detection of THz signals in PCAs and mainly result in severe broadening of the gate pulses, which leads to the lowering of bandwidth. However, distortion by nonlinear effects can be considerably reduced by using suitable optical fibers and keeping low peak amplitudes through pulse stretching and *chirped pulse amplification* (CPA).

5.3.3 Fiber Joint Impairments

The different fiber pigtails of the components of the centralized THz sensing architecture have to be joined. This can mainly be done using fiber connectors, fusion splices, or semi-permanent splices. Fusion splices offer low attenuation and return loss but at the cost of reducing reconfiguration capability. They might be the best option for inspection platforms in an industrial scenario, since usually once the system is deployed, it does not experience frequent needs for extensions. If fiber connectors are used to keep reconfigurability, care has to be taken to reduce connector losses. As it is shown in Figure 41, a considerable portion of optical power and thus THz amplitude might be lost through reflections at air gap interfaces in fiber junctions. In the test setup, the amplitudes tripled when a refractive index matching gel to close these gaps was employed.

5.3.4 Time Delay Jitter

Like every transmission medium, optical fiber shows fluctuations of the propagation delay. So, in addition to the

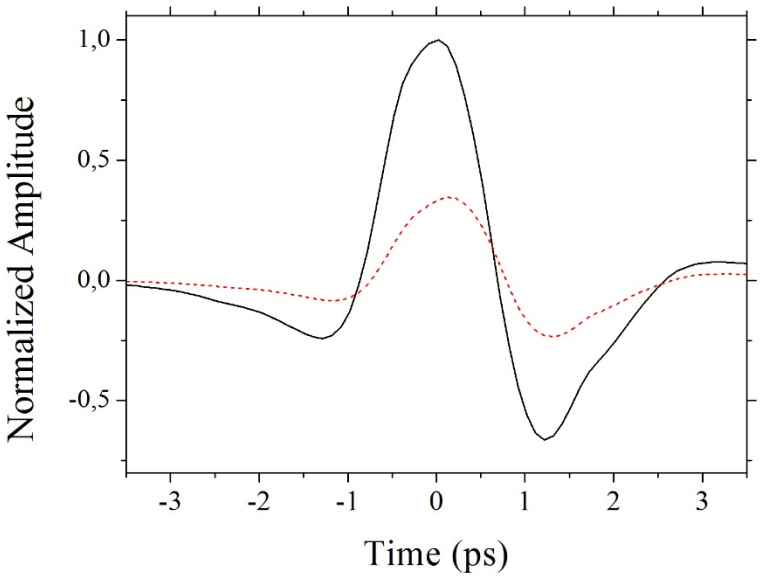

Figure 41. Influence of connector gaps: Use of index matching gel (solid line) and pulse suffering from connector gaps/reflections (dashed line)

optical source jitter, there are timing errors caused by the influence of thermal, acoustic, and mechanical disturbances on the optical fiber that result in fluctuations on the output pulse arrival time. For example, typical commercial fibers for optical communications show thermal coefficients of the propagation delay around $38\,ps/(km \cdot K)$ [182]. This change in *time of flight* of the optical pulses limits the maximum fiber length and the temperature operation range of the THz architecture. In a conventional THz-TDS system, where THz pulses are scanned in a few ps time window, unstabilized operation can be performed with a simple control on the MODL. However, faster inspection systems, e.g. [183], would require active stabilization methods [182, 184, 185], which can provide long-term timing stability with up to sub-femtosecond precision [185].

5.3.5 Polarization

It is well known that light polarization at the output of a long fiber section changes randomly over time [186]. To investigate the effect of polarization changes on the LTG-InGaAs/InAlAs-PCAs, a polarization controller was inserted in the fiber path. While the polarization was being changed continuously by a polarization controller to cover most states of polarization, the relative error of the THz pulse amplitude was measured to be $6.6 \cdot 10^{-3}$. For comparison, the same was performed without actively changing the polarization obtaining a relative error of $2.8 \cdot 10^{-3}$. It was observed that the relative error, calculated by making use of a temporal standard deviation, roughly doubles when the polarization was changed. However, the optical power reaching the THz emitter was assessed by the same method and it turned out that its standard deviation and relative error also double. It is assumed therefore that THz amplitude fluctuations were due to amplitude variations. Concluding, there does not seem to be a significant effect of polarization changes, which deteriorates the measured THz amplitudes and degrades the spectroscopy performance. Nevertheless, long-term polarization changes will provoke time jitter due to PMD and contribute to the timing errors described in Section 5.3.4.

Another issue to be taken into account is the polarization-dependence of the residual differential group delay (DGD). It gets stronger as the fiber path gets longer. To assess the DGD effect

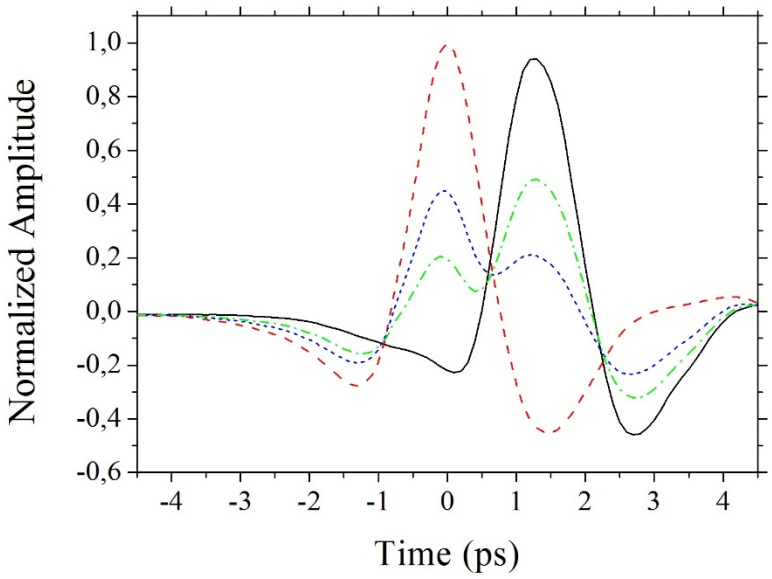

Figure 42. Varying THz pulse shapes due to PMD. The red and black lines correspond to polarizations along the orthogonal principal transverse fiber axes. The blue and green lines correspond to polarizations, in which both orthogonal components are present.

on THz generation, a SMF patch cord was replaced by a PMF, which shows a significantly larger DGD. Depending on the polarization, pulses reach the antennas with a different delay. When both polarization components are present, two orthogonally polarized pulses with temporal overlap emerge (see Figure 42). This superposition of delayed versions of the pulse leads to notch filtering in the frequency domain (see Figure 43). For long-haul systems, it is thus recommendable to employ PMF for the whole fiber circuitry to avoid polarization-induced dispersion and thus improve system stability in terms of amplitude and jitter.

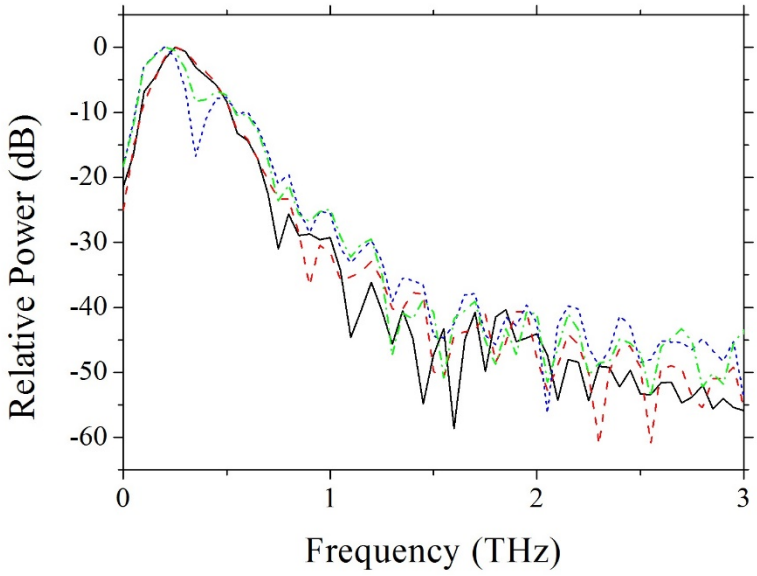

Figure 43. THz spectra affected by PMD. Spectra derived from pulse superposition (blue and green lines) exhibit a filtering notch around $350 - 400\ GHz$.

5.3.6 Noise Sources

The use of EDFAs in the centralized THz system adds a high degree of flexibility in the system and allows the distribution of the signal in many parallel links, improving the cost efficiency of the system. However, EDFAs introduce ASE noise to the THz emitters/receivers. To assess the effect of the use of EDFAs in THz sensing systems, a THz-TDS system has been modified to include a controlled ASE source. A piece of SMF has been replaced by a fiber coupler to enable the injection of an additional

signal from an ASE source to either the emitter or the receiver antenna.

Figure 44 shows the effect on the amplitude of the pulses when injecting different ASE levels into the emitter and the receiver, whereas Figure 45 compares the corresponding dynamic ranges. As can be seen, ASE noise reduces the amplitude of the THz signal, as shown in [187], for an additional continuous wave signal. This reduction in the amplitude of the THz pulses results in a degradation of the dynamic range although the ASE power levels considered here are considerably higher than expected values in a practical configuration. Low ASE noise levels reduce the amplitude almost negligibly and thus cause the dynamic

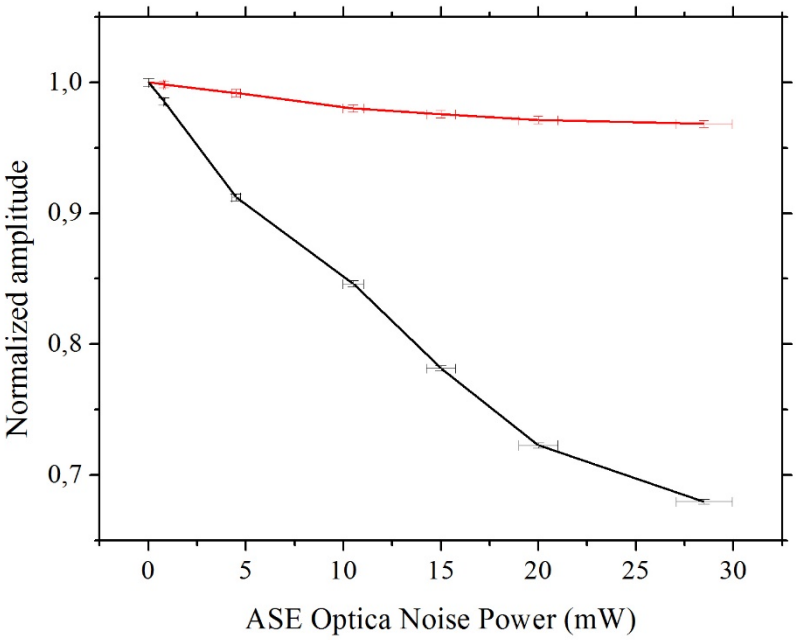

Figure 44. Effect of the injection of ASE noise into the emitter antenna (red triangles) and receiver antenna (black squares), in terms of amplitude of the THz pulses

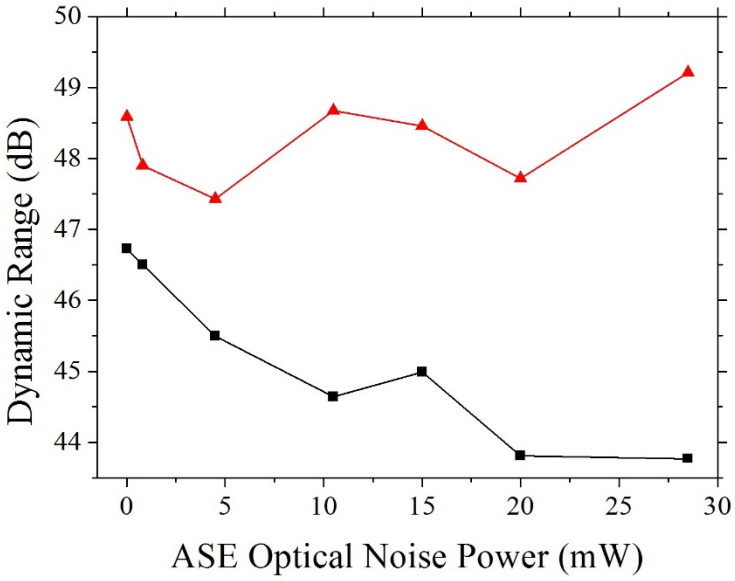

Figure 45. Dynamic range at ASE injection into the emitter antenna (red triangles) and receiver antenna (black squares)

range only to suffer minor degradations. Nevertheless, this effect can further be reduced by using a pre-amplifier configuration.

Additionally, ASE noise can induce time jitter, which will be combined with jitter sources commented in Section 5.3.4. For an input Gaussian pulse and the fiber lengths considered in this work ($100\,m$ and $25\,km$), an ASE-noise-induced time jitter contribution would be of the order of $0.1\,fs$ and $15\,fs$, respectively, according to estimations obtained from simulations carried out using *VPI Photonics* software.

6. Conclusion and Outlook

Terahertz waves can be exploited to gain information from a wide range of materials and processes thanks to the particular interactions in this spectral region. Although commercial solutions are available, further work is needed to extend the range of applications that can benefit from this technology.

Thanks to advances in the growth technology of photoconductors, new materials have been developed, which match the optical wavelength range traditionally employed in the telecommunication industry. Consequently, the formerly conventional THz technology has benefited by the use of optical fiber as a coupling and signal distribution medium with superior guiding properties. The outcome of the latter was the development of robust commercial spectrometers, replacing cumbersome and expensive free-space optics laboratory assemblies.

This thesis has aimed at studying some consequences that fiber-based THz technology have for the applicability of sensing solutions in this spectral region. Starting from the mechanisms in photoconductive antennas that allow remote all-optical control of the antenna dynamics through the injection of a continuous optical signal, the thesis advanced focusing on a THz fiber-based

system of rapid data capture enabled by fast optical delay scanning. Going another step upward on the size scale, the use of optical fiber has been proposed to build up an architecture for parallel and remote operation of an ensemble of spectrometer units, as they might occur in industrial or inspectional scenarios. Thus, the thesis includes studies at the level of device, instrument and large sensing system. The final goal of the thesis has been to contribute to the simplification of THz sensing instruments to ease their deployment in industrial scenarios.

In more detail, Chapter 3 has dealt with an all-optical alternative method for THz modulation. Besides conventional electrical and opto-mechanical modulation methods, this can be seen as a further way to control the THz emission in THz-TDS. In harsh industrial scenarios, signal distribution by optical fiber is less vulnerable to electromagnetic distortions and hence a considerable alternative to conventional techniques. This new technique has been proposed and phenomenological investigations of the influence of a continuous optical wave injected into a pulsed-mode THz spectrometer have been provided, including a physical explanation of the phenomenon.

Chapter 4 has investigated a THz-TDS system with rapid data capture. $40\,ps$ traces have been captured with $10\,Hz$ (double pass) at $0.5\,MSa/s$, what resulted in a delay step of $1\,fs$. The corresponding jitter on the delay axis, which is determined by the error of the optical sensor, has been ascertained statistically to be $\sim 0.8\,fs$ at this sampling rate. Proper alignment and subsequent averaging resulted in an increase of the DR of $(9.95 \pm 0.17)\,dB/dec$. Whilst optoelectronic delay schemes enable superior scanning rates, the fast mechanical delay line has proven to maintain the measurement quality, bandwidth and DR,

at the burden of a reduction of measurement speed, but also a reduction of the system cost. Measurement times lie still within some milliseconds up to few seconds, depending on the desired precision, and thus can be considered suitable for real world applications.

Finally, Chapter 5 has studied the implications of fiber technology to implement centralized large THz systems including a set of sensing points. The topical complex of industrial deployment was expanded by considerations of a centralized fiber-architecture. In a similar way as in optical centralized schemes in communication systems, such as *Passive Optical Networks* (PON), *Radio over Fiber* (RoF), etc., optical fiber can be deployed to reduce the cost of spectroscopy instruments in applications by exploiting parallelism. The feasibility and performance of this approach was analyzed. The use of robust optical fiber distribution links eases deployment in industrial scenarios, while source sharing permits reduction of the total cost of up to 50%. Limitations, such as chromatic dispersion, nonlinear effects in fiber, fiber joint impairments, time delay jitter, polarization and ASE noise were investigated. The residual dispersion, affecting the bandwidth via carrier generation and relaxation, results from inaccurate compensation as well as temperature and polarization variations. This work shows that besides conventional advantages, like remote and accurate feeding of PCAs and overall robust implementations of THz-sensing systems, a centralized fiber architecture is further capable to reduce the cost and complexity and ease the control of THz sensing solutions.

Further work is needed in the field of THz technology for further reductions in cost and complexity of THz systems.

Performance enhancement is always welcome, but probably cost is the key limiting factor at the moment. More compact and cost-effective THz solutions able to reach a wider range of industrial scenarios are crucial. In turn, as in many other technologies, this will lead to a feedback loop of further cost reduction through higher volume.

References

[1] T. Maiman, "Stimulated Optical Radiation in Ruby," *Nature,* vol. 187, no. 4736, pp. 493 - 494, 1960.

[2] Y.-S. Lee, Principles of Terahertz Science and Technology, New York: Springer Science+Business Media, LLC, 2009.

[3] D. Auston, "Picosecond Optoelectronic Switching and Gating in Silicon," *Appl. Phys. Lett.,* vol. 26, no. 3, pp. 101 - 103, 1975.

[4] C. Lee, "Picosecond Optoelectronic Switching in GaAs ," *Appl. Phys. Lett. 30,* vol. 30, no. 2, pp. 84 - 86, 1977.

[5] S. Nishizawa, K. Sakai, M. Hangyo, T. Nagashima, M. W. Takeda, K. Tominaga, A. Oka, K. Tanaka and O. Morikawa, "Terahertz Time-Domain Spectroscopy," in *Terahertz Optoelectronics*, Berlin, Springer Science+Business Media, 2005, pp. 203 - 270.

[6] S. L. Dexheimer, Terahertz Spectroscopy: Principles and Applications, S. L. Dexheimer, Ed., Boca Raton, Florida: CRC Press, Taylor & Francis Group, LLC, 2008.

[7] D. Grischkowsky, S. Keiding, M. v. Exter and C. Fattinger, "Far-infrared Time-domain Spectroscopy with Terahertz Beams of Dielectrics and Semiconductors," *J. of the Opt. Soc. Am. B,* vol. 7, no. 10, pp. 2006 - 2015, October 1990.

[8] M. C. Nuss and J. Orenstein, "Terahertz Time-domain Spectroscopy," in *Millimeter and Submillimeter Wave Spectroscopy of Solids*, vol. 74, G. Grüner, Ed., Springer Berlin Heidelberg, 2007, pp. 7 - 50.

[9] M. Naftaly, R. G. Clarke, D. A. Humphreys and N. M. Ridler, "Metrology State-of-the-Art and Challenges in Broadband Phase-Sensitive Terahertz Measurements," *Proceedings of the IEEE,* no. 99, pp. 1-15, 2017.

[10] H. Cai, D. Wang and J. Shen, "Study of Atmospheric Pollution Using Terahertz Wave," in *Proc. SPIE 7854, Infrared, Millimeter Wave, and Terahertz Technologies*, Beijing, 2010.

[11] C. D. Stoik, M. J. Bohn and J. L. Blackshire, "Nondestructive Evaluation of Aircraft Composites Using Transmissive Terahertz Time Domain Spectroscopy," *Opt. Expr.,* vol. 16, no. 21, pp. 17039 - 17051, 13 October 2008.

[12] S. Oka, S. Mochizuki, H. Togo and N. Kukutsu, "Inspection of Concrete Structures Using Millimeter-wave Imaging Technology," *NTT Techn. Rev.,* vol. 7, no. 3, pp. 1 - 6, 2009.

[13] T. Kurabayashi, L. Zhen, P. Plotka, M. Watanaba, Y. Oyama and J. Nishizawa, "Sub-terahertz Imaging for Construction Materials," in *33rd International Conference on Infrared, Millimeter and Terahertz Waves*, Pasadena, 2008.

[14] P. U. Jepsen, D. G. Cooke and M. Koch, "Terahertz Spectroscopy and Imaging - Modern Techniques and

Applications," *Laser & Photonics Reviews,* vol. 5, no. 1, pp. 124 - 166, 2011.

[15] R. Bogue, "Terahertz Imaging: A Report on Progress," *Sensor Rev.,* vol. 29, no. 1, pp. 6 - 12, 2009.

[16] Y. Sun, M. Y. Sy, Y.-X. J. Wang, A. T. Ahuja, Y.-T. Zhang and E. Pickwell-MacPherson, "A Promising Diagnostic Method: Terahertz Pulsed Imaging and Spectroscopy," *World J. Radiol.,* vol. 3, no. 3, pp. 55 - 65, 28 March 2011.

[17] Z. D. Taylor, R. S. Singh, D. B. Bennett, P. Tewari, C. P. Kealey, N. Bajwa, M. O. Culjat, A. Stojadinovic, H. Lee, J.-P. Hubschman, E. R. Brown and W. S. Grundfest, "THz Medical Imaging: In Vivo Hydration Sensing," *IEEE Transact. on THz Sci. and Technol.,* vol. 1, no. 1, pp. 201 - 219, 31 August 2011.

[18] J. P. Guillet, B. Recur, L. Frederique, B. Bousquet, L. Canioni, I. Manek-Hönninger, P. Desbarats and P. Mounaix, "Review of Terahertz Tomography Techniques," *J. of Infrared, Millimeter and Terahertz Waves,* vol. 35, no. 4, pp. 382 - 411, 2014.

[19] D. A. Zimdars, "Fiber-pigtailed Terahertz Time Domain Spectroscopy Instrumentation for Package Inspection and Security Imaging," in *Proc. SPIE 5070, Terahertz for Military and Security Applications*, Orlando, 2003.

[20] A. Chebotarev and G. Chebotareva, "Commercialization of THz-IR Photonics for Homeland Security and Material Inspection," in *Photonic*

Applications Systems Technologies Conference, San Francisco, 2004.

[21] N. W. Karl, R. W. McKinney, Y. Monnai, R. Mendis and D. Mittleman, "Frequency-division Multiplexing in the Terahertz Range Using a Leaky-wave Antenna," *Nature Photonics,* vol. 9, pp. 717 - 720, 2015.

[22] I. F. Akyildiz, J. M. Jornet and C. Han, "Terahertz Band: Next Frontier for Wireless Communications," *Physical Communication,* vol. 12, pp. 16 - 32, September 2014.

[23] T. Kleine-Ostmann and T. Nagatsuma, "A Review on Terahertz Communications Research," *J. Infrared Millimeter and Terahertz Waves,* vol. 32, pp. 143 - 171, 2011.

[24] M. Koch, "Terahertz Communications: A 2020 Vision," in *Terahertz Frequency Detection and Identification of Materials and Objects*, vol. 19, R. Miles, X. Zhang, H. Eisele and A. Krotkus, Eds., Springer, 2007, p. 325 – 338.

[25] A. I. McIntosh, B. Yang, S. M. Goldup, M. Watkinsonb and R. S. Donnan, "Terahertz Spectroscopy: A Powerful New Tool for the Chemical Sciences?," *Chem. Soc. Rev.,* vol. 41, no. 6, pp. 2072 - 2082, 2012.

[26] B. Fischer, M. Hoffmann, H. Helm, G. Modjesch and P. U. Jepsen, "Chemical Recognition in Terahertz Time-Domain Spectroscopy and Imaging," *Semicond.*

Sci. and Technol., vol. 20, no. 7, pp. 246 - 253, 8 June 2005.

[27] C. K. Walker, Terahertz Astronomy, Boca Raton: CRC Press, Taylor & Francis Group, 2016.

[28] B. Choudhury, A. R. Sonde and R. M. Jha, Terahertz Antenna Technology for Space Applications, Singapore: Springer Science+Business Media, 2016.

[29] P. H. Siegel, "Terahertz Technology," *IEEE Trans. Microwave Theory Tech.,* vol. 50, no. 3, pp. 910 - 928, 2002.

[30] P. Siegel, "http://www.nasa.gov/audience/foreducators/k-4/features/Peter_Siegel.html," NASA, 2004. [Online].

[31] C. Paoloni, L. Yue, X. Tang, F. Zhang, B. Popovic, L. Himes, R. Barchfeld, D. Gamzina, R. Letizia, M. Mineo and N. C. Luhmann, "THz Backward-Wave Oscillators for Plasma Diagnostic in Nuclear Fusion," in *2015 IEEE International Conference on Plasma Sciences (ICOPS)*, Antalya, Turkey, 2015.

[32] B. Vidal, T. Nagatsuma, N. J. Gomes and T. E. Darcie, "Photonic Technologies for Millimeter- and Submillimeter-Wave Signals," *Adv. in Opt. Technol.,* vol. 2012, pp. Article ID 925065, 18 pages, September 2012.

[33] G. Dodel, "On the History of Far-Infrared (FIR) Gas Lasers: Thirty-five Years of Research and Application," *Infrared Phys. & Technol.,* vol. 40, no. 3, pp. 127 - 139, 1999.

[34] C. Sirtori, S. Barbieri and R. Colombelli, "Wave Engineering with THz Quantum Cascade Lasers," *Nat. Phot.,* vol. 7, p. 691 – 701, 2013.

[35] G. Scalari, C. Walther, M. Fischer, R. Terazzi, H. Beere, D. Ritchie and J. Faist, "THz and Sub-THz Quantum Cascade Lasers," *Laser & Photon. Rev.,* vol. 3, no. 1 - 2, pp. 45 - 66, 2008.

[36] R. Köhler, A. Tredicucci, F. Beltram, H. E. Beere, E. H. Linfield, A. G. Davies, D. A. Ritchie, R. C. Iotti and F. Rossi, "Terahertz Semiconductor-heterostructure Laser," *Nature,* vol. 417, pp. 156 - 159, 2002.

[37] M. Razeghi, N. Bandyopadhyay, Y. Bai, Q. Lu and S. Slivken, "Recent advances in mid infrared (3–5 μm) Quantum Cascade Lasers," *Opt. Mater. Expr.,* vol. 3, no. 11, p. 1872 – 1884, 2013.

[38] Q. Lu and M. Razeghi, "Recent Advances in Room Temperature, High-Power Terahertz Quantum Cascade Laser Sources Based on Difference-Frequency Generation," *Photonics,* vol. 3, no. 42, p. 10 pages, 2016.

[39] G. Kozlov and A. Volkov, "Coherent Source Submillimeter Wave Spectroscopy," in *Millimeter and Submillimeter Wave Spectroscopy of Solids*, vol. 74, G. Grüner, Ed., Berlin, Springer-Verlag, 1998, pp. 51 - 109.

[40] C. A. Brau, "Free-electron lasers," *Science,* vol. 239, no. 4844, pp. 1115 - 1121, 1988.

[41] P. L. Richards, "Bolometers for Infrared and Millimeter Waves," *J. Appl. Phys.,* vol. 76, no. 1, pp. 1 - 24, 1994.

[42] H. P. Beerman, "The Pyroelectric Detector of Infrared Radiation," *IEEE Trans. on Electron. Devices,* vol. 16, no. 6, pp. 554 - 557, 1969.

[43] M. J. E. Golay, "Theoretical and practical sensitivity of the Pneumatic Infrared Detector," *Rev. Sci. Inst.,* vol. 20, pp. 816 - 820, 1949.

[44] N. Karpowicz, H. Zhong, J. Xu, K.-I. Lin, J.-S. Hwang and X.-C. Zhang, "Comparison Between Pulsed Terahertz Time-domain Imaging and Continuous Wave Terahertz Imaging," *Semicond. Sci. and Technol.,* vol. 20, no. 7, pp. 293 - 299, 2005.

[45] D. Saeedkia, R. R. Mansour and S. Safavi-Naeini, "The Interaction of Laser and Photoconductor in a Continuous-Wave Terahertz Photomixer," *IEEE J. of Quant.-Electron.,* vol. 41, no. 9, pp. 1188 - 1196, 2005.

[46] J. Mangeney, A. Merigault, N. Zerounian and P. Crozat, "Continuous Wave Terahertz Generation up to 2 THz by Photomixing on Ion-irradiated In0.53Ga0.47As at 1.55 μm Wavelengths," *Appl. Phys. Lett.,* vol. 91, no. 241102, p. 3, 2007.

[47] S. Preu, M. Mittendorff, H. Lu, H. B. Weber, S. Winnerl and A. C. Gossard, "1550 nm ErAsIn(Al)GaAs Large Area Photoconductive Emitters," *Appl Phys. Lett.,* vol. 101, no. 10, p. 101105 (4pp), 2012.

[48] S. Winnerl, "Scalable Microstructured Photoconductive Terahertz Emitters," *J. of Infrared,*

Millimeter and Terahertz Waves, vol. 33, no. 4, pp. 431 - 454, 2012.

[49] S. Preu, G. H. Döhler, S. Malzer, L. J. Wang and A. C. Gossard, "Tunable, Continuous-Wave Terahertz Photomixer Sources and Applications," *J. of Appl. Phys.,* vol. 109, no. 6, p. 061301, 2011.

[50] M. Tani, P. Gu, M. Hyodo, K. Sakai and T. Hidaka, "Generation of Coherent Terahertz Radiation by Photomixing of Dual-mode Lasers," *Opt. and Quant. Electron.,* vol. 32, no. 4, pp. 503 - 520, 2000.

[51] M. Tani, O. Morikawa, S. Matsuura and M. Hangyo, "Generation of Terahertz Radiation by Photomixing with Dual- and Multiple-mode Lasers," *Semicond. Sci. and Technol.,* vol. 20, no. 7, pp. 151 - 163, 2005.

[52] R. Sowade, I. Breunig, I. C. Mayorga, J. Kiessling, C. Tulea, V. Dierolf and K. Buse, "Continuous-wave Optical Parametric Terahertz Source," *Opt. Expr.,* vol. 17, no. 25, pp. 22303 - 22310, 2009.

[53] J. A. Fülöp, L. Pálfalvi, G. Almási and J. Hebling, "Design of High-Energy Terahertz Sources Based on Optical Rectification," *Opt. Expr.,* vol. 18, no. 12, pp. 12311 - 12327, 7 June 2010.

[54] E. Castro-Camus and M. Alfaro, "Photoconductive Devices for Terahertz Pulsed Spectroscopy: A Review," *Photon. Res.,* vol. 4, no. 3, pp. A36 - A42, 2016.

[55] C. Henry, R. Logan, F. Merritt and C. Bethea, "Radiative and Nonradiative Lifetimes in n-Type and

p-Type 1.6 μm InGaAs," *Electron. Lett.,* vol. 20, no. 9, pp. 358 - 359, 1984.

[56] R. B. J. Dietz, B. Globisch, M. Gerhard, A. Velauthapillai, D. Stanze, H. Roehle, M. Koch, T. Göbel and M. Schell, "64 μW Pulsed Terahertz Emission from Growth Optimized InGaAs/InAlAs Heterostructures with Separated Photoconductive and Trapping Regions," *Appl. Phys. Lett.,* vol. 103, no. 6, p. 061103 (4 pp), August 2013.

[57] R. B. J. Dietz, B. Globisch, H. Roehle, D. Stanze, T. Göbel and M. Schell, "Influence and Adjsutment of Carrier Lifetimes in InGaAs/InAlAs Photoconductive Pulsed Terahertz Detectors: 6 THz Bandwidth and 90 dB dynamic range," *Opt. Expr.,* vol. 22, no. 16, pp. 19411 - 19422, 11 Ausgust 2014.

[58] S. C. Corzo-Garcia, M. Alfaro and E. Castro-Camus, "Transit Time Enhanced Bandwidth in Nanostructured Terahertz Emitters," *J. of Infrared, Millimeter, and Terahertz Waves,* vol. 35, no. 12, pp. 987 - 992, December 2014.

[59] N. T. Yardimci, H. Lu and M. Jarrahi, "High Power Telecommunication-Compatible Photoconductive Terahertz Emitters Based on Plasmonic Nano-Antenna Arrays," *Appl. Phys. Lett.,* vol. 109, no. 191103, 2016.

[60] L. Duvillaret, F. Garet, J.-F. Roux and J.-L. Coutaz, "Analytical Modeling and Optimization of Terahertz Time-domain Spectroscopy Experiments Using Photoswitches as Antennas," *IEEE J. on Select.*

Topics in Quant. Electr., vol. 7, no. 4, pp. 615 - 623, July 2001.

[61] Q. Wu and X.-C. Zhang, "Design and Characterization of Traveling-wave Electrooptic Terahertz Sensors," *IEEE J. Sel. Top. Quantum Electron.,* vol. 2, no. 3, pp. 693 - 700, September 1996.

[62] J. Hebling, G. Almási and I. Z. Kozma, "Velocity matching by Pulse Front Tilting for Large-area THz-pulse Generation," *Opt. Expr.,* vol. 10, no. 21, pp. 1161 - 1166, 21 October 2002.

[63] Y.-S. Lee, T. Meade, V. Perlin, H. Winful, T. Norris and A. Galvanauskas, "Generation of Narrow-band Terahertz Radiation via Optical Rectification of Femtosecond Pulses in Periodically Poled Lithium Niobate," *Appl. Phys. Lett.,* vol. 76, no. 18, pp. 2505 - 2507, 2000.

[64] M. Schall, H. Helm and S. R. Keiding, "Far Infrared Properties of Electro-optic Crystals Measured by THz Time-domain Spectroscopy," *Int. J. of Infrared and Millimeter Waves,* vol. 20, no. 4, pp. 595 - 604, April 1999.

[65] C. Ruchert, C. Vicario and C. P. Hauri, "Scaling Submillimeter Single-cycle Transient toward Megavolts per Centimeter Field Strength via Optical Rectification in the Organic Crystal OH1," *Opt. Lett.,* vol. 37, no. 5, pp. 899 - 901, 1 March 2012.

[66] F. Brunner, O.-P. Kwon, S.-J. Kwon, M. Jazbinsek, A. Schneider and P. Günter, "A Hydrogen-bonded Organic Nonlinear Optical Crystal for High-efficiency

Terahertz Generation and Detection," *Opt. Expr.,* vol. 16, no. 21, pp. 16496 - 16508, 2008.

[67] O.-P. Kwon, S.-J. Kwon, M. Jazbinsek, F. Brunner, J.-I. Seo, C. Hunziker, A. Schneider, H. Yun, Y.-S. Lee and P. Günter, "Organic Phenolic Configurationally Locked Polyene Single Crystals for Electro-optic and Terahertz Wave Applications," *Adv. Funct. Mater.,* vol. 18, pp. 3242 - 3250, 2008.

[68] C. Hunziker, S.-J. Kwon, H. Figi, F. Juvalta, O.-P. Kwon, M. Jazbinsek and P. Günter, "Configurationally Locked, Phenolic Polyene Organic Crystal 2-{3-(4-hydroxystyryl)-5,5-dimethylcyclohex-2-enylidene}malononitrile: Linear and Nonlinear Optical Properties," *J. Opt. Soc. Am. B,* vol. 25, pp. 1678 - 1683, 2008.

[69] M. N. A. Schneider, M. Stillhart, B. Ruiz, R. U. A. Khan and P. Günter, "Generation of Terahertz Pulses through Optical Rectification in Organic DAST Crystals: Theory and Experiment," *J. Opt. Soc. Am. B,* vol. 23, no. 9, pp. 1822 - 1835, September 2006.

[70] K. Kawase, M. Mizuno, S. Sohma, H. Takahashi, T. Taniuchi, Y. Urata, S. Wada, H. Tashiro and H. Ito, "Difference-frequency Terahertz-wave Generation from 4-dimethylamino-N-methyl-4-stilbazolium-tosylate by Use of an Electronically Tuned Ti:sapphire Laser," *Opt. Lett.,* vol. 24, pp. 1065 - 1067, 1999.

[71] T. Taniuchi, S. Okada and H. Nakanishi, "Widely Tunable Terahertz-wave Generation in an Organic

Crystal and its Spectroscopic Application," *J. Appl. Phys.,* vol. 95, no. 11, pp. 5984 - 59888, 2004.

[72] A. Schneider, M. Stillhart and P. Günter, "High Efficiency Generation and Detection of Terahertz Pulses Using Laser Pulses at Telecommunication Wavelengths," *Opt. Expr.,* vol. 14, no. 12, pp. 5376 - 5384, 2006.

[73] M. Stillhart, A. Schneider and P. Günter, "Optical Properties of 4-N,N-dimethylamino-4'-N'-methyl-stilbazolium 2,4,6-trimethylbenzenesulfonate crystals at Terahertz Frequencies," *J. Opt. Soc. Am. B,* vol. 25, no. 11, pp. 1914 - 1919, November 2008.

[74] L. Mutter, F. D. J. Brunner, Z. Yang, M. Jazbinsek and P. Günter, "Linear and Nonlinear Optical Properties of the Organic Crystal DSTMS," *J. Opt. Soc. Am. B,* vol. 24, no. 9, pp. 2556 - 22561, September 2007.

[75] Z. Yang, M. Jazbinsek, S. A. B. Ruiz, V. Gramlich and P. Günter, "Molecular Engineering of Stilbazolium Derivatives for Second-order Nonlinear Optics," *Chem. Mater.,* vol. 19, no. 14, pp. 3512 - 3518, 6 September 2007.

[76] Z. Yang, L. Mutter, M. Stillhart, B. Ruiz, S. Aravazhi, M. Jazbinsek, A. Schneider, V. Gramlich and P. Günter, "Large-size Bulk and Thin-film Stilbazolium-salt Single Crystals for Nonlinear Optics and THz Generation," *Adv. Funct. Mater.,* vol. 17, no. 13, pp. 2018 - 2023, 2 August 2007.

[77] P. F. Moulton, "Spectroscopic and Laser Characteristics of Ti:Al2O3," *J. of Opt. Soc. Am. B,* vol. 3, no. 1, p. 125 – 133, 1986.

[78] P. Brochure, "Ultrafast Fiber Lasers: The Next Generation - Reliable, Robust, Flexible," Toptica Photonics AG, Graefelfing / Munich, 2015.

[79] J. V. Rudd, D. A. Zimdars and M. W. Warmuth, "Compact Fiber-Pigtailed Terahertz Imaging System," in *Proc. SPIE 3934, Commercial and Biomedical Applications of Ultrafast Lasers II*, San José, California, 2000.

[80] B. Sartorius, H. Roehle, H. Künzel, J. Böttcher, M. Schlak, D. Stanze, H. Venghaus and M. Schell, "All-fiber Terahertz Time-domain Spectrometer Operating at 1.5 µm Telecom Wavelengths," *Opt. Expr.,* vol. 16, no. 13, pp. 9565 - 9570, 23 June 2008.

[81] K. I. Kang, K.-L. Deng, S. D. Koehler and I. G. a. P. R. Prucnal, "Fabrication of precision fiber-optic time delays with in situ monitoring for subpicosecond accuracy," *Appl. Opt.,* vol. 36, no. 12, pp. 2533 - 2536, 1997.

[82] L. Thévenaz, "Slow and fast light in optical fibres," *Nature Phot.,* vol. 2, pp. 474 - 481, 2008.

[83] J. Palací and B. Vidal, "Tunable Optical Delay Line based on Single-Sideband Suppressed-Carrier Modulation," *IEEE Phot. Technol. Lett.,* vol. 25, no. 1, pp. 43 - 46, 2013.

[84] M. Skorobogatiy, "Linear Rotary Optical Delay Lines," *Opt. Expr.,* vol. 22, no. 10, pp. 11812 - 111833, 19 May 2014.

[85] G.-J. Kim, S.-G. Jeon, J.-I. Kim and S.-T. Han, "A Novel Optical Delay Line Using a Rotating Planar Reflector for Fast Measurement of a Terahertz Pulse," *J. of the Korean Phys. Soc.,* vol. 56, no. 6, pp. 1763 - 1766, June 2010.

[86] J. Xu, Z. Lu and X.-C. Zhang, "Compact Involute Optical Delay Line," *Electr. Lett.,* vol. 40, no. 19, pp. 1218 - 1219, 2004.

[87] G.-J. Kim, S.-G. Jeon, J.-I. Kim and Y.-S. Jin, "Terahertz Pulse Detection Using Rotary Optical Delay Line," *Jap. J. of Appl. Phys.,* vol. 46, no. 11, pp. 7332 - 7335, 6 November 2007.

[88] N. Vieweg, F. Rettich, A. Deninger, H. Roehle, R. Dietz, T. Göbel and M. Schell, "Terahertz-Time Domain Spectrometer with 90 dB Dynamic Range," *J. of Infrared, Millimeter and Terahertz Waves,* vol. 35, no. 10, pp. 823 - 832, October 2014.

[89] A. Bartels, F. Hudert, C. Janke, T. Dekorsy and K. Köhler, "Femtosecond Time-resolved Optical Pump-probe Spectroscopy at Kilohertz-scan-rates over Nanosecond-time-delays without Mechanical Delay Line," *Appl. Phys. Lett.,* vol. 88, no. 4, p. 041117 (3 pp), January 2006.

[90] T. Yasui, E. Saneyoshi and T. Araki, "Asynchronous Optical Sampling Terahertz Time-domain Spectroscopy for Ultrahigh Spectral Resolution

and Rapid Data Acquisition," *Appl. Phys. Lett.,* vol. 87, p. 061101 (3 pp), 1 August 2005.

[91] P. A. Elzinga, R. J. Kneisler, F. E. Lytle, Y. Jiang, G. B. King and N. M. Laurendeau, "Pump/probe Method for Fast Analysis of Visible Spectral Signatures Utilizing Asynchronous Optical Sampling," *Appl. Opt.,* vol. 26, no. 19, pp. 4303 - 4309, 1 October 1987.

[92] P. A. Elzinga, F. E. Lytle, Y. Jian, G. B. King and M. Laurendeau, "Pump/Probe Spectroscopy by Asynchronous Optical Sampling," *Appl. Spectroscopy,* vol. 41, no. 1, pp. 2 - 4, 1987.

[93] B. Schmidt, "Pump-probe Spectroscopy without Mechanical Delay," Menlo Systems GmbH, Martinsried, 2009.

[94] T. Hochrein, R. Wilk, M. Mei, R. Holzwarth, N. Krumbholz and M. Koch, "Optical Sampling by Laser Cavity Tuning," *Opt. Expr.,* vol. 18, no. 2, pp. 1613 - 1617, 2010.

[95] R. Wilk, T. Hochrein, M. Koch, M. Mei and R. Holzwarth, "OSCAT: Novel Technique for Time-Resolved Experiments Without Moveable Optical Delay Lines," *J. of Infrared, Millimeter, and Terahertz Waves,* vol. 32, no. 5, pp. 596 - 602, 2010.

[96] R. Wilk, T. Hochrein, M. Koch, M. Mei and R. Holzwarth, "Terahertz Spectrometer Operation by Laser Repetition Frequency Tuning," *J. Opt. Soc. Am. B,* vol. 28, no. 4, pp. 592 - 595, 2011.

[97] R. Wilk, "All Fiber THz Spectrometer for Plastics Industry," *Bulletin of the Polish Academy of Sciences,*

Technical Sciences, vol. 59, no. 3, pp. 283 - 285, 25 November 2011.

[98] F. Tauser, C. Rausch, J. H. Posthumus and F. Lison, "Electronically Controlled Optical Sampling Using 100 MHz Repetition Rate Fiber Lasers," in *Proc. of SPIE 6881*, San José, 2008.

[99] Y. Kim and D.-S. Yee, "Electronically Controlled Optical Sampling Terahertz Time-Domain Spectroscopy," in *35th International Conference on Infrared, Millimeter, and Terahertz Waves* , Rome, 2010.

[100] Y. Kim and D.-S. Yee, "High-speed Terahertz Time-domain Spectroscopy Based on Electronically Controlled Optical Sampling," *Opt. Lett.,* vol. 35, no. 22, pp. 3715 - 3717, 2010.

[101] J. Posthumus, "Terahertz with Electronic Delay," Fs-Laser Applications, Weinheim, 2012.

[102] J. Posthumus, "Low-jitter Laser Synchronisation and ECOPS," Toptica Photonics, Gräfelfing, 2012.

[103] R. J. B. Dietz, N. Vieweg, T. Puppe, A. Zach, B. Globisch, T. Göbel, P. Leisching and M. Schell, "All Fiber-coupled THz-TDS System with kHz Measurement Rate Based on Electronically Controlled Optical Sampling," *Opt. Lett.,* vol. 39, no. 22, pp. 6482 - 6484, 15 November 2014.

[104] O. Schubert, M. Eisele, V. Crozatier, N. Forget, D. Kaplan and R. Huber, "Rapid-scan Acousto-optical Delay Line with 34 kHz Scan Rate and 15 as Precision,"

Opt. Lett., vol. 38, no. 15, pp. 2907 - 2910, 1 August 2013.

[105] F. D. J. Brunner, A. Schneider and P. Gunter, "A Terahertz Time-Domain Spectrometer for Simultaneous Transmission and Reflection Measurements at Normal Incidence," *Opt. Expr.,* vol. 17, no. 23, pp. 20684 - 20693, 2009.

[106] M. Naftaly and R. Dudley, "Methodology for Determining the Dynamic Ranges and Signal-to-Noise Ratios of Terahertz Time-Domain Spectrometers," *Opt. Lett.,* vol. 34, no. 8, pp. 1213 - 1215, 2009.

[107] P. U. Jepsen and B. M. Fischer, "Dynamic Range in Terahertz Time-domain Transmission and Reflection Spectroscopy," *Opt. Lett.,* vol. 30, no. 1, pp. 29 - 31, 1 January 2005.

[108] S. P. Mickan, D. Abbott, J. Munch and X.-C. Zhang, "Noise Reduction in Terahertz Thin Film Measurements Using a Double Modulated Differential Technique," *Fluct. Noise Lett.,* vol. 2, no. 1, pp. R13 - R28, 2002.

[109] S. P. Mickan, K.-S. Lee, T.-M. Lu, J. Munch, D. Abbott and X.-C. Zhang, "Double Modulated Differential THz-TDS for a Thin Film Dielectric Characterization," *Microelectron. J.,* vol. 33, no. 12, pp. 1033 - 1042, December 2002.

[110] Z. Jiang, M. Li and X.-C. Zhang, "Dielectric Constant Measurement of Thin Films by Differential Time-domain Spectroscopy," *Appl. Phys. Lett.,* vol. 76, no. 22, pp. 3221 - 3223, 29 May 2000.

[111] M. Scheller, "Data Extraction from Terahertz Time Domain Spectroscopy Measurements," *J. of Infrared, Millimeter, and Terahertz Waves,* vol. 35, no. 8, pp. 638 - 648, August 2014.

[112] T.-. D. Dorney, R. G. Baraniuk and D. M. Mittleman, "Material Parameter Estimation with Terahertz Time-domain Spectroscopy," *J. Opt. Soc. Am. A,* vol. 18, no. 7, pp. 1562 - 1571, July 2001.

[113] L. Duvillaret, F. Garet and J.-L. Coutaz, "Influence of Noise on the Characterization of Materials by Terahertz Time-domain Spectroscopy," *J. Opt. Soc. Am. B,* vol. 17, no. 3, pp. 452 - 461, March 2000.

[114] L. Duvillaret, F. Garet and J.-L. Coutaz, "A Reliable Method for Extraction of Material Parameters in Terahertz Time-domain Spectroscopy," *IEEE J. of Select. Topics in Quant. Electron.,* vol. 2, no. 3, pp. 739 - 746, September 1996.

[115] W. Withayachumnankul, B. Ferguson, T. Rainsford, S. P. Mickan and D. Abbott, "Material Parameter Extraction for Terahertz Time-domain Spectroscopy," in *Proc. of SPIE, Photonic Materials, Devices, and Applications*, Bellingham, 2005.

[116] F. Sanjuan and B. Vidal, "Refractive Index Calculation from Echo Interface in Pulsed Terahertz Spectroscopy," *Electr. Lett.,* vol. 50, no. 4, pp. 308 - 309, 13 February 2014.

[117] M. Scheller, C. Jansen and M. Koch, "Analyzing Sub-100-μm Samples with Transmission Terahertz

Time Domain Spectroscopy," *Opt. Comm.,* vol. 282, no. 7, pp. 1304 - 1306, 1 April 2009.

[118] M. Scheller and M. Koch, "Fast and Accurate Thickness Determination of Unknown Material Using Terahertz Time Domain Spectroscopy," *J. of Infrared, Millimeter, and Terahertz Waves,* vol. 30, no. 7, pp. 762 - 769, July 2009.

[119] F. Sanjuan, A. Bockelt and B. Vidal, "Determination of Refractive Index and Thickness of a Multilayer Structure with a Single Terahertz Time Domain Spectroscopy Measurement," *Appl. Opt.,* vol. 53, no. 22, pp. 4910 - 4913, 1 August 2014.

[120] F. Sanjuan, A. Bockelt and B. Vidal, "Birefringence Measurement in the Terahertz Range Based on Double Fourier Analysis," *Opt. Lett.,* vol. 39, no. 4, pp. 809 - 812, 15 February 2014.

[121] D. H. Auston, K. P. Cheung and P. R. Smith, "Picosecond Photoconducting Hertzian Dipoles," *Appl. Phys. Lett.,* vol. 45, no. 3, pp. 284 - 286, 1984.

[122] C. Fattinger and D. Grischkowsky, "Terahertz Beams," *Appl. Phys. Lett.,* vol. 54, no. 6, pp. 490 - 492, 1989.

[123] F. W. Smith, H. Q. Le, V. Diadiuk, M. A. Hollis, A. R. Calawa, S. Gupta, M. Frankel, D. R. Dykaar, G. A. Mourou and T. Y. Hsiang, "Picosecond GaAs-based Photoconductive Optoelectronic Detectors," *Appl. Phys. Lett.,* vol. 54, no. 10, pp. 890 - 898, 1989.

[124] A. C. Warren, N. Katzenellenbogen, D. Grischkowsky, J. M. Woodall, M. R. Melloch and N.

Otsuka, "Subpicosecond, Freely Propagating Electromagnetic Pulse Generation and Detection Using GaAs:As Epilayers," *Appl. Phys. Lett.,* vol. 58, no. 14, pp. 1512 - 1514, 1991.

[125] C. Baker, I. S. Gregory, W. R. Tribe, I. V. Bradley, M. J. Evans, E. H. Linfield and M. Missous, "High Resistive Annealed Low-temperature-grown InGaAs with Sub-500 fs Carrier Lifetime," *Appl. Phys. Lett.,* vol. 85, no. 21, pp. 4965 - 4967, 2004.

[126] M. Suzuki and M. Tonouchi, "Fe-implanted InGaAs Photoconductive Terahertz Detectors Triggered by 1.56 μm Femtosecond Optical Pulses," *Appl. Phys. Lett.,* vol. 86, no. 1 - 3, p. 163504, 2005.

[127] J. Sigmund, C. Sydlo, H. L. Hartnagel, N. Benker, H. Fuess, F. Rutz, T. Kleine-Ostmann and M. Koch, "Structure Investigation of Low-temperature-grown GaAsSb, a Material for Photoconductive Terahertz Antennas," *Appl. Phys. Lett.,* vol. 87, no. 252103, pp. 1 - 3, 2005.

[128] H. Künzel, J. Böttcher, R. Gibis and G. Urmann, "Material Properties of Ga0.47In0.53As Grown on InP by Low-temperature Molecular Beam Epitaxy," *Appl. Phys. Lett.,* vol. 61, no. 11, pp. 1347 - 1349, 1992.

[129] B. Sartorius, M. Schlak, D. Stanze, H. Roehle, H. Künzel, D. Schmidt, H.-G. Bach, R. Kunkel and M. Schell, "Continuous wave terahertz systems exploiting 1.5 μm telecom technologies," *Opt. Expr.,* vol. 17, no. 17, pp. 15001 - 15007, 2009.

[130] H. Roehle, R. Dietz, B. Sartorius and M. Schell, "Fiber-Coupled Terahertz TDS Combining High Speed Operation with Superior Dynamic Range," in *37th International Conference on Infrared, Millimeter, and Terahertz Waves (IRMMW-THz)*, Wollongong, NSW, Australia, 2012.

[131] R. J. B. Dietz, Photoconductive THz Emitters and Detectors on the Basis of InGaAs/InP for Terahertz Time Domain Spectroscopy, Marburg/Lahn: Philipps-Universität Marburg, 2015.

[132] B. Sermage, D. Chemla, D. Sivco and A. Y. Cho, "Comparison of Auger Recombination in GaInAs-AlInAs Multiple Quantum Well Structure and in Bulk GaInAs," *IEEE J. of Quantum Electron.,* vol. 22, no. 6, p. 774 – 780, 1986.

[133] B. Globisch, R. J. B. Dietz, D. Stanze, T. Göbel and M. Schell, "Carrier Dynamics in Beryllium Doped Low-temperature-grown InGaAs/InAlAs," *Appl. Phys. Lett.,* vol. 104, no. 17, p. 172103 (4 pp), April 2014.

[134] R. J. B. Dietz, M. Gerhard, D. Stanze, M. Koch, B. Sartorius and M. Schell, "THz Generation at 1.55 µm Excitation: Six-fold Increase in THz Conversion Efficiency by Separated Photoconductive and Trapping Regions," *Opt. Expr.,* vol. 19, no. 27, pp. 25911 - 25917, 19 December 2011.

[135] H. Roehle, R. J. B. Dietz, H. J. Hensel, J. Böttcher, H. Künzel, D. Stanze, M. Schell and B. Sartorius, "Next Generation 1.5 µm Terahertz Antennas: Mesa-structuring of InGaAs/InAlAs Photoconductive

Layers," *Opt. Expr.,* vol. 18, no. 3, pp. 2296 - 2301, 1 February 2010.

[136] C. Ryu and S. G. Kong, "Boosting Terahertz Radiation in THz-TDS Using Continuous-wave Laser," *Electr. Lett.,* vol. 46, no. 5, pp. 359 - 360, 4 March 2010.

[137] R. Yano, H. Gotoh and Y. Hirayama, "Systematic Pump-probe Terahertz Wave Emission Spectroscopyof a Photoconductive Antenna Fabricated on Low-temperature Grown GaAs," *J. of Appl. Phys.,* vol. 96, no. 7, pp. 3635 - 3638, 1 October 2004.

[138] R. J. B. Dietz, B. Globisch, H. Roehle, D. Stanze, T. Göbel and M. Schell, "Influence and Adjustment of Carrier Lifetimes in InGaAs/InAlAs Photoconductive Pulsed TerahertzDetectors: & THz bandwidth and 90 dB Dynamic Range," *Opt. Expr.,* vol. 22, no. 16, pp. 19411 - 19422, 4 August 2014.

[139] P. U. Jepsen, R. H. Jacobsen and S. R. Keiding, "Generation and Detection of Terahertz Pulses from Biased Semiconductor Antennas," *J. Opt. Soc. Am. B,* vol. 13, no. 11, pp. 2424 - 2436, November 1996.

[140] J. E. Pedersen, V. G. Lyssenko, J. M. Hvam, P. Uhd Jepsen, S. R. Keiding, C. B. Sorensen and P. E. Lindelof, "Ultrafast Local Field Dynamics in Photoconductive THz Antennas," *Appl. Phys. Lett.,* vol. 62, no. 11, pp. 1265 - 1267, 15 March 1993.

[141] G. Rodríguez and A. J. Taylor, "Screening of the Bias Field in Terahertz Generation from Photoconductors," *Opt. Lett.,* vol. 21, no. 14, pp. 1046 - 1048, 15 July 1996.

[142] A. J. Taylor, P. K. Benicewicz and S. M. Young, "Modeling of Femtosecond Electromagnetic Pulses from Large-aperture Photoconductors," *Opt. Lett.,* vol. 18, no. 16, pp. 1340 - 1342, 15 August 1993.

[143] P. K. Benicewicz and A. J. Taylor, "Scaling of Terahertz Radiation from Large-aperture Biased InP Photoconductors," *Opt. Lett.,* vol. 18, no. 16, pp. 1332 - 1334, 15 August 1993.

[144] G. Rodríguez, S. R. Cáceres and A. J. Taylor, "Modeling of Terahertz Radiation from Biased Photoconductors: Transient Velocity Effects," *Opt. Lett.,* vol. 19, no. 23, pp. 1994 - 1996, 1 December 1994.

[145] J.-H. Son, T. B. Norris and J. F. Whitaker, "Terahertz Electromagnetic Pulses as Probes for Transient Velocity Overshoot in GaAs and Si," *J. Opt. Soc. Am. B,* vol. 11, no. 12, pp. 2519 - 2527, December 1994.

[146] C. Ludwig and J. Kuhl, "Studies of the Temporal and Spectral Shape of Terahertz Pulses Generated from Photoconducting Switches," *Appl. Phys. Lett.,* vol. 69, no. 9, pp. 1194 - 1196, 26 August 1996.

[147] G. Molis, A. Krotkus and V. Vaicaitis, "Intervalley Separation in the Conduction Band of InGaAs Measured by Terahertz Excitation Spectroscopy," *Appl. Phys. Lett.,* vol. 94, no. 9, p. 091104, 3 March 2009.

[148] E. Castro-Camus, J. Lloyd-Hughes and M. B. Johnston, "Three-dimensional Carrier-dynamics Simulation of Terahertz Emission from

Photoconductive Switches," *Phys. Rev. B,* vol. 71, no. 19, p. 195301 (7 pp), 19 May 2005.

[149] E. Castro-Camus, M. B. Johnston and J. Lloyd-Hughes, "Simulation of Fluence-dependent Photocurrent in Terahertz Photoconductive Receivers," *Semicond. Sci. Technol.,* vol. 27, p. 115011 (6 pp), 26 September 2012.

[150] M. Mittendorff, M. Xu, R. J. B. Dietz, H. Künzel, B. Sartorius, H. Schneider, M. Helm and S. Winnerl, "Large Area Photoconductive Terahertz Emitter for 1.55 μm Excitation Based on an InGaAs heterostructure," *Nanotechnol.,* vol. 24, no. 21, p. 214007 (7pp), 31 May 2013.

[151] T. F. Carruthers and J. F. Weller, "Picosecond Optical Mixing in Fast Photodetectors," *Appl. Phys. Lett.,* vol. 48, no. 7, pp. 460 - 462, 1986.

[152] J. Kyoung, M. Seo, H. Park, S. Koo, H.-S. Kim, Y. Park, B.-J. Kim, K. Ahn, N. Park, H.-T. Kim and D.-S. Kim, "Giant Nonlinear Response of Terahertz Nanoresonators on VO2 Thin Film," *Opt. Expr.,* vol. 18, no. 16, pp. 16452 - 16459, 2010.

[153] F. Fan, W.-H. Gu, S. Chen, X.-H. Wang and S.-H. Chang, "State Conversion Based on Terahertz Plasmonics with Vanadium Dioxide Coating Controlled by Optical Pumping," *Opt. Lett.,* vol. 38, no. 9, pp. 1582 - 1584, 2013.

[154] J. L. M. v. Mechelen and D. J. H. C. M. A. C. R. (. H. Merbold, "Towards the Industrialization of THz Technology: The Case of Quality Control of Paper

During Production," in *SPIE Photonics West OPTO*, San Francisco, 2017.

[155] J. A. Zeitler and Y.-C. Shen, "Industrial Applications of Terahertz Imaging," in *Terahertz Spectroscopy and Imaging*, 1 ed., vol. 171, Springer-Verlag Berlin Heidelberg, 2013.

[156] N. Cohen, J. W. Handley, R. D. Boyle, S. L. Braunstein and E. Berry, "Experimental Signature of Registration Noise in Pulsed Terahertz Systems," *Fluct. Noise Lett.,* vol. 6, no. 1, March 2006.

[157] A. Wojdyla and G. Gallot, "Phase Noise Investigation in Terahertz Time-domain Spectroscopy Measurements," in *38th International Conference on Infrared, Millimeter, and Terahertz Waves (IRMMW-THz)*, Mainz, 2013.

[158] D. Jahn, S. Lippert, M. Bisi, L. Oberto, J. C. Balzer and M. Koch, "On the Influence of Delay Line Uncertainty in THz Time-domain Spectroscopy," *J. of Infrared, Millimeter and Terahertz Waves,* vol. 37, no. 6, pp. 605 - 613, 19 January 2016.

[159] D. A. Humphreys, M. Naftaly and J. F. Molloy, "Effect of Time-delay Errors on THz Spectroscopy Dynamic Range," in *39th International Conference on Infrared, Millimeter, and Terahertz waves (IRMMW-THz)*, Tucson, 2014.

[160] W. Withayachumnankul, H. Lin, S. P. Mickan, B. M. Fischer and D. Abbott, "Analysis of Measurement Uncertainty in THz-TDS," in *Proc. of SPIE, Photonic Materials, Devices, and Applications II*, 2007.

[161] W. Withayachumnankul, B. M. Fischer, H. Lin and D. Abbott, "Uncertainty in Terahertz Time-domain Spectroscopy Measurement," *J. Opt. Soc. Am. B,* vol. 25, no. 6, pp. 1059 - 1072, 2008.

[162] X. Xu, X. Wang and L. Wang, "Deviation of Optical Constants Extracted in Terahertz Transmission Spectroscopy," *Appl. Opt.,* vol. 45, no. 4, pp. 648 - 652, 1 February 2006.

[163] M. V. Exter and D. R. Grischkowsky, "Characterizationof an Optoelectronic Terahertz Beam System," *IEEE Transact. on Microwave Theory and Techniques,* vol. 38, no. 11, pp. 1684 - 1691, November 1990.

[164] S. Mickan, J. Xu, J. Munch, X.-C. Zhang and D. Abbott, "The limit of spectral resolution in THz time-domain spectroscopy," in *Proc. SPIE*, 2004.

[165] W. Kester, "http://qtwork.tudelft.nl," 10 March 2005. [Online]. Available: http://qtwork.tudelft.nl/~schouten/linkload/adc-tutorial.pdf. [Accessed June 9 2017].

[166] L. Wu, "Optimierung des Signal-Rausch-Abstands von AD-Wandlern," *Elektron. Ind.,* vol. 11, pp. 50 - 52, 2010.

[167] T. Strohmer, "Numerical analysisof the nonuniform sampling problem," *J. of Comp. and Appl. Math.,* vol. 122, pp. 297 - 316, 2000.

[168] S. Maymon and A. V. Oppenheim, "Sinc Interpolation of Nonuniform Samples," *IEEE Transact.*

on Signal Processing, vol. 59, no. 10, pp. 4745 - 4758, 2011.

[169] D. A. Humphreys and M. Naftaly, "Dynamic Range Improvement of THz Spectroscopy," in *Conference on Precision Electromagnetic Measurements (CPEM 2014)*, Rio de Janeiro, 2014.

[170] K. J. Coakley and P. Hale, "Alignment of Noisy Signals," *IEEE Transact. on Instr. and Meas.,* vol. 50, no. 1, pp. 141 -149, 2001.

[171] K. C. McGill and L. J. Dorfman, "High-Resolution Alignment of Sampled Waveforms," *IEEE Transact. on Biomed. Engineering,* vol. 31, no. 6, pp. 462 - 468, 1984.

[172] G. Vandersteen and J. S. Y. Rolain, "An Identification Technique for Data Acquisition Characterization in the Presence of Nonlinear Distortions and Time Base Distortions," *IEEE Transact. on Instr. and Meas.,* vol. 50, no. 5, pp. 1355 - 1363, 2001.

[173] P. D. Hale, A. Dienstfrey, J. C. M. Wang, D. F. Williams, A. Lewandowski, D. A. Keenan and T. S. Clement, "Traceable Waveform Calibration With a Covariance-Based Uncertainty Analysis," *IEEE Transact. on Instr. and Meas.,* vol. 58, no. 10, pp. 3554 - 3568, 2009.

[174] R. Jané, H. Rix, P. Caminal and P. Laguna, "Alignment Methods for Averaging of High-Resolution Cardiac Signals: A Comparative Study of Performance," *IEEE Transact. on Biomed. Engineering,* vol. 38, no. 6, pp. 571 - 579, 1991.

[175] M. Tonouchi, "Cutting-edge Terahertz Technology," *Nature Photonics,* vol. 1, February 2007.

[176] F. Eichhorn, R. K. Olsson, J. C. D. Buron, L. Grüner-Nielsen, J. E. Pedersen and P. U. Jepsen, "Optical Fiber Link for Transmission of 1-nJ Femtosecond Laser Pulses at 1550 nm," *Opt. Expr.,* vol. 18, no. 7, pp. 6978 - 6987, 2010.

[177] S.-P. Han, H. Ko, N. Kim, H.-C. Ryu, C. W. Lee, Y. A. Leem, D. Lee, M. Y. Jeon, S. K. Noh, H. S. Chun and K. H. Park, "Optical Fiber-coupled InGaAs-based Terahertz Time-domain Spectroscopy System," *Opt. Lett.,* vol. 36, no. 16, pp. 3094 - 3096, 2011.

[178] J. Palací and B. Vidal, "Distributed THz Transmitter/Receiver based on a 1.5 μm Fiber Link," in *36th International Conference on Infrared, Millimeter and Terahertz Waves - IRMMW-THz*, Houston, 2011.

[179] J. Palací, A. Bockelt and B. Vidal, "Amplified Optical Fiber Link for Remote Generation of THz Radiation," in *Proc. IEEE Int. Topical Meeting on Microw. Photon.* , Alexandria, Virginia, USA, 2013.

[180] M. J. Hamp, J. Wright, M. Hubbard and B. Brimacombe, "Investigation into the Temperature Dependence of Chromatic Dispersion in Optical Fiber," *IEEE Photon. Technol. Lett.,* vol. 14, no. 11, pp. 1524 - 1526, 2002.

[181] J. Palací and B. Vidal, "Terahertz Radiation Shaping Based on Third-order Dispersion and Self-phase Modulation in Standard Single-mode Optical

Fiber," *International J. of Infrared Millimeter and Terahertz Waves,* vol. 33, no. 6, pp. 605 - 614, 21 April 2012.

[182] P. Krehlik, L. Sliwczyynski, L. Buczek and M. Lipinsky, "Fiber-optic Joint Time and Frequency Transfer with Active Stabilization of the Ptopagation Delay," *IEEE Trans. Instrum. Meas.,* vol. 61, no. 10, pp. 2844 - 2851, 2012.

[183] H. Hoshina, Y. Sasaki, a. Hayashi and C. Otani, "Noninvasive Mail Inspection System with Terahertz Radiation," *Appl. Spectroscopy,* vol. 63, no. 1, pp. 81 - 86, 2009.

[184] J. Kim, J. A. Cox, J. Chen and F. X. Kärtner, "Drift-free Femtosecond Timing Synchronization of Remote Optical and Microwave Sources," *Nature Photon.,* vol. 2, pp. 733 - 736, 2008.

[185] M. Y. Peng, P. T. Callahan, A. H. Nejadmalayeri, S. Valente, M. Xing, L. Grüner-Nielsen, E. M. Monberg, M. Yan, J. M. Fini and F. X. Kärtner, "Long-term Stable Sub-femtosecond Timing Distribution via a 1.2 km Polarization Maintaining Fiber Link: Approaching 10^(-21) Link Stability," *Opt. Expr.,* vol. 21, no. 17, pp. 19982 - 19989, 2013.

[186] G. P. Agrawal, Nonlinear Fiber Optics, Amsterdam: Elsevier Inc., 2012.

[187] A. Bockelt, J. Palací and B. Vidal, "Control of Terahertz Emission in Photoconductive Antennas through an Additional Optical Continuous Wave," *Opt. Lett.,* vol. 38, no. 16, pp. 3123 - 3125, 15 August 2013.

List of Journal Articles derived from this Thesis

A. A. Bockelt, J. Palací and B. Vidal, "Control of Terahertz Emission in Photoconductive Antennas through an Additional Optical Continuous Wave," *Optics Letters*, vol. 38, no. 16, pp. 3123 - 3125, 15 August 2013.

B. A. Bockelt, J. Palací and B. Vidal, "All-fiber Centralized Architecture for Parallel Terahertz Sensors," *IEEE Transactions on Terahertz Science and Technology*, vol. 5, no. 1, pp. 137-144, January 2015.

C. A. Bockelt and B. Vidal, "Dynamic Tuning of Mean Carrier Momentum Relaxation Time in InGaAs–InAlAs THz Photoconductive Switches," *IEEE Transactions on Terahertz Science and Technology*, vol. 7, no. 1, pp. 107 - 113, 2017.

Other Contributions of the Author

Journal Papers:

D. R. R. Thomson, A. S. Bockelt, E. Ramsay, S. Beecher, A. H. Greenaway, A. K. Kar, D. T. Reid, "Shaping ultrafast laser inscribed optical waveguides using a deformable mirror", *Optics Express*, vol. 16, no. 17, August 2008.

E. J. Palací, A. Bockelt, B. Vidal, "SOA-based optical processing for terahertz time-domain spectroscopy", *Electronics Letters*, vol. 48, no. 10, pp. 593 – 594, May 2012.

F. J. Palací, A. Bockelt, B. Vidal, "Terahertz radiation shaping based on optical spectrum modulation in the time domain", *Optics Express*, vol. 20, no. 21, pp. 23117 – 23125, October 2012.

G. B. Vidal, A. Bockelt, J. Palací, "Cascaded Four-Wave Mixing for Microwave Photonic Harmonic Multiplication", *IEEE Photonics Technology Letters*, vol. 25, no. 1, pp. 100-104, January 2013.

H. F. Sanjuan, A. Bockelt, B. Vidal, "Birefringence measurement in the THz range based on double Fourier analysis", *Optics Letters*, vol. 39, no. 4, pp. 809-8012, February 2014.

I. F. Sanjuan, A. Bockelt, B. Vidal, "Determination of refractive index and thickness of a multilayer structure with a single

THz time domain spectroscopy measurement", *Applied Optics*, vol. 53, no. 22, pp. 4910-4913, August 2014.

Conference Papers:

J. J. Palací, A. Bockelt, B. Vidal, "Ultra-short Pulse Shaping based on Time-domain Spectrum Modulation in a Semiconductor Optical Amplifier", IEEE International Topical Meeting on Microwave Photonics (MWP2012), Noordwijk (The Netherlands), 11-14 September 2012.

K. J. Palací, A. Bockelt and B. Vidal, "Amplified Optical Fiber Link for Remote Generation of THz Radiation", IEEE International Topical Meeting on Microwave Photonics (MWP2013), Alexandria (USA), 28-31 October 2013.

List of Figures

List of Tables

List of Acronyms

AOPDF	**A**cousto-**O**ptic **P**rogrammable **D**ispersive **F**ilter
ASE	**A**mplified **S**pontaneous **E**mission
ASOPS	**A**synchronous **O**ptical **S**ampling
BWO	**B**ackward **W**ave **O**scillator
CB	**C**onduction **B**and
CD	**C**hromatic **D**ispersion
CPA	**C**hirped **P**ulse **A**mplification
CW	**C**ontinuous **W**ave
DBM	**D**ouble **B**alanced **M**ixer
DC	**D**irect **C**urrent
DCF	**D**ispersion **C**ompensating **F**iber
DFG	**D**ifference **F**requency **G**eneration
DGD	**D**ifferential **G**roup **D**elay
DR	**D**ynamic **R**ange
DSF	**D**ispersion **S**hifted **F**iber
DTDS	**D**ifferential **T**ime-**D**omain **S**pectroscopy
ECOPS	**E**lectronically **C**ontrolled **O**ptical **S**ampling
EDFA	**E**rbium-**D**oped **F**iber **A**mplifier
EOS	**E**lectro-**O**ptic **S**ampling
FEL	**F**ree-**E**lectron **L**aser
FIR	**F**ar **I**nfra**R**ed
FT	**F**ourier **T**ransform
FWHM	**F**ull **W**idth at **H**alf **M**aximum
HRFZ-Si	**H**igh **R**esistivity **F**loat **Z**one-**Si**licon
HEMT	**H**igh **E**lectron **M**obility **T**ransistor
LAE	**L**arge **A**rea **E**mitter
LO	**L**ongitudinal **O**ptical

LODL	**L**inear **O**ptical **D**elay **L**ine
MBE	**M**olecular **B**eam **E**pitaxy
MIR	**M**id **I**nfra**R**ed
MLHS	**M**ulti**L**ayer **H**etero-**S**tructure
MMIC	**M**onolithic **M**icrowave **I**ntegrated **C**ircuit
MODL	**M**otorized **O**ptical **D**elay **L**ine
MZM	**M**ach-**Z**ehnder-**M**odulator
NIR	**N**ear InfraRed
OA	**O**ptical **A**ttenuator
OC	**O**ptical **C**hopper
OR	**O**ptical **R**ectification
OSCAT	**O**ptical **S**ampling by **Ca**vity **T**uning
PC	**P**olarization **C**ontroller
PLL	**P**hase **L**ocked **L**oop
PMF	**P**olarization **M**aintaining **F**iber
PMD	**P**olarization **M**ode **D**ispersion
PMP	**P**oly-**M**ethyl-**P**entene
PON	**P**assive **O**ptical **N**etwork
PSD	**P**hase-**S**ensitive **D**etection
PS	**P**hotoconductive **S**witching
PTFE	**P**oly-**T**etra-**F**luoro-**E**thylene
QCL	**Q**uantum **C**ascade **L**aser
RF	**R**adio **F**requency
RMS	**R**oot **M**ean **S**quare
RODL	**R**otary **O**ptical **D**elay **L**ine
RoF	**R**adio **o**ver **F**iber
Rx	**R**eceiver
SD	**S**tandard **D**eviation
SRH	**S**hockley **R**ead **H**all
SMF	**S**ingle **M**ode **F**iber

SNR	**S**ignal-to-**N**oise **R**atio
SPM	**S**elf-**P**hase **M**odulation
SQNR	**S**ignal-to-**Q**uantization **N**oise-**R**atio
THz	**T**era**H**ert**z**
THz-TDS	**T**era**H**ert**z** **T**ime-**D**omain **S**pectroscopy
Ti:Sapphire	**Ti**tanium:**Sapphire**
TOD	**T**hird **O**rder **D**ispersion
Tx	**T**ransmitter (Emitter)
VB	**V**alence **B**and

Acknowledgement

Besides personal dedication, the elaboration of this thesis benefited from direct or indirect support of many others. At this point, I would like to express my appreciation and gratitude to those, who supported me in many different ways during the doctoral process.

Firstly, I would like to thank Javier Martí, Roberto Llorente and Borja Vidal for accepting and welcoming me as PhD student at the Nanophotonics Technology Center, the 'Systems and Networks Research Line' and the 'Terahertz/Microwave Photonics' workgroup. Special thanks go to Borja for his availability as thesis director and much more for his dedication, which has gone far beyond mere professional advisory, but also helped in administrative as well as private issues. Succeeding, I want to express my gratefulness to my forerunner Jesús Palací, who has always been a formidable guide and companion. Thanks for your guidance in the laboratory and advisory in theoretical aspects of the work. You have been a crucial supporter during my episode at the NTC. Furthermore, I want to thank all colleagues of the 'Terahertz/Microwave Photonics' workgroup comprising Margherita Colleoni, Diego Samaniego, Miguel Ángel Báez, Rafael Pérez, José Carlos Serrano and former guest-researcher Federico Sanjuan. Thanks to all of you for your technical assistance and fruitful discussions. Special thanks go to David Zurita as the engineer in charge of laboratory equipment, who has always been at my service, Jordi Peiró, David Lozano and Julio Morera, our IT-specialists, who have always given their very best to provide quick and helpful solutions.. Moreover, I do not

want to be forgotten all the colleagues of the NTC, for their advisory, encouragement and companionship.

From outside the UPV, I would like to thank Flávio Caldas da Cruz of the physics department of the Universidade Estadual de Campinas (UNICAMP) in Campinas, São Paulo, Brazil for the acceptation and supervision in his workgroup during my research stay. Also thanks to Luís Eduardo Evangelista de Araujo for being the person in charge during the absence of Professor da Cruz.

A tribute goes to the Spanish Ministry of Education, Culture and Sports for the concession of the FPU grant, which set my work at the NTC onto a financial basis.

A very special award goes to my girlfriend Maricela and her team at 'La Piazzetta delle Delizie' for her culinary and mental support, assuring my everyday well-being over the years. At last, I want to praise my family and friends for their encouraging words, visits and general back up.